E.O. Paton Electric Welding Institute of the National Academy of Science of Ukraine
International Association “Welding”

The Paton Welding Journal

04
2026

International Scientific-Technical and Production Journal ♦ Founded in January 2000 (12 Issues Per Year)

Address of Editorial Office:
E.O. Paton Electric Welding Institute, 11 Kazymyr Malevych Str., 03150, Kyiv, Ukraine
E-mail: office@paton.kiev.ua; https://paton.org.ua/en/

Address of Publisher:
International Association “Welding”, 11 Kazymyr Malevych Str., 03150, Kyiv, Ukraine
Tel.: (38044) 205 23 90, E-mail: patonpublishinghouse@gmail.com; journal@paton.kiev.ua
https://patonpublishinghouse.com/eng/journals/tpwj

The Journal was registered by the National Council of Ukraine on Television and Radio Broadcasting on 09.05.2024, carrier identifier R30-04569
ISSN 0957-798X (Print), ISSN 3041-2293 (Online)
DOI: https://doi.org/10.37434/tpwj, from #01, 2020 to now; DOI: https: //doi.org/10.15407/tpwj from #01, 2014 to #12, 2019.

Subscriptions, 12 issues per year:
348 Euro — annual subscription for the printed (hard copy) version, air postage and packaging included;
288 Euro — annual subscription for the electronic version (sending issues in pdf format or providing access to IP addresses).

Representative Offices of “The Paton Welding Journal”:

BRAZIL, Arc Dynamics
Address: Nova Iguacu, Rio de Janeiro, Brazil
Daniel Adolpho, Tel.: +55 21 9 6419 5703,
E-mail: dadolpho@arcdynamics.com.br

CHINA, China-Ukraine Institute of Welding, Guangdong Academy of Sciences
Address: Room 210, No. 363 Changxing Road, Tianhe, Guangzhou, 510650, China
Zhang Yupeng, Tel.: +86-20-61086791,
E-mail: patonjournal@gwi.gd.cn

BULGARIA, Bulgarian Welding Society
Address: Blvd. Asen Yordanov No.10, Sofia 1592, Bulgaria
Pavel Popgeorgiev, Tel.: +359 899 96 22 20,
E-mail: office@bws-bg.org

POLAND, PATON EUROPE Sp. z o. o.
Address: ul. Kapitałowa 4, 35-213, Rzeszów, Poland
Anton Stepakhno, Tel.: +38067 509 95 67,
E-mail: Anton.Stepakhno@paton.ua

The content of the Journal includes articles received from authors from around the world in the field of welding, cutting, cladding, soldering, brazing, coating, 3D additive technologies, electrometallurgy, material science, NDT and selectively includes translations into English of articles from the following journals, published in Ukrainian:

- «Avtomatychne Zvaryuvannya» (Automatic Welding), https://patonpublishinghouse.com/eng/journals/as;
- «Suchasna Elektrometalurhiya» (Electrometallurgy Today), https://patonpublishinghouse.com/eng/journals/sem;
- «Tekhnichna Diahnostyka ta Neruinivnyi Kontrol» (Technical Diagnostics & Nondestructive Testing), https://patonpublishinghouse.com/eng/journals/tdnk.

CONTENTS

ORIGINAL ARTICLES

*Translated Article(s) from “Avtomatychne Zvaryuvannya” (Automatic Welding), No. 6, 2025.

**Translated Article(s) from “Avtomatychne Zvaryuvannya” (Automatic Welding), No. 2, 2026.

***Translated Article(s) from “Suchasna Elektrometalurhiya” (Electrometallurgy Today), No. 1, 2026.

Indexing: The electronic edition of “The Paton Welding Journal” is stored in the V.I. Vernadsky National Library of Ukraine (eVerLib), included in the OPEN UKRAINIAN CITATION INDEX database and international databases: CROSSREF, EBSCO, Google Scholar, INDEX COPERNICUS, Scilit, ULRICHSWEB, BASE, Jisk, German Union Catalogue of Serials (ZDB), SCISPACE, TIB — Leibniz Information Centre for Science and Technology and University Library.

The purpose of “The Paton Welding Journal” is to emerging new scientific knowledge, to present a forum for discussing of new result in welding and related technologies which contribute to the creation of new technologies and engineering samples with improved technical and economic performance and to facilitate their implementation. That is why in articles published in the journal, the emphasis is on both scientific novelty and practical value. Extensive cooperation of the Journal with research institutes, educational centers and industrial makes it possible to review articles by leading experts and to involve in the publication of advanced research results.

DOI: https://doi.org/10.37434/tpwj2026.04.01

EFFECT OF PROCESS PARAMETERS OF THE ADDITIVE ELECTRON BEAM PROCESS ON THE PROPERTIES OF THIN-WALLED PRODUCTS FROM VT6 ALLOY

V.A. Matviichuk, V.M. Nesterenkov, M.O. Sysoev

E.O. Paton Electric Welding Institute of the NASU
11 Kazymyr Malevych Str., 03150, Kyiv, Ukraine

ABSTRACT

The subject of investigation is the process of structure formation and mechanical properties of thin-walled products fabricated by additive electron beam melting (EBM) technology from VT6 titanium alloy (Ti–6Al–4V) powder. The alloy is widely used in industry due to its high weldability, strength, and fatigue resistance. Spherical VT6 titanium alloy powder with a particle size of 40–160 μm, produced by rotary plasma atomisation, was used as feedstock. A computer model was created in Materialise Magics software, from which 36 specimens were printed at beam travel speeds ranging from 500 to 6000 mm/s. It was established that a beam travel speed of 500 mm/s combined with an energy density of 40 J/mm³ ensures complete melting of the powder layer, stable shape formation, and controlled thermal conditions. This promotes the formation of a balanced (α+β)-microstructure with acicular α-phase morphology and α-lamella thickness of 0.5–1.5 μm. The volume fraction of α-Ti is 90±3 %, β-Ti — 10±3 %. The microhardness level of the specimens is $HV_{0.1}$ = 3.5±0.7 GPa. The results demonstrate that the combination of high-quality powder feedstock and a rational printing mode ensures high process reproducibility, structural stability, and suitability of the technology for manufacturing thin-walled products.

KEYWORDS: additive technology, electron beam, VT6 titanium alloy, Ti–6Al–4V, thin-walled products, process parameters, microstructure, chemical composition, microhardness

INTRODUCTION

Traditional metal processing methods are often limited in their capability to produce components with complex configurations. This drives the active development of additive technologies, which enable the fabrication of complex-shaped parts with predicted properties [1].

Research on additive manufacturing processes is relevant to modern materials science, production technologies, and mechanical engineering. Its scientific significance is determined by a set of fundamental and applied challenges that remain insufficiently resolved to date. Industry continuously requires new solutions for the fabrication of lightweight, strong, and heat-resistant structures. This is especially true for components made from titanium alloys that operate under high temperatures, variable loads, and aggressive environments [2]. The VT6 titanium alloy of the Ti–6Al–4V alloying system is one of the most widely used in industry due to its combination of high strength, thermal, and corrosion resistance [3]. These properties provide for its broad application in the aerospace, energy, and medical sectors.

In the field of additive manufacturing, intensive development is observed in wire-based technologies — Wire Arc Additive Manufacturing (WAAM), Wire-based Directed Energy Deposition (wire-DED), Laser Metal Deposition (LMD) — as well as powder-based methods such as Selective Laser Melting (SLM) and Electron Beam Melting (EBM) [4]. In [5], thin-walled specimens of Ti–6Al–4V alloy produced by wire-DED were investigated. This method is characterised by limited resolution, which complicates its application for producing thin-walled products with complex geometries. As noted in [6], wire-DED technology has lower shape formation accuracy compared to powder-based methods such as SLM and EBM. These technologies use a laser or electron beam as the energy source, which ensures stable powder melting and precise component geometry. In [7], the mechanical, microstructural, and electrochemical properties of Ti–6Al–4V specimens fabricated by EBM and SLM are compared. It is shown that EBM provides higher strength, uniform elongation, a more favourable microstructure, stable temperature conditions, and operation in a high vacuum environment, which is especially important for chemically reactive titanium alloys [3]. However, the comparative nature of that study did not allow printing parameters to be determined for specific product types. A number of technical issues remain open for further investigation.

In [8], the effect of EBM parameters on the properties of Ti–6Al–4V products was examined. The authors identified process modes ensuring optimal morphology and stable material structure. In [9], the

influence of EBM parameters on the microstructure and microhardness of titanium alloys was studied. It was shown that Ti–6Al–4V forms a dense cast structure with lamellar-acicular α′-phase and a uniform microhardness distribution. However, that study did not cover thin-walled components, which are more sensitive to thermal gradients and local defects.

Previous research demonstrates the advantages of EBM over other methods (SLM, wire-DED), yet leaves open the question of process parameter optimisation for thin-walled products, which are more susceptible to thermal gradients and local defects. Therefore, identifying the patterns governing the influence of EBM parameters on the structure and properties of thin-walled components from VT6 titanium alloy is highly relevant.

Thus, research in this direction has both scientific value — elucidating the mechanisms of structure formation and phase transformations — and practical value — ensuring the production of components with homogeneous structure, stable properties, and high reproducibility under industrial conditions.

THE AIM OF THE STUDY

is to investigate the patterns of thin-walled specimen formation produced by EBM from VT6 titanium alloy powder.

To achieve this aim, the following tasks were set:

- to investigate the surface morphology of thin-walled specimens;
- to determine their macro- and microstructure;
- to investigate chemical and phase composition;
- to measure microhardness;
- to identify printing modes that provide the best structural condition.

THE OBJECT OF INVESTIGATION

is the process of structure formation and mechanical properties of thin-walled products fabricated by EBM from VT6 titanium alloy powder.

MATERIALS AND EQUIPMENT

VT6 titanium alloy powder produced by rotary plasma atomisation of a rod blank on equipment by Multiflex LLC (Ukraine) [10] was used in the study. The powder granules have a spherical shape with diameters of 40–160 μm, ensuring high bulk density, flowability, and uniform melting during printing. The chemical composition of the powder is given in Table 1.

Test specimens were fabricated by EBM using experimental equipment developed at the PWI. A detailed description of the equipment, process parameters, and control algorithms is given in [11, 12].

Printing was carried out in a vacuum chamber at a working pressure of 10^{-2} Pa. The accelerating voltage of the electron beam gun was 60 kV. The sequence of operations, stages of specimen fabrication, and printing process parameters were determined on the basis of prior research [12]. Five electron beam scanning speed modes in the range of 500–6000 mm/s were employed. The choice of this range is both technologically and economically justified, as it provides an optimal combination of product quality and process efficiency. The powder layer thickness was 100 μm; a bidirectional scanning strategy with a trajectory offset step of 0.2 mm was selected, with the scanning direction of each subsequent layer rotated by 90°. The effective

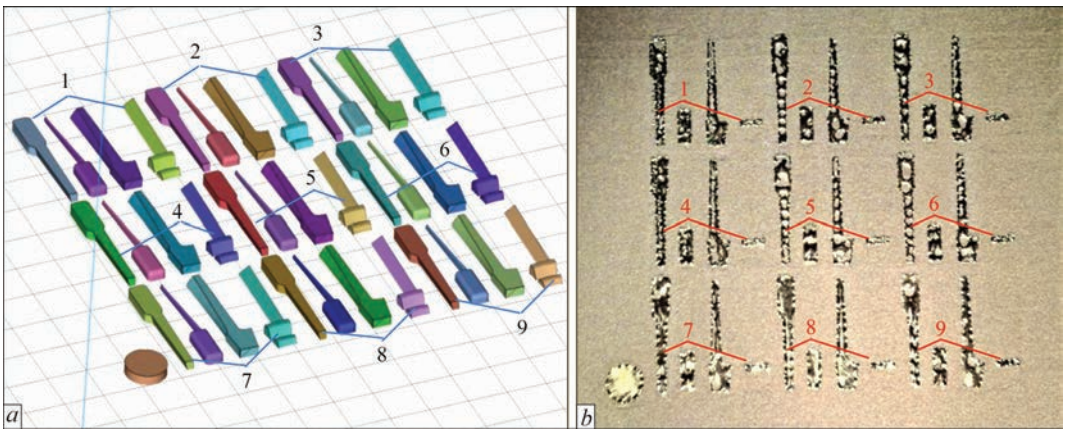

Figure 1. Models and products: *a* — assembly model; *b* — test products, 1–9 — specimen groups

Table 1. Chemical composition of VT6 powder in accordance with TU U 24.4-31914753-001:2018 [10]

Alloying elements, wt.% of particles				Impurities, wt.% of particles			
Al	V	Fe	Ti	O	C	N	H
5.5–6.75	3.5–4.5	≤ 0.3	Base	≤ 0.2	≤ 0.08	≤ 0.05	≤ 0.015

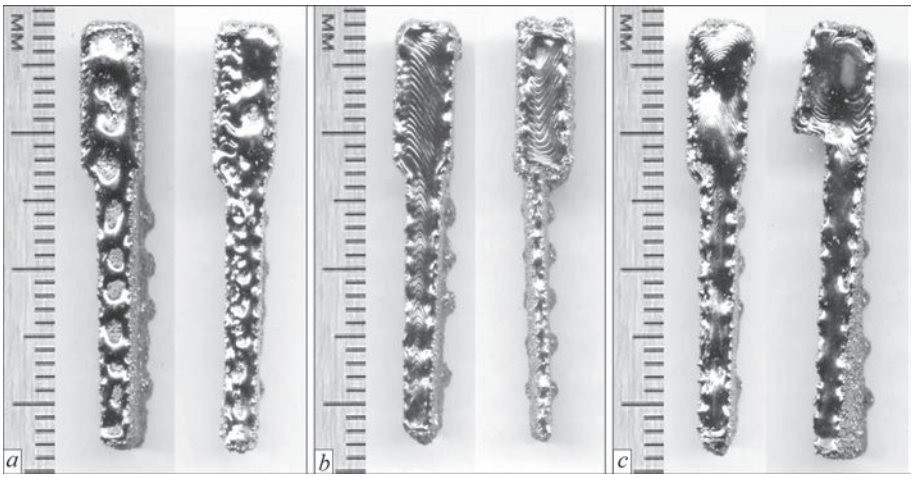

Figure 2. Surface morphology of specimens: *a* — porous; *b* — dense; *c* — bumpy

beam diameter was determined by the dynamic focusing current. Two outer contours were used to improve geometric accuracy [13]. During printing, the powder layer temperature was maintained at 680 °C [12].

A three-dimensional model of the products, incorporating fragments of rotor group components of a gas turbine engine, was created in Materialise Magics. Nine groups of specimens were realised, each corresponding to a separate printing mode (Figure 1, *a*).

A total of 36 specimens (Figure 1, *b*) were printed with the following geometric parameters: length — 30 mm, working section width — up to 2.5 mm, trailing edge thickness — 5 mm, height — 10 mm, of which 5 mm constitute the technological supports. Each of the 9 groups contained 4 specimens produced with varying beam speed, energy density, and focusing.

RESEARCH METHODS

Microstructure investigations were performed using conventional methods. Cross-sectional cuts were made on an electro-discharge machine. Specimens were ground on abrasive paper and polished with diamond suspension. Surfaces were etched in an aqueous solution of 6 % HNO_3 and 2 % HF. Structures were examined using a Carl Zeiss Jena optical microscope. Digital processing of micrographs and quantitative assessment of micro-defects were performed in ImageJ software. Surface topography and phase composition analysis were carried out using TESCAN VEGA 3 SBH EP scanning electron microscope at an accelerating voltage of 20 kV. Chemical composition and element distribution in the metal structure were determined by XRF using Bruker Quantax 610M spectrometer in the atomic number range from magnesium (Z = 12) to uranium (Z = 92). Phase analysis was carried out by X-ray diffraction (XRD) using Inel EQUINOX-1000 diffractometer in grazing incidence geometry at an angle of incidence of 5° to the surface. The X-ray source was a copper anode . Diffraction patterns were recorded in the range 2θ = 30–80° using a radial position-sensitive detector. Experimental data were processed in Match! software. Phase volume fractions were determined by the Rietveld method. Microhardness was measured by the Vickers method using PMT-3 instrument. Tests were conducted at a load of 0.1 kgf (0.98 N) with a dwell time of 10 s. Measurements were performed with a step of 250 μm within the cross-section, with one indentation at each control point.

Table 2. Process printing parameters and surface morphology type of specimens

Group (Figure 1)	Beam parameters				Surface morphology type
	Speed, mm/s	Power, W	Energy density, J/mm³	Dynamic focus current, A	
1	6000	2160	18	0	Porous
2	2000	1000	25	0.83	
3	2000	1000	25	0	
4	4000	1760	22	0	
5	4000	1760	22	0.83	
6	4000	1760	22	0.55	
7	1000	900	45	0	Bumpy
8	500	400	40	0	Dense
9	1000	900	45	1.11	Bumpy

RESULTS AND DISCUSSION

INVESTIGATION OF SPECIMEN SURFACE MORPHOLOGY

The surface condition of the specimens (Figure 1, *b*) was evaluated visually. Initial inspection allowed the specimens to be classified into three types according to surface morphology: porous (Figure 2, *a*), dense (Figure 2, *b*), and bumpy (Figure 2, *c*). The process printing parameters and the corresponding surface morphology type are given in Table 2.

Analysis of the data (Figure 1, *b*; Table 2) showed that the best (defect-free) surface condition corresponds to dense morphology, observed in Group No. 8 specimens printed at a beam speed of 500 mm/s. Bumpy morphology is characteristic of specimens from Groups Nos 7 and 9, produced at a beam speed of 1000 mm/s. Porous morphology with a large number of defects is characteristic of specimens from Groups Nos 1–6, produced at beam speeds in the range of 2000–6000 mm/s.

Based on the data from Figure 1, *b* and Table 2, it was established that surface morphology is significantly dependent on beam travel speed and beam power, whereas the effect of focusing parameters proved to be less significant. The results are explained by the characteristics of thermal processes in the melting zone. At high travel speeds (2000–6000 mm/s), beam power was excessive, leading to excessive heat input and porous surface formation. Bumpy morphology, characteristic of 1000 mm/sspeed may be associated with localised overheating causing surface irregularities. Reducing the speed to 500 mm/s, however, ensures an optimal balance between beam power and speed.

One specimen from each of Groups Nos 1, 3, 4, 7, and 8 (Table 2) was selected for further investigation, covering the full range of speed modes studied.

INVESTIGATION OF SPECIMEN STRUCTURE

In addition to surface condition, the microstructural state is an important material characteristic. Analysis of the microsections (Figure 3) revealed defects in the form of micropores. Defect assessment was carried out by digital processing of micrographs, allowing their number, dimensions, and area to be determined. Measurement results are given in Table 3.

Analysis of Table 3 data established that Specimens Nos 1, 3, and 4 have a significant number of defects — 10 or more — and porous surface morphology (Table 2). The mean defect area was 9124–18294 μm^2 with a mean size of 110–156 μm (Table 3). Specimen No. 7 had a bumpy surface type (Table 2). The mean defect area did not exceed 7775 μm^2 with a mean size of 102 μm. The number of identified pores was only three (Table 3). Specimen No. 8 was characterised by a dense surface (Table 2) with a minimum number of

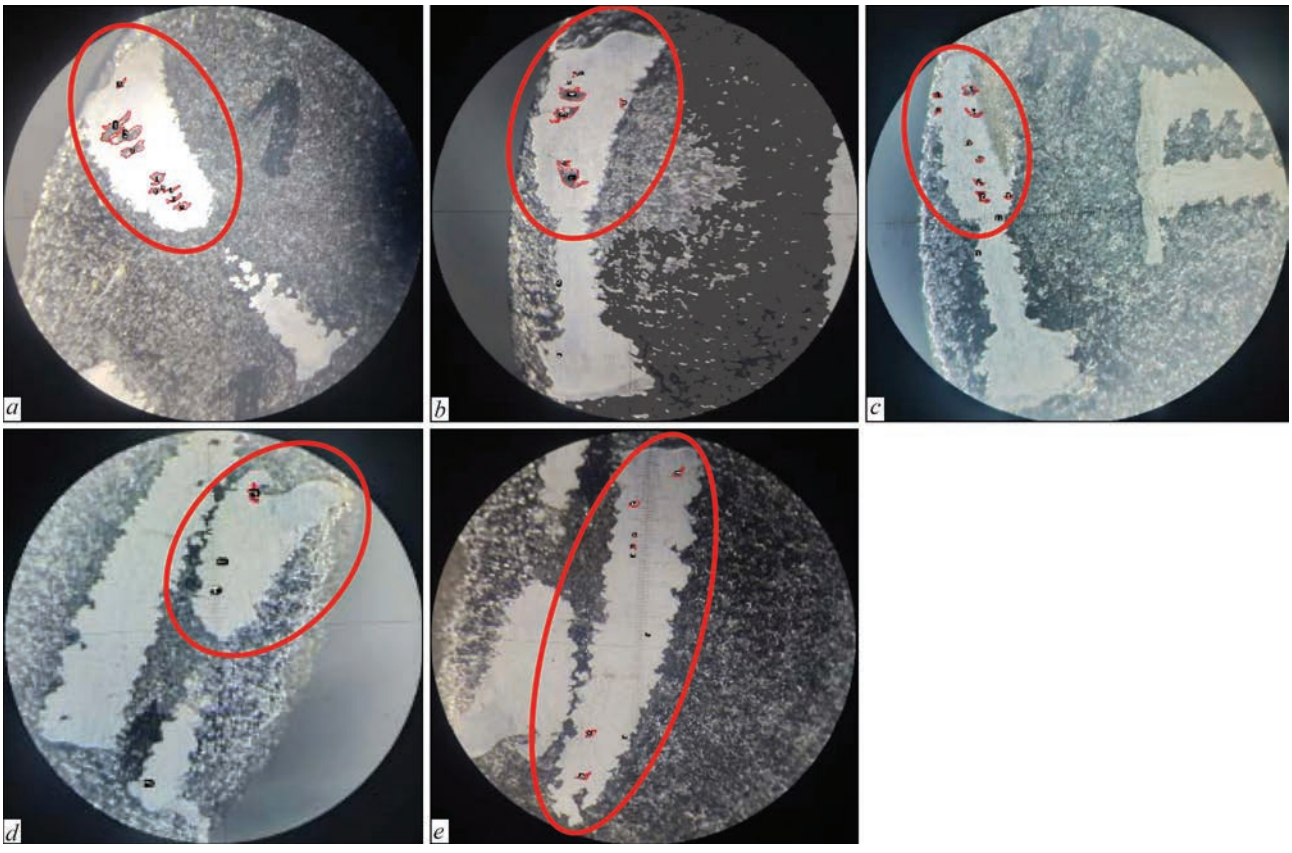

Figure 3. Structures of specimens, No.: *a* — 1; *b* — 3; *c* — 4; *d* — 7; *e* — 8. The area investigated is marked in red

Table 3. Results of internal defect investigations in test specimens

Specimen No. (Figure 3)	Defect area (S) and size (D)						Number of identified defects
	S_{max}, μm²	D_{max}, μm	S_{min}, μm²	D_{min}, μm	S_{av}, μm²	D_{av}, μm	
1	40477	232	3618	69	18294	156	10
3	40454	232	3182	65	14841	141	10
4	17699	154	3022	63	9124	110	11
7	20733	166	2647	59	7775	102	3
8	13064	132	3212	65	7377	99	5

defects — 5 pores — with a mean area not exceeding 7377 μm² and a mean size of 99 μm (Table 3).

The analysis confirmed a clear correlation between surface morphology (Figure 2) and internal defectiveness (Table 3). The increased number and area of defects in specimens with porous morphology indicates that surface condition may serve as an indicator of internal structure. The reduction in defectiveness in Specimens Nos 7 and 8 demonstrates the possibility of optimising printing parameters to achieve a stable structure with minimum defects. Specimens Nos 7 and 8 were selected for further investigation as they exhibit the best surface condition and minimum defect area and number.

Metallographic examination of Specimen No. 7 at ×50 magnification revealed that the metal structure consists of crystallites with different etching degrees, 40–300 μm wide (Figure 4, *a*). The structure demonstrates a pronounced zonality arising from local thermal gradients and non-uniform cooling. At the macro level (Figure 4, *a*), a coarse, non-uniform structure is observed consisting of columnar α-phase crystallites and residual β-phase that did not fully transform. At the micro level (Figure 4, *b*), elongated α-lamellae oriented in one direction are identified, with thin β-phase interlayers between them. This morphology is indicative of martensitic transformation of the β-phase due to rapid cooling in the upper layers. SEM imaging (Figure 4, *c*) confirms the presence of a basket-weave structure with α-lamellae 0.8–1.5 μm thick. Such non-uniformity may result in differences in properties: fine-grained regions with elongated α-lamellae potentially exhibit higher hardness, whereas coarse-grained regions are more prone to local failure due to porosity or microcracks.

Investigation of Specimen No. 8 established that the metal structure at ×50 magnification is more balanced (Figure 4, *d*). It consists of crystallites with different etching degrees, 30–300 μm wide, growing in the direction of the heat flow, while β-phase is partially stabilised in the interlamellar volume. At the micro level at ×500 magnification (Figure 4, *e*), an (α+β)-structure is identified with α-lamellae between which thin β-phase interlayers are located. SEM imaging at ×5000 magnification (Figure 4, *f*) confirms dense packing of α-lamellae 0.6–1.1 μm thick and uniform distribution of the β-phase, forming a balanced (α+β)-morphology (Figure 4, *g*). Such a structure indicates more stable cooling

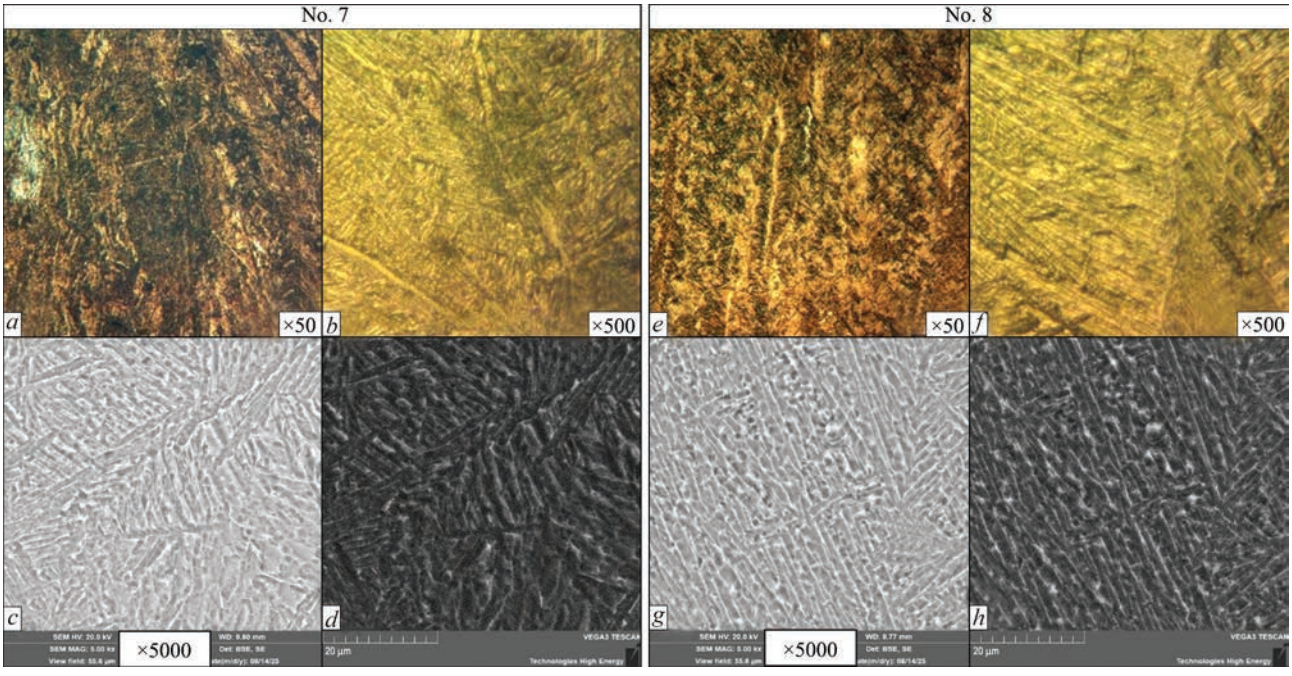

Figure 4. Microstructures of specimens: No. 7 (*a–d*); No. 8 (*e–h*)

Table 4. Chemical composition of specimens (XRF), wt.% (Ti — base)

Designation	Chemical element						
	Mg	Al	Si	V	Fe	Ni	Zr
Specimen No. 7	–	5.059	0.058	4.177	0.102	0.022	0.01
Specimen No. 8	–	5.644	0.062	4.091	0.104	0.046	0.0076
VT6 alloy [14]	≤ 0.30	5.3–6.8	≤ 0.1	3.5–5.3	≤ 0.6	≤ 0.08	≤ 0.30

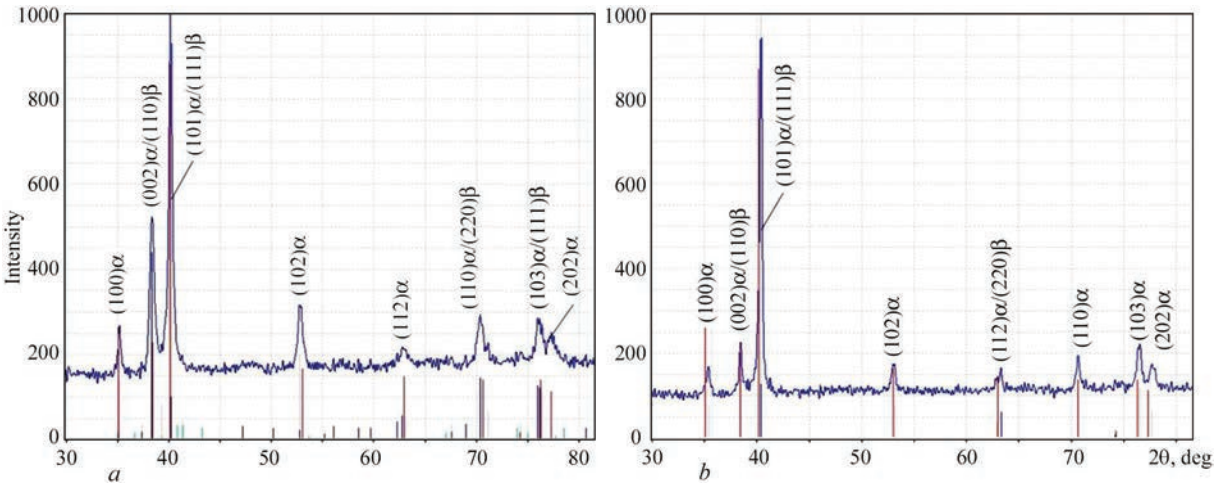

Figure 5. XRD results of specimens: *a* — No. 7; *b* — No. 8

conditions and a more uniform thermal cycle, providing better property homogeneity.

INVESTIGATION OF CHEMICAL AND PHASE COMPOSITION OF SPECIMENS

The investigations showed that chemical composition significantly influences the microstructure of specimens, particularly the Al content, which determines α-phase stability and the phase balance.

According to the data in Table 4, it was established that in Specimen No. 7 the Al concentration (5.059 %) is below the standard range (5.3–6.8 %), which causes a shift in equilibrium towards the β-phase and structural non-uniformity. In Specimen No. 8, the Al content (5.644 %) conforms to the standard, ensuring a stable lamellar α-phase. Thus, Specimen No. 8 has the required chemical composition for the formation of a balanced (α+β)-microstructure, while Specimen No. 7 exhibits phase imbalance due to Al deficiency.

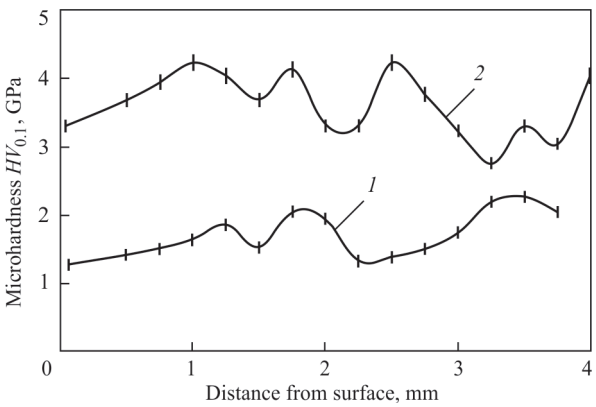

Figure 6. Microhardness ($HV_{0.1}$) variations in specimens, No.: *1* — 7; *2* — 8

X-ray phase analysis allowed the phase composition of specimens to be determined, and the degree of crystallinity, structural purity, and the influence of chemical composition on phase equilibrium to be assessed.

XRD results (Figure 5, *a*) established that Specimen No. 7 exhibits α-phase with a hexagonal close-packed lattice and β-phase with a body-centred cubic structure, where the volume fraction of α-phase is 87±3 % and that of β-phase is 13±3 %. As shown in [15], a reduction in Al content leads to a shift in phase equilibrium towards the β-phase and reduces the morphological stability of the α-phase, which may adversely affect mechanical properties.

Specimen No. 8 demonstrates a clear coincidence of diffraction peaks with reference values (Figure 5, *b*). The intensity and sharpness of the reflections indicate a high degree of crystalline perfection of the phases. This is characteristic of a well-formed α-phase with a volume fraction of 90±3 %. The volume fraction of the β-phase is 10±3 %. The obtained α/β ratio is characteristic of VT6 alloy. As shown in [7] the high crystallinity and the absence of amorphous regions are indicative of a stable thermal crystallisation mode during EBM, ensuring homogeneity of phase composition and improved mechanical properties. This is consistent with the chemical analysis results, where the Al and V content in Specimen No. 8

is within the standard range (Table 4), promoting the formation of a balanced (α+β)-microstructure.

MICROHARDNESS MEASUREMENTS

To evaluate local mechanical properties, microhardness measurements were carried out for Specimens Nos 7 and 8 within the cross-section.

It was established that on the surface of Specimen No. 7 microhardness is $HV_{0.1}$ = 1.3 GPa and it gradually increases, reaching a maximum of $HV_{0.1}$ = 2.3 GPa at a distance of approximately 3.5 mm (Figure 6). This indicates structural non-uniformity of the material, a transition from a less stable surface zone to a more strengthened internal structure. This behaviour is explained by phase instability and reduced Al content, causing local differences in the α/β phase ratio. The mean microhardness of Specimen No. 7 is $HV_{0.1}$ = 1.8±0.5 GPa, which is reduced compared to typical values for VT6 alloy [9].

Specimen No. 8 demonstrates a significantly higher hardness level (Figure 6), ranging from $HV_{0.1}$ = 2.8 to 4.2 GPa. The mean microhardness value is $HV_{0.1}$ = 3.5±0.7 GPa, consistent with characteristic values for VT6 alloy of the Ti–6Al–4V alloying system [9] and indicative of a well-formed (α+β)-microstructure. Hardness fluctuations can be attributed to local features of the thermal cycle, which does not affect the overall structural stability.

DETERMINATION OF PRINTING MODES ENSURING THE BEST STRUCTURAL CONDITION

The results of the comprehensive analysis confirmed that the quality of thin-walled products is significantly dependent on the choice of EBM process parameters. When determining printing modes that ensure the best structural condition, it was established that Specimen No. 8 is distinguished by minimum defectiveness and a balanced microstructure with a uniform phase distribution. Its chemical and phase composition and microhardness values are consistent with the characteristic indicates for VT6 alloy.

Specimen No. 8 was printed at a speed of 500 mm/s and an energy density of 40 J/mm^3. Thus, the implemented process parameters can be considered rational for manufacturing thin-walled products from VT6 alloy. The obtained results are consistent with data from [7], where it is noted that optimisation of beam speed and energy in the EBM process is key to forming a fine-grained microstructure with a minimum defect level.

Despite the positive results obtained, the study has a number of limitations. In particular, the printing parameters were investigated for only one powder type. Microstructure analysis was carried out locally, without accounting for scale effects and complex product geometry. Furthermore, microhardness was used as an assessment of local mechanical behaviour without conducting a full range of mechanical tests. These aspects should be considered in the practical application of the obtained recommendations, as well as in further studies aimed at confirming the long-term operational reliability of the products.

CONCLUSIONS

1. The parameters of the additive electron beam process significantly influence the shape formation quality of thin-walled products. Elevated beam travel speeds in the range of 2000–6000 mm/s lead to unstable melting and increased porosity.

2. A correlation was established between additive process parameters, surface morphology, and the level of internal defectiveness of specimens. Optimisation of printing modes substantially reduces porosity and promotes the formation of a more uniform two-phase (α+β)-structure. The best structural indicates were demonstrated by Specimen No. 8, which is distinguished by minimum defectiveness and a balanced microstructure with uniform phase distribution.

3. It was determined that chemical composition is a decisive factor in the formation of the phase state and microstructural stability of VT6 alloy. Al deficiency (<5.3 %) in Specimen No. 7 causes a shift in phase equilibrium towards the β-phase (α-Ti — 87±3 %, β-Ti — 13±3 %) and increased structural non-uniformity. Specimen No. 8, whose chemical composition meets the standard requirements, exhibits a balanced α/β ratio (α-Ti — 90±3 %, β-Ti — 10±3 %) and high crystallinity of the structure.

4. Microhardness measurements confirmed the significant influence of microstructural condition on the local mechanical properties of VT6 alloy. Specimen No. 7 is characterised by reduced and non-uniform hardness values of $HV_{0.1}$ = 1.8±0.5 GPa, attributable to phase imbalance and structural non-uniformity. Specimen No. 8 demonstrates a higher microhardness level of $HV_{0.1}$ = 3.5±0.7 GPa, corresponding to the balanced (α+β)-structure, and is consistent with characteristic values for VT6 alloy. Hardness fluctuations can be attributed to local features of the thermal cycle, which does not affect the overall structural stability.

5. The printing mode of Specimen No. 8 can be considered the most rational from the point of view of achieving the best structural condition. Application of the mode with a beam travel speed of 500 mm/s and an energy density of 40 J/mm^3 provides for thin-walled products from VT6 alloy: a dense surface, a balanced (α+β)-microstructure, and mechanical properties consistent with literature data.

FUNDING

This work was funded within the framework of the targeted scientific research programme of the National Academy of Sciences of Ukraine on the topic "Development of resource-saving electron beam and plasma-arc additive technologies for manufacturing aerospace and rocket components for military applications from high-strength titanium alloys" (state registration number 0125U000353).

ACKNOWLEDGEMENTS

The authors are grateful to High Energy Technologies LLC (Kyiv, Ukraine) for technical support in conducting the research.

REFERENCES

1. Radhika, C. et al. (2024) A review on additive manufacturing for aerospace application. *Mater. Res. Express*, 11(**2**), 022001. DOI: https://doi.org/10.1088/2053-1591/ad21ad
2. Thomas, D., Gleadall, A. (2022) Advanced metal transfer additive manufacturing of high temperature turbine blades. *Inter. J. Adv. Manuf. Technol*., **120**, 6325–6335 DOI: https://doi.org/10.1007/s00170-022-09176-2
3. Whittaker, M. (2011) *Titanium in the gas turbine engine, book advances in gas turbine technology*. 315–335, DOI: https://doi.org/10.5772/21524
4. Drummer, D., Schmidt, M. (2025) *Progress in powder based additive manufacturing*. Springer Tracts in Additive Manufacturing. eBook. DOI: https://doi.org/10.1007/978-3-031-78350-0
5. Wang, F., Williams, S., Colegrove, P. et al. (2013) Microstructure and mechanical properties of wire and arc additive manufactured Ti–6Al–4V. *Metal. Mater. Transact. A*, **44**, 968–977. DOI: https://doi.org/10.1007/s11661-012-1444-6
6. Kishor, G., Mugada, K.K., Mahto, R.P. (2025) Wire arc additive manufacturing of titanium alloys for enhancing mechanical properties and grain-refinement. *Met. Mater. Inter*., **32**, 50–80. DOI: https://doi.org/10.1007/s12540-025-02004-8
7. Romero Reséndiz, L., Sánchez Cano, T., Naeem, M. et al. (2024) Mechanical and electrochemical properties comparison of additively manufactured Ti–6Al–4V alloys by electron beam melting and selective laser melting. *J. of Materials Eng. and Performance*, **33**, 9028–9038. DOI: https://doi.org/10.1007/s11665-024-09486-4
8. Matviichuk, V., Nesterenkov, V., Berdnikova, O. (2022) Determining the influence of technological parameters of the electron-beam surfacing process on quality indicators. *Eastern-European J. of Enterprise Technologies*, **1**, 21–30. DOI: https://doi.org/10.15587/1729-4061.2024.297773
9. Matviichuk, V., Nesterenkov, V., Berdnikova, O. (2024) Determining the influence of technological parameters of electron beam surfacing process on the microstructure and microhardness of Ti–6Al–4V alloy. *Eastern-European J. of Enterprise Technologies*, **1**, 15–21. DOI: https://doi.org/10.15587/1729-4061.2024.297773
10. Powder materials produced by LLC "MULTIFLEX" [in Ukrainian]. https://powdermet.com.ua/ (access date: 23.02.2026)
11. Matviichuk, V.A., Nesterenkov, V.M., Berdnikova, O.M. (2022) Additive electron beam technology for manufacture of metal products from powder materials. *The Paton Welding J.*, **2**, 16–25. DOI: https://doi.org/10.37434/tpwj2022.02.03
12. Matviichuk, V. (2025) *Additive electron-beam technologies for the production of metal products by the method of layer-by-layer melting using powder materials*: Synopsis of Thesis for Cans. of Tech. Sci. Degree. DOI: https://doi.org/10.13140/RG.2.2.26234.61129
13. Pan Wang, Wai Jack Sin, Mui Ling Sharon Nai, Jun Wei (2017) Effects of processing parameters on surface roughness of additive manufactured Ti–6Al–4V via electron beam melting. *Materials*, 10(**10**), 1121. DOI: https://doi.org/10.3390/ma10101121
14. *VT6-Grade5*.https://evek.org/vt6-vt6s-vt6ch-splav-truba.html *VT6-Grade 5* [in Russian]. https://evek.org/vt6-vt6s-vt6ch-splav-truba.html
15. Sahoo, S., Joshi, A.P., Yazar, K.U. et al. (2026) Fine-scale microstructure, elemental distribution, and dislocation substructure formation and their influence on post-deposition phase transformation in additive manufacturing of Ti–6Al–4V alloy. *J. of Materials Eng. and Performance*, **35**, 7411–7429. DOI: https://doi.org/10.1007/s11665-025-12207-0

ORCID

V.A. Matviichuk: 0000-0002-9304-6862,
V.M. Nesterenkov: 0000-0002-7973-1986,
M.O. Sysoev: 0009-0002-0654-3914

CONFLICT OF INTEREST

The Authors declare no conflict of interest

CORRESPONDING AUTHOR

V.A. Matviichuk
E.O. Paton Electric Welding Institute of the NASU
11 Kazymyr Malevych Str., 03150, Kyiv, Ukraine
E-mail: vl.matviichuk@gmail.com

SUGGESTED CITATION

V.A. Matviichuk, V.M. Nesterenkov, M.O. Sysoev (2026) Effect of process parameters of the additive electron beam process on the properties of thin-walled products from VT6 alloy. *The Paton Welding J*., **04**, 3–10.
DOI: https://doi.org/10.37434/tpwj2026.04.01

JOURNAL HOME PAGE

https://patonpublishinghouse.com/eng/journals/tpwj

Received: 23.12.2025
Received in revised form: 25.02.2026
Accepted: 11.04.2026

DOI: https://doi.org/10.37434/tpwj2026.04.02

CORROSION RESISTANCE OF VAPOUR-PHASE CONDENSATES (Cu–Y–Zr)–Mo IN ATMOSPHERIC CONDITIONS

V.G. Grechanyuk, I.M. Grechanyuk

Kyiv National University of Civil Engineering and Architecture. Ukraine, Kyiv, Air Force Avenue, 31

ABSTRACT

The corrosion resistance of composite materials in distilled water, which corresponds to the conditions of a humid environment, was studied. The conducted X-ray analysis of composite materials (Cu–Y–Zr)–Mo showed that corrosion damage is observed in areas with structural defects. It was established that the oxidation process becomes more intense with increasing molybdenum concentration in the condensates.

KEYWORDS: composite materials, structure, corrosion resistance, electron beam technology

INTRODUCTION

Various metallurgical processes, in particular, powder metallurgy methods are widely used to create composite materials (CM) [1–3]. Quite promising also is the method of electron beam evaporation of metals and their subsequent condensation in the vacuum developed at PWI in the 50s of the previous century. Application of this method allows creating CM, in which such important properties as dispersity and grain size can be purposefully changed, and the processes of material interaction with the substrate can be regulated, thus ensuring fulfillment of various requirements to the materials.

Analysis of the available materials and regularities of the change of their physical-chemical properties at different temperatures and under the influence of the environment shows the potential for copper-based CM application in different industries. Withstanding the temperature fluctuations well, having comparatively high corrosion resistance, high electrical and heat conductivity, the copper-based CM can be applied in radio engineering and computing technology. Their comparatively low cost, compared to alloys of noble metals determines the ability to use these materials as electrical contacts for various purposes. Up to the present time, a fairly large amount of factual information has been accumulated on producing and studying the copper-based CM [4, 5]. However, a number of properties of these materials which are important in the scientific and applied terms, have not been clarified completely. Such aspects as corrosion resistance, influence of structural factors, and dispersity on the physical and chemical properties of these materials are practically unstudied. At the same time, it is known that none of the materials can be accepted by industry without the above-mentioned characteristics.

INVESTIGATION PROCEDURE

Composite materials were produced by the method of electron beam evaporation and subsequent condensation on a rotating substrate in vacuum in UE-187 unit [6, 7]. Cylinders from CaF_2 compound were used to form a separation layer on the substrate, on which the vapour flow condensation was performed. Owing to the separation layer, the condensate was readily separated from the substrate, and it was used for investigations. The substrate for condensation was plate steel of St3 grade. The surface of the blank (substrate), onto which the vapour flow was condensed, was treated up to the roughness of 0.63–1.2 R_a.

Such a technology enabled producing condensates with a layered structure with alternating copper layers alloyed by zirconium and yttrium and molybdenum layers. Condensates of alloyed copper (Cu–0.05–0.1 % Zr–0.05–0.1 % Y) with different content of molybdenum from 7.62 to 46.7 wt.%) were used to study the corrosion resistance.

The serviceability of any materials, including contact ones, depends on external factors. The rate of the corrosion processes, which may run on the composite material surface, is influenced, primarily, by air humidity. In this connection, corrosion studies of (Cu–Zr–Y)–Mo CM were conducted in distilled water in this work, which corresponds to 100 % humidity according to GOST 24927–81 [8].

The base for conducting investigations of the corrosion properties of (Cu–Zr–Y)–Mo CM was the structural approach, as during the corrosion processes the composition and structure of the surface layer change. The condensate microstructure was studied by the method of scanning electron microscopy using Cam Scan 4 microscope. Transverse microsections of samples in as-deposited condition and after corrosion tests were produced by a generally accepted procedure [9] by grinding on abrasive (or sand) paper with 80–2400 μm grain size. Final polishing of the microsection surface was performed by diamond paste with grain size of 1 μm, and aluminium oxide-based aqueous suspension with grain size of 0.3 μm. The structure was studied in the back-scattered electron mode without additional etching of the microsection surface.

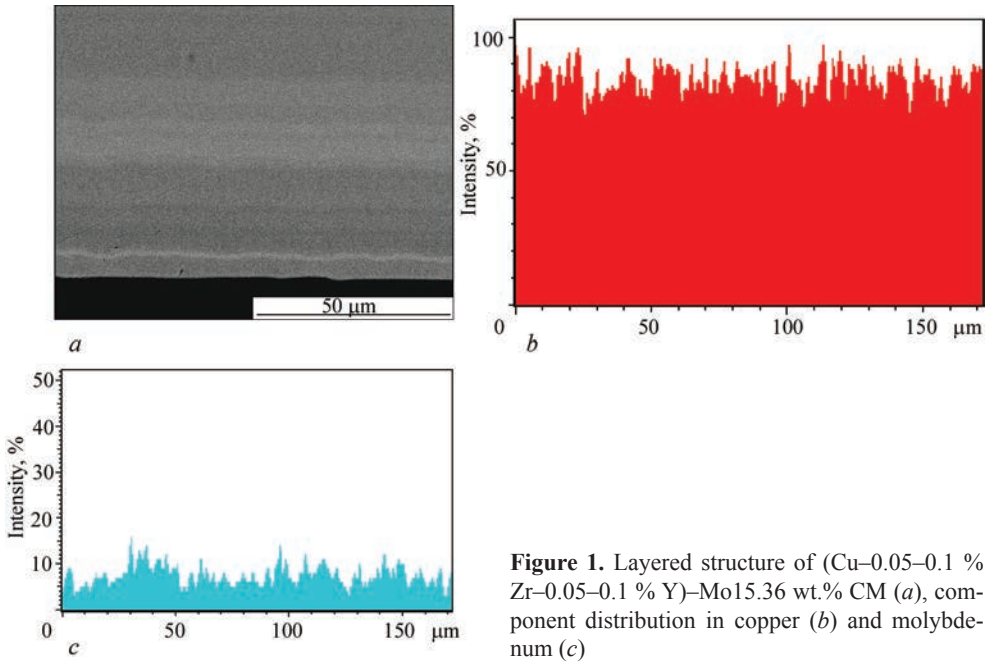

Figure 1. Layered structure of (Cu–0.05–0.1 % Zr–0.05–0.1 % Y)–Mo15.36 wt.% CM (*a*), component distribution in copper (*b*) and molybdenum (*c*)

EXPERIMENTAL RESULTS

Conducted electron microscopy studies of samples not yet subjected to corrosion testing in distilled water, revealed an absence of any film on the surface and in the section normal to the surface of as-deposited samples (Figure 1, *a*).

The structure of all the condensates is layered: molybdenum-enriched copper layers (of lighter colour) alternate with the copper layers with smaller molybdenum content. In the section normal to the surface, fluctuations of the copper and molybdenum content are observed over the entire sample thickness (Figure 1, *b*, *c*).

A nonuniform distribution of copper and molybdenum is observed not only between the layers, but also inside the layers. Such a regularity is characteristic for all the studied samples. X-ray analysis allows stating that copper is the main phase in as-deposited samples. In samples with a small content of molybdenum, pure copper is recorded, and additional reflection lines are absent. In samples with molybdenum content higher than 15 wt.% there is one more additional line with

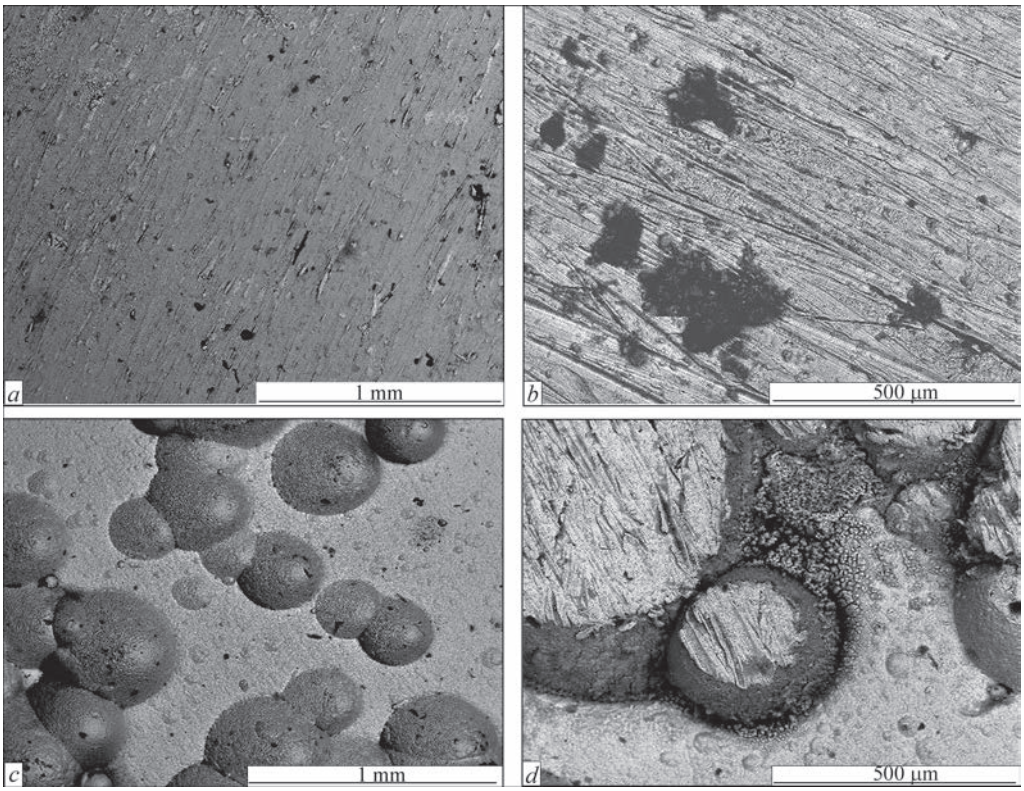

Figure 2. As-deposited the surface before (*a*, *c*) and after (*b*, *d*) corrosion testing from the side of: *a*, *b* — substrate; *c*, *d* — evaporator-pool

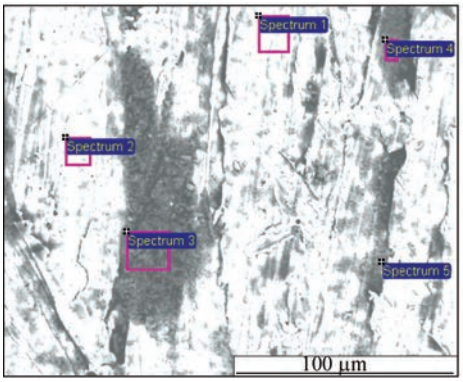

Spectrum	O	Cu	Mo
Spectrum 1	17.16	80.45	2.39
Spectrum 2	16.79	80.88	2.33
Spectrum 3	27.80	67.99	4.21
Spectrum 4	22.47	73.29	4.24
Spectrum 5	26.19	70.81	3.00

Figure 3. Element distribution on the surface of (Cu–0.05–0.1 % Zr–0.05–0.1 % Y)–Mo15.36 wt.% condensate after corrosion testing in distilled water

Table 1. Reduction in the weight of (Cu–0.05–0.1 % Zr–0.05–0.1 % Y)–Mo CM samples in distilled water

Chemical composition of the samples, wt.%		Test time, h				
Cu	Mo	20	40	60	80	100
		Sample weight reduction, 10^5 g/mm^2				
Balance	7.62	0.75	0.05	0.20	0.05	0.50
	15.36	0.95	0.25	0.95	0.90	0.85
	28.90	1.50	1.25	1.35	1.70	1.20
	46.70	1.95	1.55	1.65	1.80	1.30

interplanar distance d = 2.22 Å, alongside the copper reflection line.

The condensate surface after corrosion tests in distilled water is characterized by damage in those areas, which have mechanical defects and structural defects due to CaF_2 separation layer and drops ejected from the liquid pool during condensation (Figure 2). For comparison, Figure 2 gives the results of structural analysis before and after the corrosion tests. In as-deposited condition certain mechanical defects are observed on the condensate surface contacting the substrate, which are due to the substrate roughness and defects formed as a result of drop transfer during evaporation of the separation CaF_2 layer. On the opposite surface, from the side of the evaporator pool, drops are observed, which were formed by solid particle emissions from the evaporator pool, which can be the oxides formed by impurities in commercial-grade copper and molybdenum.

Table 2. Weight and depth corrosion indices for (Cu–0.05–0.1 % Zr–0.05–0.1 % Y)–Mo CM in distilled water

Chemical composition of the samples, wt.%		K_{wt}, g/m^2·h	П, mm/year	Corrosion resistance point
Cu	Mo			
Balance	7.62	0.004	0.00343	Fairly resistant 2
	15.36	0.050	0.0429	Resistant 4
	28.90	0.080	0.0687	Resistant 5
	46.70	0.090	0.0770	

During corrosion the surface in the points of defect formation is more intensively destroyed (Figure 2). On the surface from the side of the evaporator pool fracture runs on the drop-condensate interfaces, where discontinuities between the drops and the condensate base are present. On the mentioned discontinuities fracture propagates in-depth the condensate (Figure 2, *d*). Studies of the chemical composition of the surface after corrosion testing in distilled water showed that the surface is characterized by the presence of a large amount of copper, oxygen and a small amount of molybdenum (Figure 3). Reduction of molybdenum content is relat-

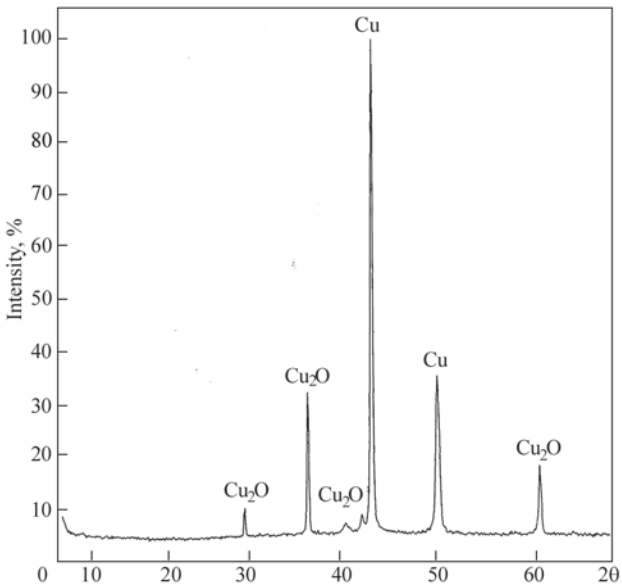

Figure 4. Fragment of an X-ray pattern of (Cu–0.05–0.1 % Zr–0.05–0.1 % Y)–Mo15.36 wt.% CM after testing in distilled water

ed to molybdenum corrosion activity and its transition into the solution as a more active metal.

Results of X-ray investigations (Figure 4) confirm formation of cuprum (I) oxide Cu_2O on the surface. In addition, weak additional lines with d = 2.22 Å and d = 1.11 Å are observed in the samples, which can be due to the presence of molybdenum and its oxide MoO_3 in the samples.

These data confirm the mechanism of corrosion processes, which is characterized by formation of copper-molybdenum galvanic couple. The more active metal (molybdenum) diffuses to the surface, it is ionized and when interacting with oxygen from the solution it forms MoO_3 film on the surface. Presence of molybdenum oxide (VI) on the sample surface reduces the corrosion resistance, as the molybdenum oxide film has a low continuity and cannot perform the protective functions. In this connection, the corrosion process spreads in-depth. Corrosion resistance is the smallest for material with the highest molybdenum content. This is indicated by the greatest intensity of the X-ray spectra.

Gravimetric studies were conducted for 100 h with determination of the weight change every twenty hours. As shown by the investigation results, the weight losses increase noticeably for samples with a high content of molybdenum (Table 1).

Weight and depth corrosion indices calculated by the results of gravimetric dependencies, are indicative of reduction of the CM corrosion resistance depending on molybdenum concentration from 7.92 to 46.7 wt.%. The corrosion resistance rating on a ten-point scale is 2 with molybdenum concentration of 7.62 wt.% according to DSTU 13819-68 [10], and it is reduced to 4–5 when molybdenum concentration is increased to 46.7 wt.% (Table 2).

CONCLUSIONS

1. Conducted research showed an absence of any film on the surface and in the section normal to the surface of composite materials (Cu-0.05–0.1 % Zr–0.05–0.1 % Y)–Mo in as-deposited condition.

2. The structure of all the condensates is layered: molybdenum-enriched copper layers alternate with copper layers, in which the molybdenum content is lower.

3. After corrosion testing in distilled waster the condensate surface is characterized by damage in those areas, where mechanical defects and structural defects are present.

4. It was determined that with increase of molybdenum concentration the corrosion resistance of all the samples in distilled water is reduced. The corrosion resistance point is the highest for CM with molybdenum content of 7.62 wt.%.

REFERENCES

1. Baglyuk, G.A., Grypachevskyi, O.M., Volfman, V.I., Uskova, N.O. (2009) Thermal synthesis of powder master alloy Fe–Mn–C–Cu. *Metaloznavstvo ta Obrobka Metaliv,* **3**, 43–47 [in Ukrainian].
2. Konoval, V.P., Umanskyi, O.P., Bondarenko, O.A. et al. (2024) Technology of producing and properties of composite powders based on titanium-chrome diboride for coating deposition. *Poroshkova Metalurhiya,* **1–2**, 3–16 [in Ukrainian].
3. Kulikov, L.M., Ragulya, A.V., Poznii, A.P. et al. (2023) Influence of air humidity on dielectric properties of micron powders of 2D molybdenum disulphide. *Poroshkova Metalurhiya,* **9–10**, 3–20 [in Ukrainian].
4. Artyukh, Ya.Yu., Grechanyuk, V.G. (2006) Corrosion resistance of composite materials based on copper and molybdenum produced by electron beam technology in the temperature range of 20–800 °C. *Electrical contacts and electrodes. Series Composite Materials.* Kyiv, 267–272.
5. Grechanyuk, I.N., Artyukh, Ya.Yu., Grechanyuk, V.G. et al. (2005) Study of corrosion and erosion resistance of composite materials based on copper and molybdenum. *Naukovi Visti NTUU KPI,* **6**, 46–50.
6. Grechanyuk, N.I., Kucherenko, P.P. (2005) *Unit for electron beam deposition of coatings.* Pat. 2265078 RF. Publ. 12.07.2005.
7. Grechanyuk, N.I., Mamuzic, I., Bukhanovskii, V.V. (2007) Production technology and physical, mechanical and performance characteristics of Cu–Zr–Y–Mo finely-dispersed microlayer composite materials. *Metallurgiya*, 46(**2**), 125–28.
8. (1980) *Unified procedure of laboratory tests of effectiveness of corrosion inhibitors in water systems.* Riga, Institute of Inorg. Chemistry, AS Lithuanian SSR.
9. Zagorodnii, V.V. (2019) *Local methods of investigations: Manual for students of speciality 105 "Applied Physics and Nanomaterials"*. Kyiv, KPI.
10. (1969) GOST 13819–68: *Corrosion of metals. Ten-point scale of corrosion resistance.*

ORCID

V.G. Grechanyuk: 0009-0008-8771-3092,
I.M. Grechanyuk: 0000-0001-7341-3170

CONFLICT OF INTEREST

The Authors declare no conflict of interest

CORRESPONDING AUTHOR

V.G. Grechanyuk
Kyiv National University of Civil Engineering and Architecture. Ukraine, Kyiv, Air Force Avenue, 31
E-mail: eltechnic777@ukr.net

SUGGESTED CITATION

V.G. Grechanyuk, I.M. Grechanyuk (2026)
Corrosion resistance of vapour-phase condensates (Cu–Y–Zr)–Mo in atmospheric conditions.
The Paton Welding J., **04**, 11–14.
DOI: https://doi.org/10.37434/tpwj2026.04.02

JOURNAL HOME PAGE

https://patonpublishinghouse.com/eng/journals/tpwj

Received: 06.01.2026
Received in revised form: 18.02.2026
Accepted: 14.04.2026

DOI: https://doi.org/10.37434/tpwj2026.04.03

PRODUCTION AND REFINING OF METALLURGICAL SILICON TO SOLAR-GRADE SILICON (REVIEW)

G.G. Didikin

E.O. Paton Electric Welding Institute of the NASU
11 Kazymyr Malevych Str., 03150, Kyiv, Ukraine

ABSTRACT

Studies of refining MG-Si silicon by metallurgical methods show that each method is selective in removing one or a small group of impurity elements. Particular attention is paid to the purity of silicon by boron, the content of which should not exceed 0.3 ppm_w. Evaporation of P or B is possible, but it is most often a slow process and can be accompanied by a loss of Si. Solvent refining has proven effective in removing impurities, with Al being a suitable alloying agent. In order to take advantage of the high throughput and low cost benefits of metallurgical processing methods, combinations of methods must be used, either sequentially or simultaneously, to produce a product that is consistent with solar-grade SoG–Si. Impurities in MG–Si are classified as segregable and insoluble. Single acid leaching removes only certain impurities. In practice, sequential or mixed acid leaching is used. Adding oxidizing agents to acidic leachers increases the efficiency of impurity removal. External fields (ultraviolet radiation, ultrasonic field, and oxygen pressure leaching) or the introduction of cracks/porous structures and thermal pretreatment can improve impurity removal. In the electron beam remelting of metallurgical silicon, purification occurs by evaporating impurity elements from the melt surface in a vacuum. Refining is based on the process in a high vacuum and the difference in vapor pressure of different impurity elements, whose vapor pressure is higher than that of silicon. The method of electron beam remelting of metallurgical silicon in conjunction with oxidative refining makes it possible to purify up to the level of 5–6 N.

KEYWORDS: metallurgical silicon, slag treatment, leaching, electron beam melting, vacuum degassing, solar-grade silicon, impurity elements, segregation

INTRODUCTION

In this review the attention is focused on processing and refining silicon for photoelectric devices (PhE). The dominant semiconductor material in photoelectric devices is the silicon grade for semiconductors (SOG–Si). The ultrapure silicon (polysilicon) is produced on the commercial scale by distillation and thermal decomposition of light silicon compounds — trichlorosilane ($SiHCl_3$) and monosilane (SiH_4). However, this is a high-cost product, 30 to 50 times more expensive than metallurgical silicon. MG–Si metallurgical silicon with 98.5 % Si purity is produced by carbothermic reduction in a submerged electric arc furnace at the temperature of 1500–2000 °C from lump quartz of appropriate purity and carbon raw material. The general scheme of the reduction reactions has the following form:

$$SiO_2(s) + 2C(s) \rightarrow Si(l) + 2CO(g). \quad (1)$$

Silicon yield in the form of metallurgical silicon produced by carbothermic reduction is up to 90 %, the remainder is silicon dioxide vapor. Produced metallurgical silicon requires further purification (process of extraction up to obtaining solar-grade SOG–Si) with the required purity of 7 N. Effectiveness of solar batteries decreases, because of the presence of impurities in silicon, which shorten the carrier service life in the silicon solar element and disturb the electric energy generation. Owing to its low cost, simplicity of operation and control hydrometallurgy is believed to be a promising method of producing solar-grade silicon (SOG)–Si from metallurgical quality silicon (MG–Si). Metallurgical refining of MG–Si [1, 2] includes oxidative refining [3–5], hydrometallurgical processes [6, 7], vacuum refining [8] and directional crystallization [9, 10]. Most of the soluble impurities are removed in the hydrometallurgical process, carbon and boron are removed by oxidative refining, and P, Ca, Al — by vacuum cleaning (Figure 1). The remaining impurities are removed by directional crystallization. The final product is single-crystal silicon and high-purity solar-grade polysilicon (SOG–Si) (Table 1) [11–15].

Siemens process is a reaction with hydrogen chloride to produce volatile trichlorosilane ($SiHCl_3$) by hydrochlorination of metallurgical silicon in a reactor with a pseudo sparse layer [16] with its further distillation and vapour-phase deposition of silicon by $SiHCl_3$ decomposition.

The main reactions are:

$$Si + 3HCl = HSiCl_3 + H_2, \quad (2)$$

$$H_2 + HSiCl_3 = Si + 3HCl. \quad (3)$$

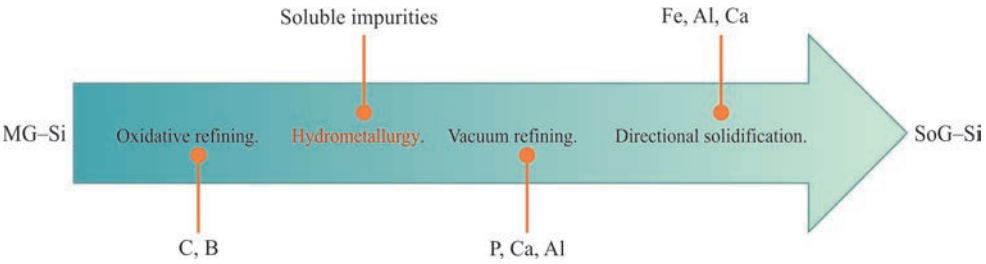

Figure 1. Scheme of production of solar-grade silicon by the metallurgical refining method [15]

Table 1. Limit concentrations of impurities in MG-Si and SoG–Si

Elements		Al	Fe	Ca	Mg	Mn	Cr	Ti	V	Zr	Cu	B	P	C	O
MG–Si	%	2	5	1	0.1	0.05	0.05	1.6	0.01	0.01	0.01	0.08	0.05	0.6	3
SoG–Si	ppm_w	0.1	0.1	0.3		0.1	0.1	0.01	0.1	0.1	0.1	0.3	0.1	3	10

The Union Carbide Process is an alternative silicon purification process developed at Union Carbide. After trichlorosilane transformation into monosilane (SiH_4), it is deposited similar to the Siemens process. The refining effect in the iodide process is determined by the fact that the impurities present in silicon being purified, during their interaction with gaseous iodine do not form any volatile iodides and remain in the unreacted residue. The metal deposition rate grows continuously with increasing thread temperature.

Solar-grade SILICON, METALLURGICAL PURIFICATION ROUTE

Reaction of carbothermic purification of silicon dioxide (1) shows that the raw material for MG–Si production covers only silicon and carbon reducing agents, and that they are the main impurity sources in MG–Si. Impurities in MG–Si include nonmetallic (B, P, C and O) and metallic elements (Fe, Al, Ca, Ti, Mn, V, Cu, Cr, etc.); Fe, Al and Ca being the dominating impurities (Table 1). The above-mentioned impurities are classified as segregable and insoluble: segregated impurities (Fe, Al, Ca, Ti, V, Cu, and Cr), and nonmetallic elements C and O [17, 18]. Segregable impurities deposit on grain boundaries during MG–Si solidification. During MG–Si crushing these impurities become exposed on the surface of the powder granules and are removed by acid leaching [19].

ACID LEACHING

H_2SO_4, HCl, HNO_3, HF, CH_3COOH acids and their mixtures are used for MG–Si purification by leaching with addition of oxidizers and by using ultraviolet radiation, ultrasound and oxygen pressure. H_2SO_4 acid demonstrated high activity only for lowering the carbon content. Fe and Al impurities cannot be removed completely by H_2SO_4 and HNO_3 acids. HCl acid removes Al and Ca from MG–Si up to 70–85 [7]. HF acid effectively removes the impurities, has high chemical activity with SiO_2, removes hidden impurities, but Fe, Al and Cu removal has its limitations [20]. Sequential acid leaching with H_2SO_4, HNO_3, HCl, and HF, and mixed acid leaching combine the advantages of different acids for impurities removal from MG–Si to the purity of 99.90 %. The most effective is the HCl + HF mixture.

During the hydrometallurgical process oxidizers are added to remove impurities from MG–Si. In works [21, 22] MG–Si was purified by mixtures of HF solutions with H_2O_2 additives, purification effectiveness reached 99.99 %, degree of B and P removal was moderate. When $AgNO_3$ was added to HF solutions, MG–Si purity increased to 99.98 % [22, 23]. $AgNO_3$ + H_2O_2 + HF combination effectively removes B and P impurities. The authors of work [24] crushed MG–Si to <53 μm and conducted leaching in a mixture of HNO_3 and HCL acids: removal of Fe, Al, Zn, Cu impurities was equal to 90 % (except for B and P), and silicon of ~99.98 % purity was produced. Nanosized silicon powders were leached by a solution of HF, HCl and HNO_3 [25], and silicon purity of 99.999 % was achieved. Thus, producing SOG–Si silicon from MG–Si is possible by combining acid leaching, oxidative purification, vacuum purification and purification by hardening. External fields — ultraviolet radiation, ultrasonic field and processing by leaching under oxygen pressure in the hydrometallurgical process improve removal of impurities from MG–Si to silicon purity of 99.995 %.

To remove internal impurities by acid leaching porous structures were created in MG–Si, and a purity of >99.99 % was achieved using acid leaching [26]. Porous silicon was produced under the effect of vapours of a mixture of HF/HNO_3 or $HF/H_2O/HNO_3$ acids [27–29]. Preprocessing by thermic oxidation weakens the bonds between the impurities and Si, and silicon of 99.996 % purity was produced after processing by

HF leaching [30], and a combination of ultrasonic and thermal processing enables producing silicon of 99.995 % purity.

SECONDARY REFINING PROCESSES

These processes include gas blowing, slag treatment, plasma cleaning and solvent cleaning. The most suitable secondary refining processes are slag and solvent cleaning. Slag oxide systems absorb, separate and remove the impurities from MG–Si. The process of solvent cleaning (alloying) is based on the principle of fractional crystallization [31]. In this process the metals dissolve in molten silicon, forming an alloy, and because of the low thermodynamic stability of some impurities in MG–Si their segregation coefficients are low, so that impurities removal from MG–Si can be improved.

SLAG TREATMENT OF SILICON MELT

Purity of solar-grade silicon (SOG–Si) should reach 99.9999 %. As the method of slag refining has such characteristics, as low cost, low power consumption, simplicity of operation and commercial production, it is believed to be one of the important methods of metallurgical cleaning of solar-grade silicon (SOG–Si). Paper [32] presents a comparison and discussion of the effectiveness and mechanism of removal of impurities in the binary, multicomponent and alloy-slag systems of slag, which provides a theoretical substantiation for researchers as to SOG–Si production by the method of slag refining. The main unfavourable impurities in MG–Si for SOG–Si production are Fe, Al, Ca, Ti, B and P. MG–Si purification is conducted by slag in the molten state: by calcium oxide or certain mixtures with CaO (SiO_2–Na_2O, SiO_2–CaF_2, SiO_2–$CaCl_2$). Metal or nonmetal impurities from MG–Si are oxidized and move into the slag phase [33]. MG–Si pretreatment by slags with further acid leaching by HCl provides higher productivity for removal of Fe, Al, Ca, Ti, Mn, B, and P [34–36]. In work [37] treatment by CaO–SiO_2–$CaCl_2$ slag and acid leaching were used to remove from MG the B impurities in the form of gaseous BOCl boride to its residual content of 1.37 ppm. After leaching by HCl + HF acid mixture B content in MG–Si decreased from 3 wt.% to 0.81 ppm_w.

VACUUM DEGASSING OF THE MELT

Such methods as vacuum degassing (VD), vacuum arc degassing or vacuum oxygen decarburization are widely used in the metallurgical industry for steel refining [38]. In this process differences in vapour pressure at high temperatures specific for each element are used for impurity evaporation from the metal melt. The same principle was studied for silicon in a number of investigations. Figure 2 shows the change in standard vapour pressure of pure substances depending on temperature, calculated by the thermodynamic data. Effective removal of phosphorus, calcium and aluminium is reported. The behaviour of phosphorus, which is difficult to remove from silicon, was particularly studied [39–42].

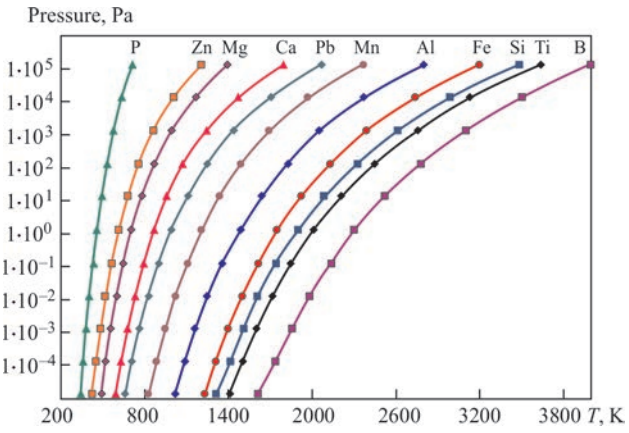

Figure 2. Changes in standard vapour pressure of pure substances depending on temperature

The kinetic criterion of volatility for vacuum refining was developed by Olette [44]:

$$\alpha = \frac{\gamma_i^{00} p_i^0}{p_{\mathrm{Si}}^0} \left(\frac{M_{\mathrm{Si}}}{M_i} \right)^{1/2}, \qquad (4)$$

where $p_{Si}^{\ 0}$ i $p_i^{\ 0}$ are the vapour pressures of pure silicon and impurities at this temperature, and γ_i^{00} is the Henrian coefficient of activity for the impurity. M_{Si} and M_i are the atomic weights of silicon and the impurity, respectively. At $\alpha > 1$ the impurity can be removed practically completely by VD method, and at $\alpha < 1$ vacuum refining is ineffective. When α is close to 1 silicon and the impurity evaporate simultaneously.

In study [45] phosphorus removal is described for different temperature and pressure conditions. In the work the authors report removal of P, Al, Ca and Mn from silicon during electron beam vacuum treatment of MG–Si (Table 2). They point to the existence of an interaction between the impurities in the melt, resulting in VD effectiveness, which depends on the initial composition of the melt. The authors of work [46] reported removal of phosphorus and other elements to 99 % (except for boron) in the experiments with the electron beam. Results obtained during MG–Si purification by melting in the electron beam furnace are as follows: a material with impurity concentration below 2 ppm_w was produced [47] (excluding boron). Phosphorus removal exceeded 98 % (0.4 ppm_w). Figure 3 shows the top view of one of the samples. Chemical analysis results are given in Table 3.

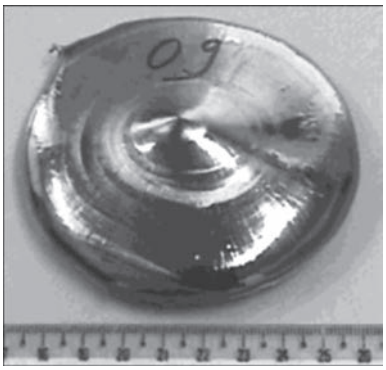

Figure 3. Top view of a crushed and leached MG–Si sample after melting in EBF [48]

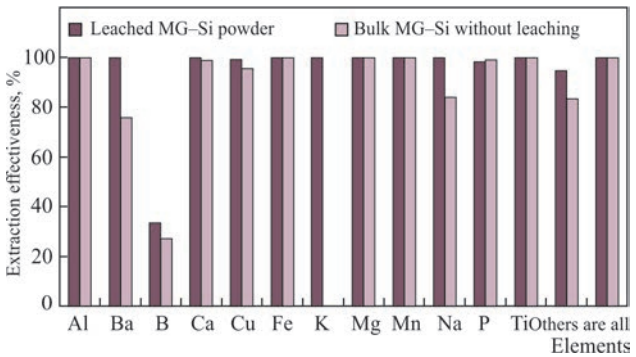

Figure 4. Effectiveness of impurity removal from leached MG–Si powder and bulk MG–Si without leaching

The extraction effectiveness for all the impurities is presented in Figure 4. Cleaning is more effective for elements with the vapour pressure closer to or higher than that of silicon. Boron was not removed, as its pressure is much lower than that of the silicon vapours. Difficulties of boron removal consist in its coefficient of segregation in silicon (k = ~ 1), which also complicates its removal using the process of unidirectional crystallization. Plasma melting in an oxidizing atmosphere (O_2, CO_2 or H_2O) is usually applied to remove boron. In this process boron is converted into an oxide form, increasing its vapour pressure [48–50]. Figure 5 gives the dependencies on melting time by the rate of P, Ca and Al removal in vacuum at temperatures of 1723 and 1823 K [51].

For the metallurgical methods of production of solar-grade silicon, it is necessary to use bidirectional

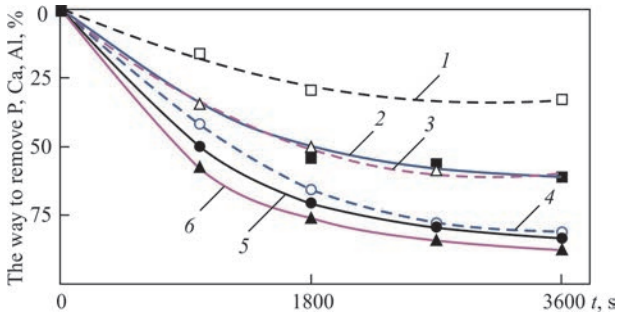

Figure 5. P, Ca and Al removal in the vacuum at 1723 and 1823 K as a function of melting time: *1*, *2* — Al; *3*, *6* — Ca; *4*, *5* — P; *1*, *3*, *4* — 1723 K; *2*, *5*, *6* — 1823 K [49]

crystallization to remove the Al, Ca, Fe and Ti meal impurities. In study [52] the synergic effect of chlorination by adding trace quantities of $MgCl_2$ at the stage of refining by the method of electron beam melting and directional crystallization allows removing these impurities to ultralow concentrations using chemical and physical processes during one-time melting. At the stage of directional crystallization, caused by the electron beam, the high temperature gradient inside the melt and the high-voltage electric field enhance the segregation. As a result, the total content of metal impurities in the ingot decreases from 647.11 to less than 0.60 ppm_w. In particular, Al, Fe and Ti content is below 0.10 ppm_w.

Production of silicon solar elements envisages development of the process of processing silicon from used photoelectric elements (PhE). Silicon in PhE is alloyed with different elements. Work [53] is a study of processing silicon from crushed solar elements using the vacuum purification process. The rejected solar elements after annealing are treated by acid etching, resulting in demetallized silicon fragments. Vacuum purification of these silicon fragments showed the following content of, ppm_w: phosphorus — 11.67, boron — 1, silver — 96 and tin — 136, the content of other metal impurities being lower. It is shown that Sn, Ag, O, N and Mg can be removed from the silicon melt by short-term vacuum refining. As the vacuum refining process is not limited by thermodynamic equilibrium, this promises complete removal of all the volatile impurities and then this process has a high

Table 2. Results of vacuum treatment of liquid silicon

Element	P, Pa	T, °C	Time, min	Removal, %	Literature
P	0.5	1600	60	22–42	52
Ca				10–31	
Al				6–22	
Mn				27–32	
P	10^{-2}–10^{-4}	Not specified	20	98–99	57
P	0.012–0.046	1600	120	99	56

Table 3. Chemical analysis before and after silicon melting, final purity and effectiveness of impurity removal

Impurities	Powder of leached MG–Si			MG–Si in bulk form without leaching		
	Before melting, ppm_w	After melting, ppm_w	Extraction effectiveness, %	Before melting, ppm_w	After melting, ppm_w	Extraction effectiveness, %
Al	53.00	0.09	99.83	110.00	0.44	99.60
Ba	11.00	0.00	100.00	0.04	<0.01	>75.61
B	15.00	10.00	33.33	10.00	7.30	27.00
Ca	185.00	0.02	99.99	26.00	0.31	98.81
Cu	1.80	0.01	99.20	6.50	0.29	95.54
Fe	31.00	0.03	99.90	790.00	0.70	99.91
K	30.00		99.92	0.10	0.10	0.00
Mg	4.60	<0.01	>99.78	4.20	0.02	99.50
Mn	2.00	0.003	99.85	75.00	0.027	99.96
Na	480.00	0.04	99.99	0.33	0.05	83.94
P	23.00	0.41	98.20	38.00	0.39	98.97
Ti	3.00	0.002	99.93	42.00	0.087	99.80
Others	20.58	1.12	94.56	16.32	2.74	83.21
Total	844.98	1.766	99.79	1108.49	5.165	99.53
Final purity, %	99.92	99.99982	–	99.88	99.9995	–

chance of bringing the produced silicon to solar energy generation standards.

LIQUID SILICON PURIFICATION BY GASES OR WATER VAPOUR

During refining of molten MG silicon gases van be blown through the melt, which can react with impurity elements for slag formation and oxidation, or can be neutral to promote melt mixing. Gases were also used for transportation of solid substances (slags), liquids (moisture) or gases (gas mixtures) for a reaction with molten silicon and promotion of refining [54].

There is a large amount of silicon scrap from the electronic industry, which cannot be used for photoelectric additives, as its boron content is 10 times higher than that in MG-silicon [55]. Boron is removed in the gaseous form (BOH, BO, BH_2 and B_2O_2) by blowing wet gas through molten silicon at the temperature of 1500–1700 °C [56]. The authors of work [57] conducted experiments at 0.05 atm with boron and phosphorus evaporation at the flow rate of 1 l/min of Ar + 2.5 ml H_2O to remove boron in the form of BOH. Initial B and P content was equal to 5.7 and 9.4 ppm_w, after blowing for 50 min it was 2.1 and 3.2 ppm_w, respectively (Figure 6). When using MG–Si, B concentration was reduced to 0.3 ppm_w, and P concentration — to 7 ppm_w from the initial levels of 40–60 ppm_w [51, 52]. After the refining stage, the melt was subjected to directional solidification. The impurity content, except for B and P, was reduced to <0.1 ppm_w, and B level was lowered to <1 ppm_w.

SILICON PURIFICATION BY ALLOYING

Silicon refining by solvent is one of the metallurgical approaches to produce SoG–Si from MG–Si, using a metallic agent, acting as an impurity catcher during solidification after its fusion with Si. The impurities together with the intermediary are driven to the solidification front and remain in the liquid phase. The intermediary metal should have a high affinity to boron and phosphorus, having a low coefficient of segregation in silicon, should readily dissolve in liquid silicon and have a low solubility in solid silicon.

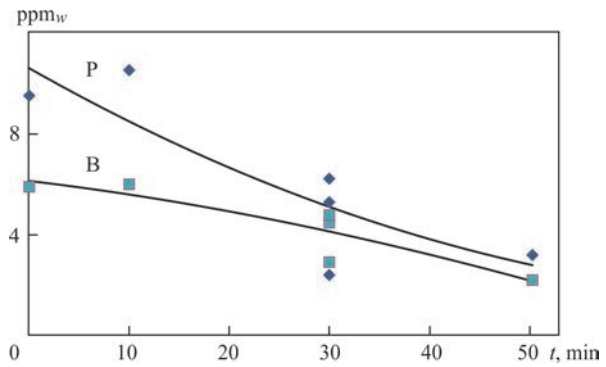

Figure 6. Change in the content of boron and phosphorus depending on treatment time: pressure — 0.05 atm; argon — 1 l/min; water — 2.5 ml [54]

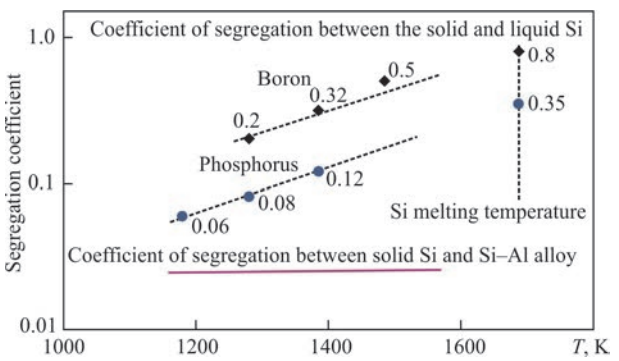

Figure 7. Temperature dependence of the coefficients of phosphorus and boron segregation between solid silicon and Si–Al melt

Table 4. Coefficient of segregation between solid silicon and Si–Al alloy at 1073 and 1273 K and the coefficient of segregation between solid and liquid silicon

Coefficient of segregation between solid silicon and Si–Al alloy			Coefficient of segregation between solid and liquid silicon in its melting point
Element	1073 K	1273 K	
Fe	$1.7 \cdot 10^{-11}$	$1.7 \cdot 10^{-9}$	$1.7 \cdot 10^{-6}$
Ti	$3.8 \cdot 10^{-9}$	$3.8 \cdot 10^{-7}$	$3.8 \cdot 10^{-6}$
Cr	$4.9 \cdot 10^{-10}$	$4.9 \cdot 10^{-8}$	$4.9 \cdot 10^{-5}$
Mn	$3.4 \cdot 10^{-10}$	$3.4 \cdot 10^{-8}$	$3.4 \cdot 10^{-5}$
Ni	$1.3 \cdot 10^{-9}$	$1.3 \cdot 10^{-7}$	$1.3 \cdot 10^{-4}$
Cu	$9.2 \cdot 10^{-8}$	$9.2 \cdot 10^{-6}$	$9.2 \cdot 10^{-4}$
Zn	$2.2 \cdot 10^{-9}$	$2.2 \cdot 10^{-7}$	$2.2 \cdot 10^{-5}$
Ga	$2.1 \cdot 10^{-4}$	$2.1 \cdot 10^{-4}$	$2.1 \cdot 10^{-3}$
In	$1.1 \cdot 10^{-5}$	$1.1 \cdot 10^{-5}$	$1.1 \cdot 10^{-4}$
Sb	$3.4 \cdot 10^{-5}$	$3.4 \cdot 10^{-3}$	$3.4 \cdot 10^{-2}$
Pb	$9.7 \cdot 10^{-5}$	$9.7 \cdot 10^{-4}$	$9.7 \cdot 10^{-3}$
Bi	$1.3 \cdot 10^{-6}$	$2.1 \cdot 10^{-5}$	$1.3 \cdot 10^{-4}$

Si–Al ALLOY SYSTEMS

Authors of works [58, 59] suggest cleaning silicon by fractional solidification from the molten solution of aluminium and silicon. Si–Al phase diagram is used in this process. If such a molten solution is slowly cooled, silicon precipitates from it in the form of plates. Acid leaching removes residual aluminium from the separated plates, the material melts and solidifies directionally. In work [60] the method of metallurgical purification of MG–Si by solidification of the aluminium and silicon melt was studied. A decrease in the content of boron and phosphorus to 314 and 96 ppm_w, respectively, was ensured. The produced silicon can be purified by directional solidification method to a purity of 6N. Mg, Sb, Sn, Zn and Cu can be used for alloying. In works [61, 62] aluminium, magnesium and copper as a metal-solvent were used for raw silicon purification. The Si–Al alloy system is one of the most promising solvents for Mg–Si purification after separation of the solidified silicon grains from Si–Al melt and further leaching by mixtures of aqua regia and H_2SO_4. Improved removal of boron in molten Si–Al solutions containing titanium was studied in [63], and in work [64] phosphorus removal was investigated, and an enhanced effect of segregation during solidification of silicon from Al–Si was confirmed. Figure 7 shows the results for boron and phosphorus and they are compared with the segregation coefficients at solidification of pure silicon [54]. Table 4 contains experimental results of test purifications of MG-silicon [64], solidified from Si–55.3 % Al alloy and Si–64.6 % Al under the conditions of 1273 and 1173 K, respectively [64]. Increased aluminium levels, which are higher than aluminium solubility in silicon at these temperatures, is attributable to the quantity of solvent entrapped by silicon crystals during growth, as shown in Figure 7. Effective removal of Fe, Ti, Cu, Mn and Ni impurities is shown in works [65, 66]. Other solvent systems were studied, such as Si–Cu, Si–Ga, Si–In, Si–Ag [67] and Si–Sn and Si–Zn [68], which showed interesting results, but so far only the Al–Si system has been used on the industrial scale for silicon refining.

Si–Cu ALLOY SYSTEMS

Si–Cu alloy has a relatively low melting temperature and a high affinity to a wide range of elements [69]. Using the process of refining by Cu alloying to remove B and P, it was determined that B and P are absorbed in the phase of Si–Cu alloy [70]. It was found that P adsorbs in the formed $CaCu_2Si_2$ phase after adding Ca to Si–Cu system and is effectively removed in combination with acid leaching [71].

Si–Mg ALLOY SYSTEMS

In works [72, 73] magnesium alloying and refining and acid leaching were studied for removing impurities from MG–Si. Phosphorus concentration of 0.2 ppm_w in SOG–Si was obtained after acid leaching. It is shown that a porous structure of the nanometer and micrometer range formed in Si–Mg alloys, and high-purity silicon (~99,995 %) was produced after leaching.

CONCLUSIONS

1. Investigations of MG–Si refining by metallurgical methods show that each method is selective at remov-

al of one or a small group of impurity elements. P or B evaporation is possible, but most often this process is slow, and it can be accompanied by Si loss. Solvent refining proved that Al is a suitable alloying intermediary. The advantages of the metallurgical processing methods can be used at a combination of the methods sequentially or simultaneously, in order to manufacture a product, corresponding to SoG–Si solar-grade silicon.

2. During electron beam remelting of metallurgical silicon purification takes place by evaporation of impurity elements from the melt surface in vacuum. Refining is based on conducting the process in a high vacuum and difference in the vapour pressures of different impurity elements, which will lead to removal from the melt surface of the components, the vapour pressure of which is high than that of the silicon vapours. The method of electron beam remelting of metallurgical silicon together with oxidative refining enables purification to the level of 5–6 N.

3. The impurities in MG–Si are classified as segregation and insoluble. Segregation impurities are readily revealed, while insoluble impurities cannot be detected completely in case of crushing of MG–Si mass.

4. Single-acid leaching removes only certain impurities. Therefore, in practice the sequential or mixed acid leaching is widely used. Adding oxidizers into acidic leaching agents enhances the effectiveness of impurity removal, particularly for H_2O_2, or its combinations with $AgNO_3$ and $Cu(NO_3)_2$.

5. Impurity removal from MG–Si by metallurgical processes depends on the impurity sensitivity to acid etchants. External fields (ultraviolet radiation, ultrasonic field and leaching under oxygen pressure) or introduction of cracks/porous structures and thermal pretreatment can improve impurity removal.

6. Combination of the processes of secondary purification (slag purification and solvent purification) and hydrometallurgical processes is the most effective to remove insoluble impurities from MG–Si. Systems of slag purification are usually combined with HCl or acid mixtures containing HCl. Different metals (Ca, Cu, Al, Sn, Mg) are used as solvents for purification of metallurgical silicon and this requires acid leaching.

REFERENCES

1. Morita, K., Miki, T. (2003) Thermodynamics of solar-grade-silicon refining. *Intermetallics,* 11(**11–12**), 1111–1117. DOI: https://doi.org/10.1016/s0966-9795(03)00148-1
2. Chen, H., Morita, K., Ma, X. et al. (2019) Boron removal for solar-grade silicon production by metallurgical route: A review. *Sol. Energ. Mat. Sol. C*., **203**, 110169. DOI: https://doi.org/10.1016/j.solmat.2019.110169
3. Heuer, M. (2013) Chapter two-metallurgical grade and metallurgically refined silicon for photovoltaics. *Semiconduct. Semimet*, **89**, 77–134. DOI: https://doi.org/10.1016/B978-0-12-381343-5.00002-1
4. Ding, Z., Ma, W., Wei, K. et al. (2012) Boron removal from metallurgical-grade silicon using lithium containing slag. *J. Non-Cryst. Solids*, 358(**18–19**), 2708–2712. DOI: https://doi.org/10.1016/j.jnoncrysol.2012.06.031
5. Chen, H., Wang, Y., Zheng, W. et al. (2017) Model implementation of boron removal using $CaCl_2$–CaO–SiO_2 slag system for solar-grade silicon. *Metall. Mater. Transact. B Process Metall. Mater. Process. Sci*., 48(**6**), 3219–3227.DOI: https://doi.org/10.1007/s11663-017-1105-7
6. Hunt, L.P., Dosaj, V.D., McCormick, J.R., Crossman, L.D. (1976) Production of solar-grade silicon from purified metallurgical silicon. In: *Record of the 12th IEEE Photovoltaic Specialists Conf.*, 125–129.
7. Dietl, J. (1983) Hydrometallurgical purification of metallurgical-grade silicon. *Solar Cells,* 10(**2**), 145–154. DOI: https://doi.org/10.1016/0379-6787(83)90015-7
8. Wei, K., Zheng, D., Ma, W. et al. (2015) Study on Al removal from MG–Si by vacuum refining. *Silicon,* 7(**3**), 269–274. DOI: https://doi.org/10.1007/s12633-014-9228-9
9. Tan, Y., Guo, X., Shi, S. et al. (2013) Study on the removal process of phosphorus from silicon by electron beam melting. *Vacuum,* **93**, 65–70. DOI: https://doi.org/10.1016/J.VACUUM.2012.12.010
10. Qian, G., Sun, L., Chen, H. et al. (2020) Enhancing impurities removal from Si by controlling crystal growth in directional solidification refining with Al–Si alloy. *J. Alloys Compd.,* **820**, 153300. DOI: https://doi.org/10.1016/j.jallcom.2019.153300
11. Lei, Y., Qiu, P., Chen, K. et al. (2019) Mechanism of ZrB_2 formation in Al–Si alloy and application in Si purification. *ACS Sustain. Chem. Eng.,* 7(**15**), 12990–12996. DOI: https://doi.org/10.1021/acssuschemeng.9b02065
12. Ren, Y., Ueda, S., Morita, K. (2019) Formation mechanism of ZrB_2 in a Si–Cu melt and its potential application for refining Si and recycling Si waste. *ACS Sustain. Chem. Eng*., 7(**24**), 20107–20113. DOI: https://doi.org/10.1021/acssuschemeng.9b05986
13. Braga, A.F.B., Moreira, S.P., Zampieri, P.R. et al. (2008) New processes for the production of solar-grade polycrystalline silicon: A review. *Sol. Energ. Mat. Sol. C.,* 92(**4**), 418–424. DOI: https://doi.org/10.1016/j.solmat.2007.10.003
14. Chigondo, F. (2018) From metallurgical-grade to solar-grade silicon: An overview. *Silicon*, 10(**3**), 789–798. DOI: https://doi.org/10.1007/s12633-016-9532-7
15. Xi, F., Li, Sh., Ma, W. et al. (2021) A review of hydrometallurgy techniques for the removal of impurities from metallurgical-grade silicon. *Hydrometallurgy,* **201**, 105553. DOI: https://doi.org/10.1016/j.hydromet.2021.105553
16. Hunt, L.P. (1990) *Silicon precursors: Their manufacture and properties*: Handbook of semiconductor silicon technology. Noyes PUB. https://scholar.google.com.ua/scholar?q=Their+manufacture+and+properties%3B+Handbook+of+semiconductor+silicon+technology%3B+Noyes+PUB.+(1990).&hl=uk&as_sdt=0&as_vis=1&oi=scholart
17. Ohmi, T., Imaoka, T., Sugiyama, I., Kezuka, T. (1992) Metallic impurities segregation at the interface between Si wafer and liquid during wet cleaning. *J. Electrochem. Soc.,* 13(**11**), 3317. DOI: https://doi.org/10.1149/1.2069074
18. Vick, G.L., Whittle, K.M. (1969) Solid solubility and diffusion coefficients of boron in silicon. *J. Electrochem. Soc.,* 116(**8**), 1142. DOI: https://doi.org/10.1149/1.2412239
19. Sun, Y.H., Ye, Q.H., Guo, C.J. et al. (2013) Purification of metallurgical-grade silicon via acid leaching, calcination and

quenching before boron complexation. *Hydrometallurgy*, **139**, 64–72. DOI: https://doi.org/10.1016/j.hydromet.2013.07.002
20. Lai, H., Huang, L., Gan, C. et al. (2016) Enhanced acid leaching of metallurgical grade silicon in hydrofluoric acid containing hydrogen peroxide as oxidizing agent. *Hydrometallurgy*, **164**, 103–110. DOI: https://doi.org/10.1016/j.hydromet.2016.06.003
21. Lai, H., Huang, L., Xiong, H. et al. (2017) Hydrometallurgical purification of metallurgical grade silicon with hydrogen peroxide in hydrofluoric acid. *Ind. Eng. Chem. Res.,* 56(**1**), 311–318. DOI: https://doi.org/10.1021/acs.iecr.6b02245
22. Xi, F., Li, S., Ma, W. et al. (2018) Removal of impurities from metallurgical grade silicon with metal assisted chemical leaching. *Hydrometallurgy*, **178**, 250–255. DOI: https://doi.org/10.1016/j.hydromet.2018.05.013
23. Xi, F., Cui, H., Li, Y. et al. (2019) Novel enhancing impurities purification from silicon powder through metal-catalyzed chemical corrosion. *Powder Technol.,* **352**, 53–61. DOI: https://doi.org/10.1016/j.powtec.2019.04.055
24. Hunt, L.P., Dosaj, V.D., McCormick, J.R., Crossman, L.D. (1976) Production of solar-grade silicon from purified metallurgical silicon. In: *Record of the 12th IEEE Photovoltaic Specialists Conf.,* 125–129. https://ntrs.nasa.gov/citations/19780027016
25. Zong, L., Zhu, B., Lu, Z. et al. (2015) Nanopurification of silicon from 84 % to 99.999 % purity with a simple and scalable process. *P. Natl. Acad. Sci.*, 112(**44**), 13473–13477. DOI: https://doi.org/10.1073/pnas.1513012112
26. Won, C.W., Nersisyan, H.H., Won, H.I. (2011) Solar-grade silicon powder prepared by combining combustion synthesis with hydrometallurgy. *Sol. Energ. Mat. Sol. C*, 95(**2**), 745–750. DOI: https://doi.org/10.1016/j.solmat.2010.10.016
27. Khalifa, M., Hajji, M., Ezzaouia, H. (2012) Purification of silicon powder by the formation of thin porous layer followed byphoto-thermal annealing. *Nanoscale Res. Lett.,* 7(**1**), 1–4. DOI: https://doi.org/10.1186/1556-276x-7-444
28. Khalifa, M., Atyaoui, M., Hajji, M. et al. (2013) Purification of metallurgical-grade silicon powder via chemical attack by hydrofluoric and nitric acids followed by thermal treatment. *Mater. Sci. Semicond. Process*., 16(**6**), 1742–1746. DOI: https://doi.org/10.1016/j.mssp.2013.06.006
29. Khalifa, M., Hajji, M., Ezzaouia, H. (2013) An efficient method combining thermal annealing and acid leaching for impurities removal from silica intended for photovoltaic application. *B. Mater. Sci.*, 36(**6**), 1097–1101. https://www.ias.ac.in/article/fulltext/boms/036/06/1097-1101
30. Xi, F., Cui, H., Zhang, Z. et al. (2019) Novel and efficient purification of silicon through ultrasonic-Cu catalyzed chemical leaching. *Ultrason. Sonochem*., **56**, 474–480. https://www.sciencedirect.com/science/article/pii/S1350417719303918
31. Li, Y., Zhang, L. (2019) Application of Si-based solvents to the purification of metallurgical grade-silicon. *Sep. Purif. Rev.,* 1–24. https://www.researchgate.net/publication/350061593
32. Liang, J.-Sh., Ye, Yu.-R., Wu, H.-T. et al. (2023) Progress of preparing solar-grade silicon by metallurgical silicon slag refining. *Chinese J. of Nonferrous Metals*. DOI: https://doi.org/10.11817/j.ysxb.1004.0609.2021-42471
33. Heuer, M. (2013) Chapter two — Metallurgical grade and metallurgically refined silicon for photovoltaics. *Semiconduct. Semimet*., **89**, 77–134. DOI: http://dx.doi.org/10.1016/B978-0-12-381343-5.00002-1
34. Fang, M., Lu, C.H., Huang, L.Q. et al. (2014) Separation of metal impurities from metallurgical grade silicon via CaO–SiO_2–CaF_2 slag treatment followed by leaching with hydrochloric acid. *Sep. Sci. Technol.,* 49(**14**), 2261–2270. https://www.semanticscholar.org/paper/c86b4c2144a5df185dc0e979c3e6e71b4ffe4c94
35. Fang, M., Lu, C., Huang, L. et al. (2014) Effect of calcium-based slag treatment on hydrometallurgical purification of metallurgical-grade silicon. *Ind. Eng. Chem. Res.,* 53(**2**), 972–979. https://www.researchgate.net/publication/263957572
36. Huang, L., Lai, H., Lu, C. et al. (2016) Evaporation behavior of phosphorus from metallurgical grade silicon via calcium-based slag treatment and hydrochloric acid leaching. *J. Electron. Mater.,* 45(**1**), 541–552. https://link.springer.com/article/10.1007/s11664-015-4146-1
37. Zhou, Q., Wu, J., Ma, W. et al. (2019) Boron removal from industrial silicon by combined slagging and acid leaching treatment technology. *JOM*, 72(**7**), 2670–2675. DOI: https://doi.org/10.1007/s11837-019-03847-4
38. Ghosh, A. (2001) *Secondary steelmaking-principles and applications*. (Chapter 6). CRC Press, Boca Raton, London, New York, Washington, D.C. https://www.taylorfrancis.com/books/mono/10.1201/9781420042313/secondary-steelmaking-ahindra-ghosh
39. Miki, T., Morita, K., Sano, N. (1996) Thermodynamics of phosphorus in molten silicon. *Metall. Mater. Transact.,* **27B**, 937. https://www.infona.pl/resource/bwmeta1.element.springer-6645efe1-974a-3b88-8644-c0399919bb84
40. Pires, J.C.S., Otubo, J., Braga, A.F.B., Mei, P.R. (2005) The purification of metallurgical grade silicon by electron beam melting. *J. Mater. Process. Technol.,* **169**, 21–25. https://www.sciencedirect.com/science/article/pii/S0924013605003675/pdf?md5=02d666a90ee46fda5d97871918fa1e1c&pid=1-s2.0-S0924013605003675-main.pdf
41. Safarian, J., Xakalashe, B., Tangstad, M. (2011) Vacuum removal of the impurities of different silicon melts. In: *26th European Photovoltaic Solar Energy Conf.*, *Hamburg, Germany*. https://www.researchgate.net/publication/267824751
42. Suzuki, K., Sakaguchi, K., Nakagiri, T., Sano, N. (1990) Gaseous removal of phosphorus and boron from molten silicon. *J. Jpn. Inst., Met.*, **54**, 161. https://www.osti.gov/etdeweb/biblio/6822482
43. Yuge, N., Abe, M., Hanazawa, K. et al. (2001) Purification of metallurgical-grade silicon up to solar-grade. *Prog. Photovolt. Res. Appl.,* **9**, 203–209. DOI: http://dx.doi.org/10.1002/pip.372
44. Olette, M. (1961) *Physical chemistry of process metallurgy*. Pt 2, Ed. by G.R. St-Pierre. Interscience, New York, NY,1065. https://www.researchgate.net/publication/267824751
45. Zheng, S.S., Chen, W.H., Cai, J. et al. (2010) Mass transfer of phosphorus in silicon melts under vacuum induction refining. *Met. Mater. Transact.,* **B 41**, 1268. https://core.ac.uk/download/pdf/41347899.pdf
46. Pires, J.C.S., Otubo, J., Braga, A.F.B., Mei, P.R. (2005) The purification of metallurgical grade silicon by electron beam melting. *J. Mater. Process. Technol.,* **169**, 21–25. DOI: https://doi.org/10.1016/j.jmatprotec.2005.03.006
47. Pires, J.C.S., Otubo, J., Braga, A.F.B., Mei, P.R. (2005) The purification of metallurgical grade silicon by electron beam melting. *J. Mater. Process. Technol.* **169**, 16–20. https://www.academia.edu/9442020
48. Suzuki, K., Kumagai, T., Sano, N. (1992) Removal of boron from metallurgical-grade silicon by applying the plasma treatment. *ISIJ Int.,* 32(**5**), 630–634. https://www.academia.edu/109502229/
49. Ikeda, T., Maeda, M. (1961) Elimination of boron in molten silicon by reactive rotating plasma arc melting, *Mater. Transact., JIM*, 37(**5**), 983–987. https://www.jstage.jst.go.jp/article/matertrans1989/37/5/37_5_983/_pdf

50. Gao, Yu., Tan, Yi, Qi, W. (2025) Removal of metal impurities from silicon via chlorination coupled with electron beam induced directional solidification. *Separation and Purification Technology*, **380**, Pt 3, February, 135575. DOI: https://doi.org/10.1016/j.seppur.2025.135575
51. Hoseinpur, A., Tang, K., Ulyashin, A. et al. (2023) Toward the recovery of solar silicon from end-of-life PVs by vacuum refining. *Solar Energy Materials and Solar Cells,* 251:11281. DOI: https://doi.org/10.1016/j.solmat.2023.112181
52. Khattak, C.P., Joyce, D.B., Schmid, F. (1983) Production of solar-grade silicon by refining of liquid metallurgical grade silicon. In: *Proc. of Symp. on Materials and New Processing Technology for Photovoltaics, Proc. Electrochemical Soc.,* 83(**11**), 478. https://www.nrel.gov/docs/fy00osti/27593.pdf
53. Khattak, C.P., Joyce, D.B., Schmid, F. (2001) Production of solar-grade (SoG) silicon by refining liquid metallurgical grade (MG) silicon. *National Renewable Energy Laboratory*. Final Report, August, 1–40. DOI: http://dx.doi.org/10.2172/786367
54. Alemany, C., Trassy, C., Pateyron, B., K.I. Li, Delannoy Y. (2002) Refining of metallurgical-grade silicon by inductive plasma. *Solar Energy Materials and Solar Cells*, 72(**1–4**), 41–48. https://www.sciencedirect.com/science/article/pii/S0927024801001489
55. Flamant, G., Kurtcuoglu, V., Murray, J., Steinfeld, A. (2006) Purificaiton of metallurgical grade silicon by a solar process. *Solar Energy Materials & Solar Cells*, **90**, 2099–2106.
56. Dawless, R.K., Troup, R.L., Meier, D.L., Rohatgi, A. (1988) Production of extreme-purity aluminum and silicon by fractional crystallization processing. *J. Cryst. Growth,* 89(**1**), 68–74. https://www.sciencedirect.com/science/article/pii/0022024888900735
57. Kotval, P.S., Strock, H.B. (1978) *Silicon solar cells with low-cost substrates*. US Pat., **0412441A**.
58. Mallah, A.R., Saevarsdottir, G., Heuer, M., Svavarsson, H.G. (2025) Advancing sustainability in solar-grade silicon production: Enhanced boron and phosphorus removal via silicon refining from Al–Si melt. *JOM*, 77(**4**), 2512–2526. DOI: https://doi.org/10.1007/s11837-024-07114-z
59. Juneja, J.M., Mukherjee, T.K. (1986) A study of the purification of metallurgical grade silicon. *Hydrometallurgy,* 16(**1**), 69–75. DOI: https://doi.org/10.1016/0304-386X(86)90052-6
60. Yoshikawa, T., Arimura, K., Morita, K. (2005) Boron removal by titanium addition in solidification refining of silicon with Si–Al melt. *Metall. Mater. Transact*., **36B**, 837–842. https://link.springer.com/article/10.1007/s11663-005-0085-1
61. Yoshikawa, T., Morita, K. (2003) Removal of phosphorus by the solidification refining with Si–Al melts. *Sci. Technol. Adv. Mater.*, **4**, 531–537. DOI: https://doi.org/10.1016/j.stam.2003.12.007
62. Morita, K., Yoshikawa, T. (2011) Thermodynamic evaluation of new metallurgical refining processes for SOG-silicon production. *Transact. Nonferrous Met. Soc.*, **21**, 685–690.
63. Yoshikawa, T., Morita, K. (2005) In EPD congress. High-temperature refining of metallurgical-grade silicon. *TMS, Warrendale*, 549–558. DOI: https://doi.org/10.1007/s11837-012-0384-3
64. Bathey, B., Cretella, M.C. (1982) Vacuum refining of molten silicon. *J. Mater. Sci.,* **17**, 3077-96. DOI: https://doi.org/10.1007/BF01203469
65. Good, E.A. (2004) *Impurity partitioning effects in silicon crystallization from metal: Eutectic solutions for solar cell applications*: Ph.D. Dissertation, Colorado School of Mines, Golden, CO. https://www.nrel.gov/docs/fy02osti/32706.pdf
66. Zhao, L., Wang, Z., Guo, Z., Li, C. (2011) Low-temperature purification process of metallurgical silicon. *Transact. Nonferrous Met. Soc*., **21**, 1185–1192. DOI: https://doi.org/10.1016/S1003-6326(11)60841-8
67. Mitrasinovic, A.M., Utigard, T.A. (2009) Refining silicon for solar cell application by copper alloying. *Silicon*, 1(**4**), 239–248. DOI: http://dx.doi.org/10.1007/s12633-009-9025-z
68. Huang, L., Lai, H., Lu, C. et al. (2016) Enhancement in extraction of boron and phosphorus from metallurgical grade silicon by copper alloying and aqua regia leaching. *Hydrometallurgy*, **161**, 14–21. DOI: https://doi.org/10.1016/j.hydromet.2016.01.013
69. Huang, L., Danaei, A., Thomas, S. et al. (2018) Solvent extraction of phosphorus from Si–Cu refining system with calcium addition. *Sep. Purif. Technol.,* **204**, 205–212. DOI: https://doi.org/10.1016/j.seppur.2018.04.087
70. Safarian, J., Tranell, G. (2016) Silicon purification through magnesium addition and acid leaching. In: *32 European PV Conf. and Exhibition. European Photovoltaic Solar Energy Conf. and Exhibition,* 1011–1014. http://hdl.handle.net/11250/2467067
71. Espelien, S., Tranell, G., Safarian, J. (2017) Effect of magnesium addition on removal of impurities from silicon by hydrometallurgical treatment. In: *Energy Technol. Springer,* 355–366. DOI: http://dx.doi.org/10.1007/978-3-319-52192-3_35
72. Zhu, M., Azarov, A., Monakhov, E. et al. (2020) Phosphorus separation from metallurgical-grade silicon by magnesium alloying and acid leaching. *Sep. Purif. Technol.,* **240**, 116614. DOI: https://doi.org/10.1016/j.seppur.2020.116614
73. Mei, J., Yu, W., Hou, P. et al. (2021) Purification of metallurgical grade silicon via the Mg–Si alloy refining and acid leaching process. *Silicon,* **13**, 341–350. DOI: https://doi.org/10.1007/s12633-020-00439-9

ORCID

G.G. Didikin: 0000-0002-9268-5072

CORRESPONDING AUTHOR

G.G. Didikin
E.O. Paton Electric Welding Institute of the NASU
11 Kazymyr Malevych Str., 03150, Kyiv, Ukraine.
E-mail: didikin@paton-icebt.kievua

SUGGESTED CITATION

G.G. Didikin (2026) Production and refining of metallurgical silicon to solar-grade silicon (Review). *The Paton Welding J*., **04**, 15–23. DOI: https://doi.org/10.37434/tpwj2026.04.03

JOURNAL HOME PAGE

https://patonpublishinghouse.com/eng/journals/tpwj

Received: 15.12.2025
Received in revised form: 08.02.2026
Accepted: 16.04.2026

DOI: https://doi.org/10.37434/tpwj2026.04.04

COMPUTER PROGRAM FOR MODELLING STRESS-STRAIN STATE OF A CIRCUMFERENTIAL WELDED JOINT

L.M. Lobanov, O.V. Makhnenko, O.S. Milenin, O.A. Velykoivanenko, G.P. Rozynka, N.R. Basystyuk, G.Yu. Saprykina

E.O. Paton Electric Welding Institute of the NASU
11 Kazymyr Malevych Str., 03150, Kyiv, Ukraine

ABSTRACT

The "Girth Weld" computer program enables computational analysis of following phenomena in circumferential welded joints (girth welds) of pipelines and pressure vessels, including: mechanical properties of weld metal and heat-affected zone (HAZ) , residual stresses and deformations, stress-strain state redistribution under post-weld heat treatment, operational loads, or pressure testing, structural integrity assessment and service life prediction for welds with discontinuities (detected by non-destructive testing or postulated). The program requires no specialized skills in computational methods, automating key processes such as parametric modelling of multipass girth welds, finite element mesh generation, solver execution and results visualization. Despite minimal hardware and time requirements, "Girth Weld" ensures high accuracy through advanced modelling of welding physico-chemical processes, efficient algorithms for nonlinear problems and optimized solutions for high-order differential equations.

KEYWORDS: multipass welding, girth weld, computer program, mathematical modelling, finite element method, mechanical properties, residual stresses, deformations, post weld heat treatment, operational loads, defect acceptability

INTRODUCTION

With the development of computing technology, methods for solving thermoplasticity problems and describing characteristic changes in the material of a welded joint during welding heating, computational approaches and mathematical modelling of welding processes are finding widespread application in industry. However, a very challenging issue is the accessibility of such an approach for users with limited access to commercial finite element analysis software packages such as SYSWELD, ABAQUS, ANSYS, MARC etc.

To address this issue, a highly specialized computer program "Girth Weld" was developed as a part of the "Weldprediction" software package for the mathematical modelling of the stress-strain state and mechanical properties in the zone of a girth butt weld during arc welding. It is designed for engineering and scientific applications and does not require the user to have specialized training in computational methods.

The "Girth Weld" computer program is applied for typical cases involving welded pipeline assemblies and equipment components. It enables the computational prediction of the mechanical properties of the weld metal and HAZ, residual technological stresses and strains, determination of the stress-strain state redistribution resulting from post weld heat treatment and the effects of operational and testing loads, and prediction of the serviceability and life of critical welded structures with discontinuities (detected by non-destructive testing or postulated).

The "Girth Weld" computer program was developed at the E.O. Paton Electric Welding Institute of the NAS of Ukraine (PWI). The development of this program was based on many years of experience in the mathematical modelling of physico-chemical processes during welding, surfacing, heat treatment and related technologies, as well as on recent advances in numerical methods, mechanics of deformable bodies and fracture mechanics.

In this context, a specialized computer program provides the following advantages:

- high accuracy of predictive results with limited demands on computing and time resources (short calculation time) due to the use of modern approaches to modelling physico-chemical processes during welding and efficient algorithms for solving nonlinear problems and systems of high-order differential equations;
- reduced effort due to a simple data input interface and the full automation of processes such as mathematical modelling, finite element mesh generation, solver execution and results visualization;
- no need for service personnel, as the program can be operated by a welding-engineer or a process engineer, rather than solely by a specialist in numerical methods for solving mathematical problems.

GENERAL DESCRIPTION AND PURPOSE OF THE COMPUTER PROGRAM

The "Girth Weld" computer program is an independent, problem-oriented software product designed for numerical finite element analysis of technological

and physical-mechanical processes during multipass welding of circumferential joints in pipeline components and pressure vessels. The program is designed to solve typical tasks of expert analysis of the technological strength of critical structures when planning site and/or repair welding and post-weld heat treatment of girth welds, as well as for predicting short-term and long-term static strength during the subsequent operation of the welded structure, taking into account both its post-weld residual state and the entire range of external working loads.

The "Girth Weld" computer program is recommended for use by organizations in the power, transport and aerospace industries during designing, optimization of construction and planning of repair works in critical pipeline components and pressure vessels with girth welds. This programming code is also recommended for use in justifying the serviceability and expert assessment of the safe life of welded structures, taking into account both their predicted state and operating conditions, as well as discontinuities detected during technical diagnostics (cracks, nonmetallic inclusions, localized thinning, gas pores).

The use of the "Girth Weld" computer program enables solving the following tasks:

- calculation of the optimal layout of the beads during multipass welding, depending on the technical conditions of the process and the criteria for welding optimization;
- determining the kinetics of the temperature field during multipass welding of circumferential joints of pipeline components and pressure vessels, taking into account the technological parameters of the welding process, the geometric features of the specific structure, the type and properties of the material depending on its chemical composition and current temperature;
- numerical assessment of the specifics of the penetration zone formation across the thickness of the structural element;
- predicting the current and residual properties, as well as the microstructural phase composition of the weld metal and HAZ, depending on the type of welding and base materials and the thermal conditions during welding;
- predicting of the kinetics of the elastic-plastic strain field during multipass welding of a circumferential butt joint up to the complete cooling of the structural element and subsequent operational mechanical and thermal effects;
- modelling the distribution of mechanical stresses in the structure caused both by welding effects (transient and residual) and by the thermal and mechanical operating conditions of the specific product;
- calculation of residual distortions of the structure resulting from non-uniform welding heating by assessing irreversible shrinkage phenomena in the welded joint region;
- numerical assessment of the kinetics of residual plastic strain accumulation, which is an important characteristic of the susceptibility of the welded structural metal to hot cracking.

The graphical user interface of the "Girth Weld" computer program provides an interactive mode for numerical analysis and allows the following results of numerical experiments to be displayed on screen and saved as files or hard copies:

- optimal calculation schemes for the layout of beads in the groove of a girth weld;
- two-dimensional distributions of calculated values (temperatures, maximum instantaneous temperatures, residual stresses, plastic strains, fusion zone) presented both as diagrams and tables;
- distribution of microstructural phase components and mechanical properties of the structural metal in the weld zone, taking into account the effect of local heating during multipass welding with known heat input parameters;
- risks of cold and hot cracking;
- distortions of the structure after welding, taking into account irreversible welding shrinkage deformations;
- relaxation of residual stresses due to post-weld heat treatment;
- redistribution of residual stresses under loading conditions (temperature and internal pressure);
- assessment of the fatigue resistance of a girth weld under cyclic loading;
- probabilistic assessment of the serviceability of a cylindrical structure in the presence of macroscopic discontinuities in the weld metal.

METHODS FOR THE NUMERICAL AND SOFTWARE IMPLEMENTATION OF THE PROGRAM CALCULATION ALGORITHMS

The development of a mathematical model for simulating welding processes depends on the purpose of the simulation. To predict temperature cycles, volume fractions of microstructural phases, deformations and residual stresses in a multipass welded joint, finite element models of a volumetric heat source and non-isothermal material deformation, associated with the von Mises yield criterion, are typically used [1, 2]. The modelling is based on tracking the kinetics of the formation and development of plastic strains and stresses in the welded product during the heating and cooling of each welding pass of the joint. The transformation microstructures causing volumetric effects and

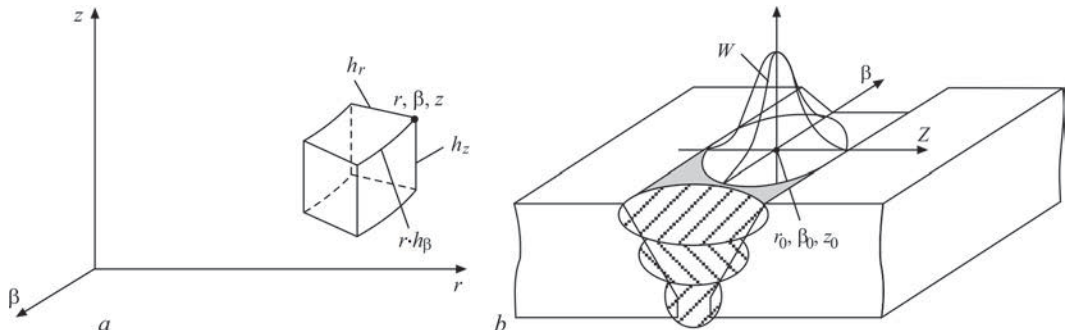

Figure 1. Diagram of a volumetric element in the cylindrical coordinate system (r, β, z) (*a*); distribution of thermal power $W(r, \beta, z, t)$ during multipass welding (*b*)

changes in the physical and mechanical properties of the material in the weld zone are taken into account.

In general terms, during welding in the r, β and z coordinate system (Figure 1, *a*), as the centre of the heat source moves over time $r_0(t)$, $\beta_0(t)$ and $z_0(t)$, the heat release at the point r, β and z at time t is described by the relationship:

$$W(r, \beta, z, t) = W_0(t) \exp [-K_r(r-r_0)^2 - K_\beta(\beta-\beta_0)^2 - K_z(z-z_0)^2], \quad (1)$$

where $W_0(t)$ is the heat flux at the point (r_0, β_0, z_0); K_r, K_β, K_z are the heating concentration coefficients in the r, β, and z directions, respectively. A relationship $K_j = \frac{d_j^2}{4} = 3{,}0$, $d_j = \frac{3.46}{\sqrt{K_j}}$ exists between K_r, K_β, K_z and the corresponding sizes of the effective heating zone d_r, d_β, d_z. $W_0(t)$ can be expressed in terms of the effective heating power $q_{ef}(t)$ by integrating (1) over x, y, z within the heated workpiece. For example, if the source moves along the surface of a solid cylinder along a welded joint (Figure 1, *b*), then:

$$W_0(t) = \frac{2q_{ef}(t)\sqrt{K_x \cdot K_y \cdot K_z}}{\pi\sqrt{\pi}}. \quad (2)$$

By specifying sufficiently accurate values for K_r, K_β and K_z, it is possible to obtain fairly precise results regarding temperatures near the fusion zone of the material being welded, which is important in terms of microstructural phase transformations, mechanical properties, etc.

The mathematical formulation of the problem of heat transfer in a thermally conductive body, in accordance with a given heat source $W(r, z, \beta, t)$ and the corresponding conditions of heat exchange with the surrounding environment at temperature T_c, according to Newton's law:

$$-\lambda\frac{\partial T}{\partial n} = \alpha_T(T - T_c), \quad (3)$$

where λ is the thermal conductivity of the material at temperature T, and α_T is the surface heat transfer coefficient [3].

To the conditions in (3), the initial condition at $t = 0$ and the heat conduction differential equation must be added, which in the (r, β, z) coordinate system takes the form:

$$\frac{\partial}{\partial r}\left(r\lambda\frac{\partial T}{\partial r}\right) + \frac{\partial}{r\partial\beta}\left(\lambda\frac{\partial T}{\partial y}\right) + \frac{\partial}{\partial z}\left(r\lambda\frac{\partial T}{\partial z}\right) + W(r,\beta,z,t) = c\gamma\frac{\partial T}{\partial t}r; \quad (4)$$

$$T(r,\beta,z,t=0) = T_0, \quad (5)$$

where $c\gamma$ is the volumetric heat capacity of the material at temperature T.

Volumetric effects caused by changes in the temperature field are conventionally divided into thermal effects and effects caused by microstructural transformations [5]. Temperature-induced volumetric effects at any point in a welded joint:

$$\varphi = \alpha(T)(T - T_0), \quad (6)$$

where φ is the temperature expansion function, and $\alpha(T)$ is the average value of the coefficient of relative thermal expansion over the temperature range $(T_0 - T)$.

During welding steels prone to hardening, the microstructural composition at any point in the fusion zone and HAZ is determined at time t by the values of the relative content of the j-th phase, $V_j(t)$, where $j = a$ corresponds to austenite, $j = m$ to martensite, $j = f$ corresponds to ferrite, $j = b$ to bainite, and $j = fp$ to a ferrite-pearlite mixture. In this case, $\sum_j V_j(t) \equiv 1$. Volumetric effects at any point due to microstructural transformations in the temperature range $(T_0 - T)$:

$$3\varphi = \frac{\sum V_j(T,t)\gamma_j(T) - \sum V_j(T_0)\gamma_j(T_0)}{\sum V_j(T_0)\gamma_j(T_0)}, \quad (7)$$

where $\gamma_j(T)$ is the volume per unit mass of the j-th phase at temperature T. According to [3], for structural steels, cm^3/g:

$$\gamma_m(T) = 0.12282 + 8.56\cdot 10^{-6}T + 2.15\cdot 10^{-3}C;$$
$$\gamma_a(T) = 0.12708 + 4.448\cdot 10^{-6}T + 2.79\cdot 10^{-3}C; \quad (8)$$
$$\gamma_{b,fp}(T) = 0.12708 + 5.528\cdot 10^{-6}T.$$

The yield strength of a finite element (volume) material at temperature T, taking into account microstructural transformations, is calculated as:

$$\sigma_Y(T) = \sum \sigma_Y^j(T)V_j(T), \quad (j = a, f, fp, b, m);$$
$$\sigma_Y^j(T) = \sigma_Y^j(20)f_j(T), \quad (9)$$

where $\sigma_Y^j(T)$ is the yield strength of the corresponding j-th microstructural phase at temperature T, and C is the carbon content (% by weight).

High temperatures during welding heating and significant non-uniformity in the distribution of the function $\varphi(r, \beta, z, t)$ lead to the occurrence of both elastic and inelastic deformations. The general strain tensor $\varepsilon_{ij}(r, \beta, z, t)$ is typically represented as the sum of three tensors:

$$\varepsilon_{ij} = \varepsilon_{ij}^e + \varepsilon_{ij}^p + \varepsilon_{ij}^c, , \quad (10)$$

where the index ε denotes elastic strain; p denotes instantaneous plastic strain; and c denotes strain due to diffusion-induced plasticity or creep.

Plastic strains are related to the stress state by the equation of the theory of plastic non-isothermal flow and the associated Mises yield criterion:

$$d\varepsilon_{ij}^p = d\lambda(\sigma_{ij} - \delta_{ij}\sigma), \quad i, j = x, y, z, \quad (11)$$

where $d\varepsilon_{ij}^p$ is the increment of the tensor ε_{ij}^p, which at a given time t is determined by the deformation history, the stresses σ_{ij} and the temperature T; $d\lambda$ is a scalar function determined by the flow conditions:

$$d\lambda = 0 \text{ if } f = \sigma_{eq}^2 - \sigma_Y^2(T) < 0 \text{ or } f = 0 \text{ when } df < 0;$$
$$d\lambda > 0, \text{ if } f = 0 \text{ and } df > 0;$$
$$\text{the condition } f > 0 \text{ is not admissible;}$$

σ_{eq} is the equivalent stress; $\sigma_Y(T)$ is the yield strength of the material at temperature T.

For creep strain $d\varepsilon_{ij}^c$, the following constitutive equation is used:

$$d\varepsilon_{ij}^c = \Omega(\sigma_{eq}, T)(\sigma_{ij} - \delta_{ij}\sigma)dt, \quad (12)$$

where $\Omega(\sigma_{eq}, T)$ is a scalar creep function of the material at temperature T and a stress level determined by the equivalent stress σ_{eq}.

For this problem, where it is most important to account for creep deformations $d\varepsilon_{ij}^c$ during heat treatment, as the stress relaxation process depends significantly on them, it is reasonable to select the function $\Omega(\sigma_{eq}, T)$ on the basis of experiments involving the deformation of specimens of this material at elevated temperatures.

Accordingly, the creep function in general form, as a function of material temperature starting from 550 °C and above, can be approximated by a typical relationship:

$$\Omega(\sigma_{eq}, T) = A\cdot\sigma_{eq}^n\cdot\exp\left(\frac{G}{T+273}\right), \quad (13)$$

where A, G and n are the constants related to the properties of the material.

The presented model of creep at elevated temperatures is quite general and allows tracking deformation processes during heat treatment not only during holding, but also during heating and cooling at temperatures, for example, for steels, of 550 °C and above. This model can be effective in simulating the relaxation of residual stresses during local heat treatment of welded structures or in the case of furnace heat treatment with a short holding time, when uniform heating to the specified holding temperature cannot be ensured throughout the volume of the welded structure or assembly.

The increment in the strain tensor $\Delta\varepsilon_{ij}$ over the time interval from $(t - \Delta_t)$ to t, where Δ_t is the time step, which is sufficiently small:

$$\Delta\varepsilon_{ij} = \psi\left(\sigma_{ij} - \delta_{ij}\sigma\right) + \delta_{ij}\left(K\sigma + \varphi\right) - b_{ij}, \left(i, j = x, y, z\right);$$
$$\psi = \frac{1}{2G} + \Delta\lambda + \Delta t\Omega\left(T, \sigma_{eq}\right);$$
$$b_{ij} = \left[\frac{\sigma_{ij} - \delta_{ij}\sigma}{2G} + \delta_{ij}\left(K\sigma\right)\right]_{t-\Delta y} - \delta_{ij}\Delta\varphi, \quad (14)$$

where σ_{ij} is the stress tensor; σ is the mean pressure; δ_{ij} is the unit tensor; the bulk modulus is $K = \frac{1-2\nu}{E}$; the shear modulus is $G = \frac{E}{2(1+\nu)}$; E is the Young's modulus; ν is the Poisson's ratio; $\Delta\lambda$ is the scalar function; $\Omega(T, \sigma_{eq})$ is the creep function.

Constitutive equation (14) contains the function ψ, which is determined by the flow plasticity condition (11) and the creep deformation development (12). This function depends significantly on the initial solution for time t, and its determination requires specific approaches. The simplest approaches are based on using the solution for the time step $(t - \Delta_t)$. By reducing

the time step Δ_t, errors associated with the risk of obtaining unacceptable states can be noticeably reduced (11). However, in the case of welding heating, this risk is very significant and, therefore, approaches based on the construction of appropriate iterative processes for resolving the physical nonlinearity associated with $\Delta\lambda$ and $\Omega(T, \sigma_{eq})$ are more common.

The following iterative process has proven effective in practice:

$$\psi^{(n+1)} = \left[\frac{1}{2G} + \Delta t \Omega\left(T, \sigma_{eq}^{(n-1)}\right)\right](1-p) + p\psi^{(n)},$$
$$\text{if} \quad \sigma_{eq}^{(n)} - \sigma_s\left(T, \sigma_{eq}^{(n)}\right) < -m;$$
$$\psi^{(n+1)} = \psi^{(n)}, \text{if} \quad -m < \sigma_i^{(n)} - \sigma_s\left(T, \sigma_{eq}^{(n)}\right) < m; \qquad (15)$$
$$\psi^{(n+1)} = \psi^{(n)} \cdot \frac{\sigma_{eq}^{(n)}}{\sigma_s\left(T, \sigma_{eq}^{(n)}\right)}, \text{ if } \sigma_{eq}^{(n)} - \sigma_s\left(T, \sigma_{eq}^{(n)}\right) > m.$$

Process (15) ends if:

$$\left|\psi^{(n+1)} \Big/ \psi^{(n)} - 1\right| < \delta, \qquad (16)$$

where n, $n + 1$ are the iteration numbers; $0 \le p < 1$, $m << \sigma_s\left(T, \sigma_{eq}^{(n)}\right)$; $\delta \le 1$ are the parameters of the iterative process.

Following the linearization procedure, the structure of the constitutive equation (14) formally corresponds to the continuity equation of elasticity theory with variable elastic parameters (ψ instead of $1/2G$), and additional deformations b_{ij}, the values of which are known from the solution at the previous time step $(t - \Delta_t)$ and the temperature field at times t and $(t - \Delta_t)$.

Since, in most typical cases of welding and operation of pipeline components and pressure vessels, the distribution of stress and strain fields is characterized by negligible variation in the circumferential direction (along the weld line), in order to reduce the time required for numerical analysis and the demands on computational power, the numerical schemes in the programming code are implemented in a two-dimensional axisymmetric formulation.

This computer program is equipped with a database of the physical and mechanical properties of typical steels and aluminium alloys used in the manufacture of pipeline components and pressure vessels, which simplifies the calculation procedure and reduces the error in numerical analysis results caused by the incompleteness of the reference information available to the user. Similarly, the treatment geometry of a butt weld can be determined either from a set of available preset options used for critical structural components, or entered by the user if the necessary information regarding a specific design solution is available.

USER INTERFACE

The software user interface is designed for welding engineers without special knowledge of mathematical methods. All tasks involved in developing a finite element model of a girth multipass weld in a cylindrical structure are fully automated. All calculation results can be presented in both graphical and tabular form. The information can be copied from any window to a graphics file, the clipboard or a printer. To save all input data and calculation results, there is a function for saving a variant. Available interface languages:

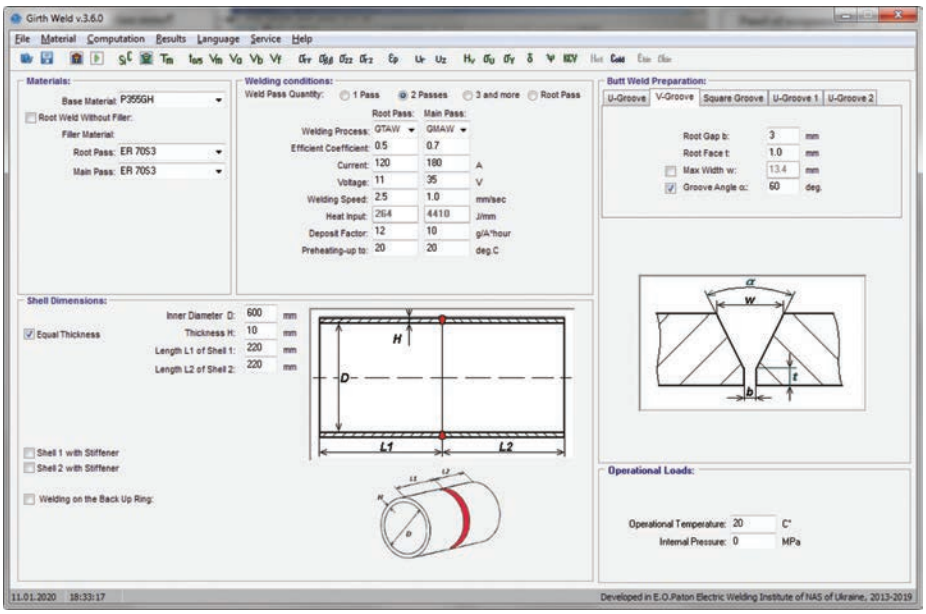

Figure 2. Main window of the "Girth Weld: computer program

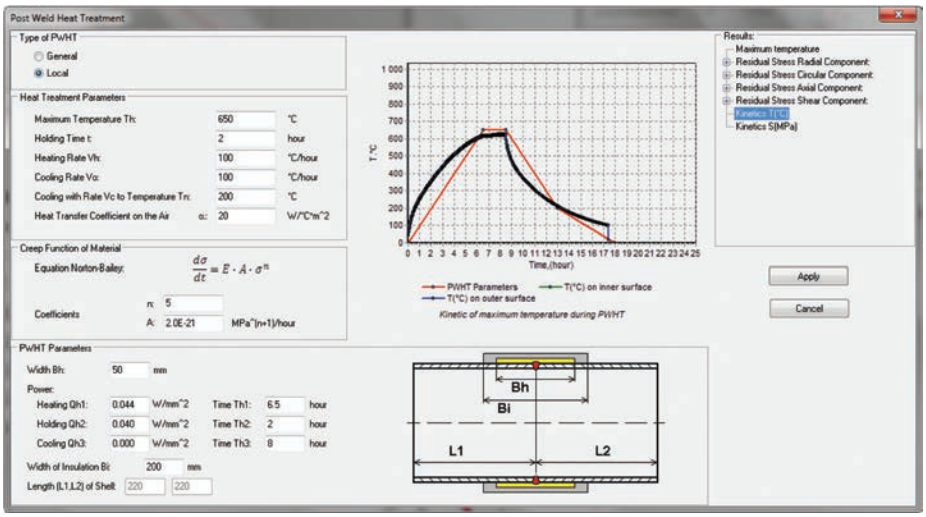

Figure 3. Window for modelling post-weld heat treatment

English, Russian. Figures 2–4 show the windows of the computer program. The main window (Figure 2) is used to enter the sizes of the cylindrical structure and the girth weld, the base material and the welding material, the welding modes and the service load. It also shows the windows for modelling post-weld heat treatment (Figure 3) and the module for probabilistic assessment of the acceptability of a crack-like defect in the area of the girth weld (Figure 4).

MAIN LIMITATIONS OF THE COMPUTER PROGRAM:

● metallic materials: steels, light alloys, titanium and nickel alloys;

● sizes of the cylindrical structure:

● diameter D = 2–10000 mm,

● shell thickness H = 1–20 mm, $H < D/2$,

● length $2L$ = 30–2000 mm, L > 30H;

● edge preparation of the weld girth is single-sided (on the outer side);

● the number of welding passes in a girth weld shall not exceed 200;

● the structural material is treated as a macroscopically continuous, isotropic, elastic-plastic medium capable of strain hardening;

● maximum welding temperatures do not exceed the boiling point of the structural metal;

● the structures are not subject to cryogenic temperatures during operation;

● operational loads: internal pressure from 0 to $P < (0.5\sigma_T 2H/D)$; for example, if H = 5 mm, D = 400 mm, σ_T = 170 MPa, then $P < 2.125$ MPa;

● the acceptability of defects is determined by the conditions of static or quasi-static strength, while the application of assessment methods falls within the scope of specific criteria used in accordance with the relevant standard documents;

● cracks: semi-elliptical in the axial and circumferential directions, on the outer and inner surfaces; crack sizes: depth $a_0 < H$, length $2c_0$, $a/c < 0.7$; fatigue crack propagation;

● pores: diameter d_0 < 1.0 mm, depth r_0: $d_0/2 < r_0 < H - d_0/2$;

● shell thinning: on the outer and inner surfaces; sizes of thinning: depth a_0: $a_0 < H/2$, length $2s_0$: $2s_0 < L/2$; growth of corrosion thinning.

AN ERROR THAT FALLS WITHIN THE ADMISSIBLE RANGE OF NUMERICAL ANALYSIS PARAMETERS

The adequacy of the developed models and their software implementation is ensured and confirmed both by the validation and verification procedures, and by the experience of successfully implementing and utilizing individual procedures and the software as

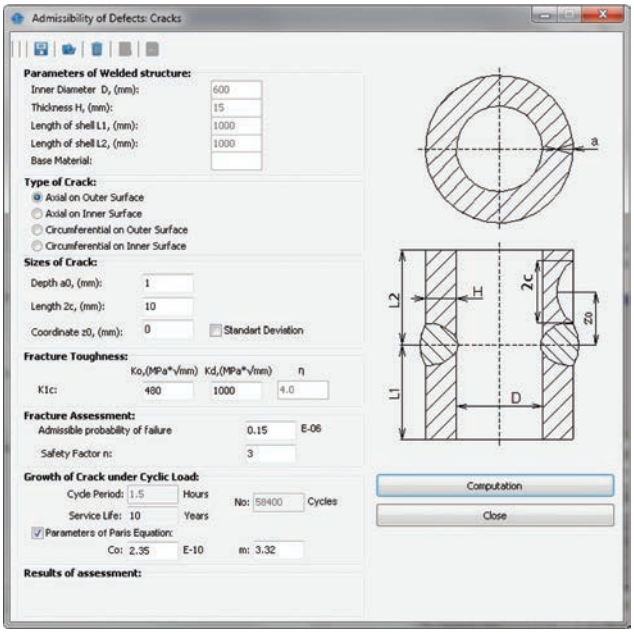

Figure 4. Module window for probabilistic assessment of the acceptability of a crack-like defect in the zone of a girth weld

a whole in optimizing industrial welding cycles for girth welds in critical structures, as well as confirming their serviceability and life by domestic and foreign enterprises in the power, machine-building, transport and aerospace industries.

A comparison of the results obtained using the "Girth Weld" computer program (version 3.6) with full-scale experimental measurements shows that the error in the numerical analysis does not exceed 10–15 %.

VERIFICATION OF THE SIMULATION RESULTS FOR WELDING A DISSIMILAR GIRTH WELD ON A PIPELINE

Residual stresses are important for addressing problems of cracking and failure in welded structures and can be modelled for the welding process. The development of new heat-resistant steels for the power engineering, where girth welded pipes are frequently used, requires an investigation into the impact of welding processes and residual stresses on the safe and reliable operation of power stations.

Finite element modelling of the multipass SMAW (shielded metal arc welding) process was carried out for a butt weld between a pipe with an outer diameter of 42 mm and a shell thickness of 7 mm made of 12 % Cr steel and dissimilar materials (austenitic or pearlitic steel). Such welded joints are used for pipes in boiler steam superheaters at thermal power plants.

The aim of mathematical modelling is to predict temperature fields and the kinetics of the stress-strain state during multipass welding, taking into account the martensitic class of the steel, the choice of welding consumables, welding conditions, preheating temperature, as well as determining the residual stress state after welding and possible post-weld heat treatment.

After preliminary experiments on practicing the welding technology, a more suitable set of welding parameters was selected. The groove was filled by four welding passes (Figure 5). For a dissimilar welded joint (12 % Cr steel + austenitic steel 0.12C–Cr18Ni10T), E-0.11C-Cr16Ni25Mo6Mn2N electrodes with a diameter of 3.0 mm were selected. Welding parameters: 1st pass I = 75–85 A, U = 24 V, $V \approx$ 1.8 mm/s; 2nd–4th passes I = 85–90 A, U = 24 V, $V \approx$ 2.6 mm/s.

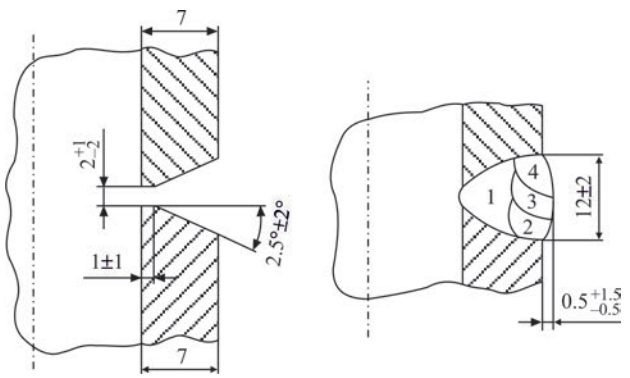

Figure 5. Preparation of single U-type groove for pipe welded joints (SMAW welding process) (*a*), predicted weld configuration and layout of weld beads (*b*)

The chemical composition, mechanical and thermal properties of the base materials and filler metal are presented in Tables 1 and 2.

Taking into account the martensitic class of high-chromium (12 %) steel, the following conditions for the phase transformation of the HAZ microstructure are adopted:

$$\text{if } T > A_c, \text{ then } V_a = 1{,}0\ ,\ V_m = 0;$$

$$\text{if } T < A_c \text{ and } \left(\frac{\partial T}{\partial t} < 0\right), \text{ then } V_j = V_j(T, t), j = a, m;$$

$$V_m(T) = 1 - \exp\left(3\frac{T_s^{(m)} - T}{T_s^{(m)} - T_e^{(m)}}\right); \qquad (17)$$

$$V_a(T) = 1 - V_m(T), \quad \sum_j V_j(t) \equiv 1,$$

where $j = a$ corresponds to austenite; $j = m$ to martensite, and $V_j(T, t)$ is determined from the thermokinetic diagram of austenite decomposition for steel with the corresponding chemical composition. An example of such a diagram is shown in Figure 6 for steel X10CrMoVNb91 [4].

A comparison of the results of numerical calculations using 2D and 3D models for four-pass butt welding of pipes made of dissimilar materials (12 % Cr steel + austenitic steel 0.12C–Cr18Ni10T) shows satisfactory agreement.

The results for the 2D and 3D models shown in Figure 9 reveal fairly similar distributions of maximum temperatures during welding all four passes. In the diagrams, the red colour corresponds to the shape of the molten zone; the size of the HAZ is limited by the 800–850 °C isotherm and reaches approximately 1.5–2.5 mm; the penetration depth of the weld metal into the base material is approximately 1 mm. The molten zones, the penetration depth of the weld and the temperature range in the HAZ are consistent with general thermal expectations.

Figure 10 shows the calculated distributions of residual welding stresses (circumferential component). In the melt zone, where the filler material has an austenitic microstructure, high tensile stresses of up to 450 MPa arise. Adjacent to the melt zone in the HAZ of the 12 % Cr steel base material (lower part of the pipe in Figure 10), martensitic transformation gives rise to localized high compressive stresses of up to –350 MPa, as well as localized tensile stresses of up to 180–300 MPa according to 2D analysis and up to

Table 1. Mechanical and thermophysical properties of materials in a dissimilar welded joint

T, °C	*E*, MPa	α, 10^{-6} 1/K	λ, J/(cm·s·°C)	*c*, J/(cm^3·°C)
Martensitic steel, 12 % Cr				
20	215404	12.1	0.18	3.53
100	211697	12.1	0.19	3.75
200	205591	12.4	0.20	4.02
300	197750	12.8	0.22	4.32
400	188169	13.1	0.23	4.68
500	177028	13.5	0.24	5.15
600	164580	13.9	0.25	6.09
700	154030	13.0	0.27	6.00
800	131900	12.1	0.29	5.20
900	120604	11.1	0.31	4.64
1000	111687	12.5	0.32	4.75
1100	102607	13.6	0.33	4.90
1400	34172	17.5	0.36	9.50
1500	0	24.1	0.35	5.64
Austenitic steel 0.12C–Cr18Ni10T				
20	196531	19	0.146	3.54
100	191369	19	0.156	3.70
200	184280	19	0.168	3.86
300	176922	20	0.180	3.99
400	169296	20	0.193	4.11
500	161416	20	0.205	4.24
600	153303	20	0.218	8.32
700	141463	21	0.236	4.73
800	133320	21	0.249	4.56
900	125217	21	0.262	4.77
1000	116988	22	0.275	4.80
1100	108545	22	0.288	4.96
1200	99881	22	0.301	5.13
1300	88793	23	0.316	5.87
1400	2102	26	0.319	27.00
1500	0	30	0.319	5.64
Welding material E–0.11C–Cr16Ni25Mo6Mn2N (austenitic)				
20	203437	18	0.119	3.58
100	198385	18	0.130	3.73
200	191493	18	0.145	3.87
300	184422	18	0.160	3.99
400	177172	19	0.175	4.10
500	169742	19	0.190	4.21
600	162130	19	0.205	4.41
700	153178	19	0.220	4.57
800	144799	20	0.235	4.84
900	135985	20	0.249	5.05
1000	126625	21	0.263	5.32
1100	117816	21	0.277	4.88
1200	109326	21	0.292	4.99
1300	100669	21	0.307	5.10
1400	74695	22	0.320	11.56
1500	0	28	0.319	5.74

Table 2. Welding parameters for filling the groove of a butt weld using wire of 0.9 mm diameter

Groove filling sequence	Welding parameters					
	I, A pulse/pause	U_a, V	V_w, mm/min	Wire feed rate, V_f, mm/min, pulse/pause	Time, μs pulse/pause	Argon flow rate, l/min
First root pass (1	150/120	9.5	80	880/360	100/100	20–25
Smoothing layer (2)	160/90	10	86	–	100/100	
Third root pass (3)	220/130	11.5	91	2000/1000	225/275	
Fourth root pass (4)	250/150	11.5	89	2600/1300	225/275	
Intermediate filling layer (5–8)	300/180	11.5	89	3400/1620	225/275	
Main filling layer (9–104)	340/200	12	110	3200/1620	225/275	
Weld reinforcement layer (105–112)	260/110	11.5	80.3	1520/1000	175/325	

50 MPa according to 3D analysis, which counterbalance the compressive stresses. The width of the zone of residual tensile hoop stresses in the pipe is quite small (approximately 2 mm). Further out on the periphery of the 12 % Cr steel pipe, compressive stresses of up to –640 MPa occur on the inner surface and tensile stresses of up to 180 MPa on the outer surface. Figure 11 shows the residual hoop stresses across the thickness of the welded joint in the 2D model and in various cross-sections along the angular coordinate from the start–end of welding in the 3D model (0, 90, 180, 270°). One stress curve differs significantly from the other due to the effect of the start and end of welding in the 3D model. The hoop stresses determined by the two-dimensional model are close to the results of the three-dimensional model.

The results of the distribution of residual welding stresses for the axial component shown in Figures 12 and 13, based on 2D and 3D models, also agree well. The martensitic structure of 12 % Cr steel causes the conventional axial tensile residual stresses on the inner surface to change to compressive stresses of up to –400 MPa and, correspondingly, the compressive stresses on the outer surface to tensile stresses of up to 400 MPa. This effect may be beneficial for pipes exposed to a corrosive environment on the inside.

Despite a slight difference in the distribution of residual stresses determined by the 3D model across different cross-sections of the pipe along the angular

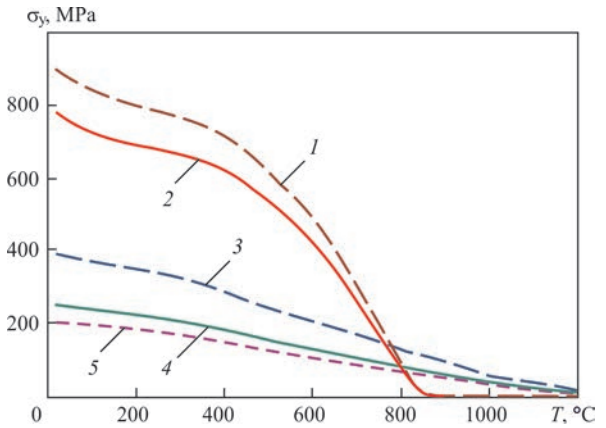

Figure 7. Dependence of the yield strength on temperature and microstructural state: *1* — V_m = 1.0 martensite Thermanit MTS616; *2* — V_m = 1.0 martensite of 12 % Cr steel; *3* — V_a = 1.0 austenite of 12 % Cr steel; *4* — austenitic filler metal E–0.11C–Cr16Ni25Mo6Mn2N; *5* — austenitic base material 0.12C–Cr18Ni10T

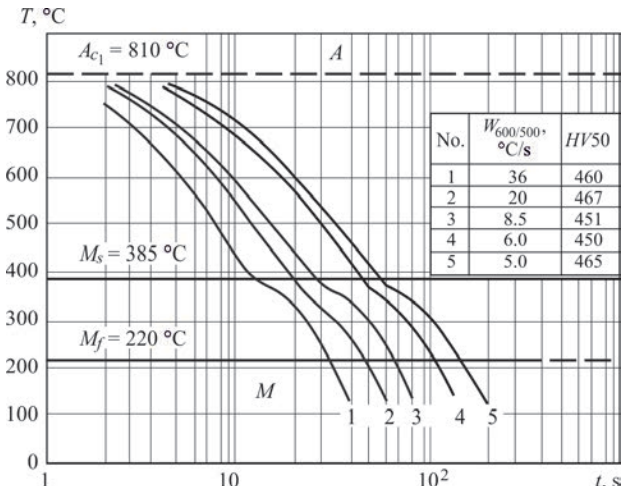

Figure 6. Thermokinetic diagram of austenite decomposition for X10CrMoVNb91 steel [4]

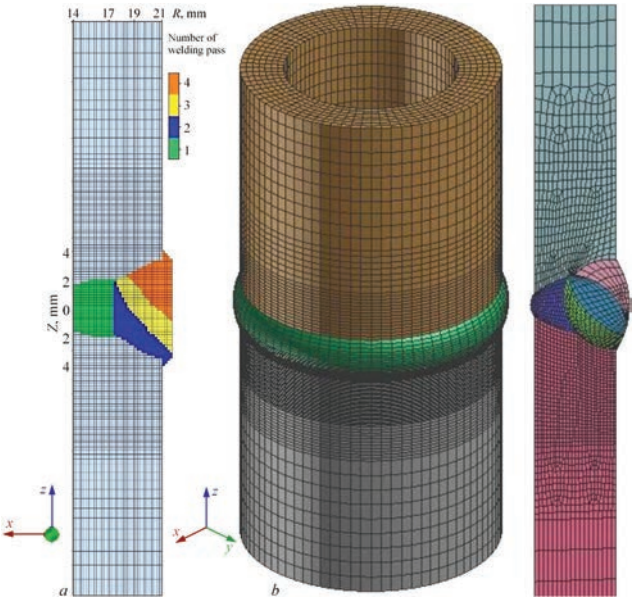

Figure 8. Finite element mesh of the 2D (*a*) and 3D (*b*) models of a girth butt pipe weld

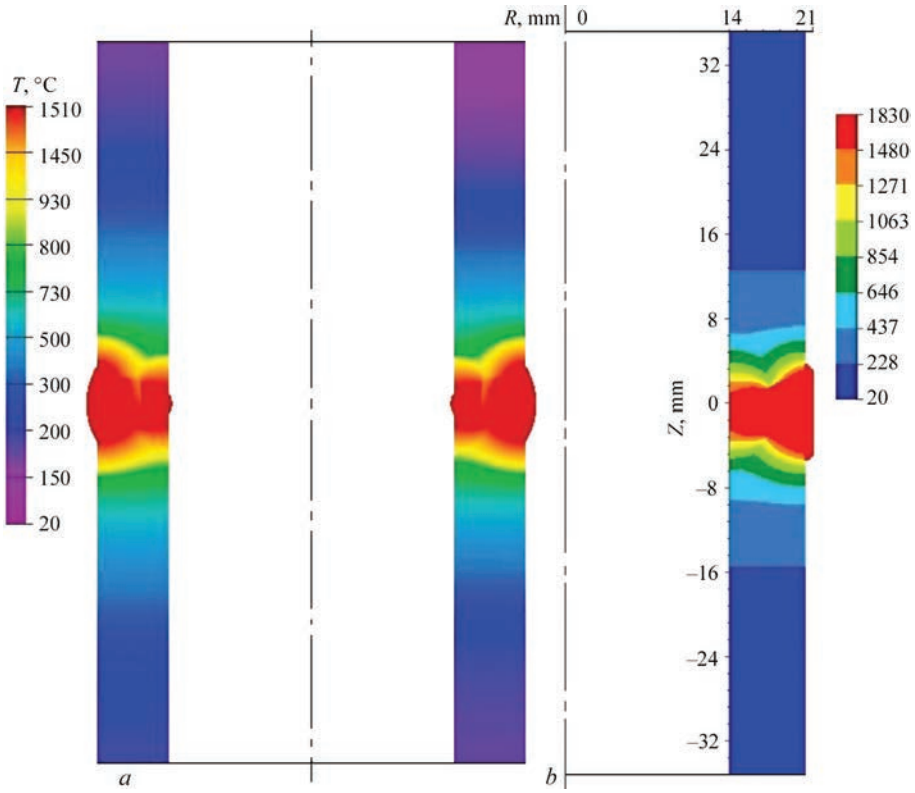

Figure 9. Comparison of calculated distributions of maximum temperature and melting zones (red) in the cross-section of a girth pipe weld: *a* — 3D model; *b* — 2D "Girth Weld" model

coordinate, good agreement with the 2D model was observed. Thus, the 2D model of a girth weld can be used to simulate the distributions of maximum temperatures, microstructural phase composition, mechanical properties, residual stresses and strains during multipass welding of butt joints in pipelines and cylindrical shells (vessels).

VALIDATION OF THE SIMULATION RESULTS FOR MULTIPASS WELDING OF A GIRTH JOINT ON A PIPELINE

Calculations using the "Girth Weld" computer program provided comprehensive information on the distribution of welding stresses throughout the entire volume of the welded joint in the DN850

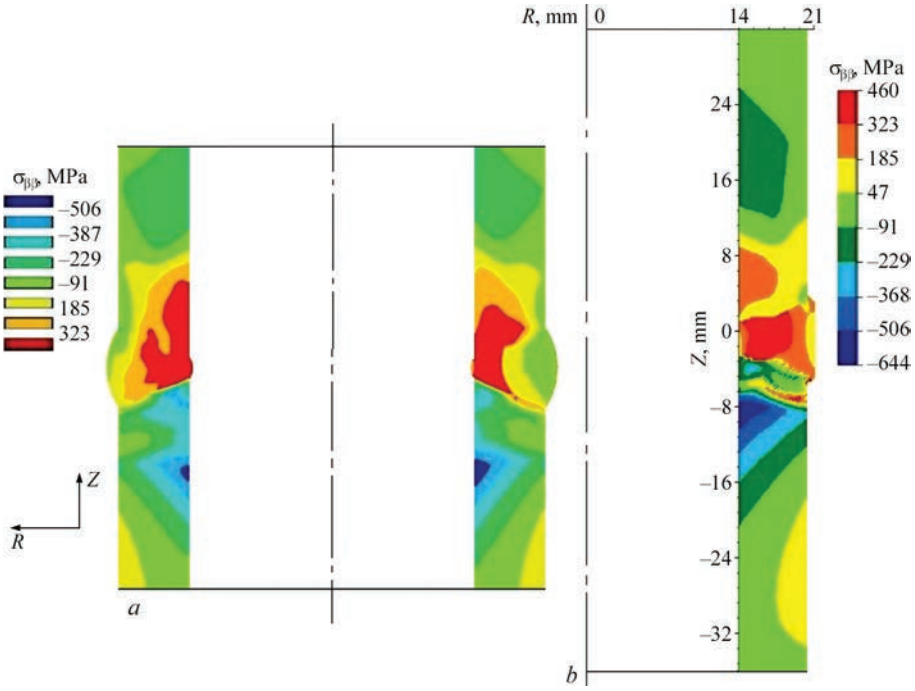

Figure 10. Comparison of numerically calculated distributions of residual welding stresses (circumferential component): *a* — 3D model; *b* — 2D "Girth Weld" model

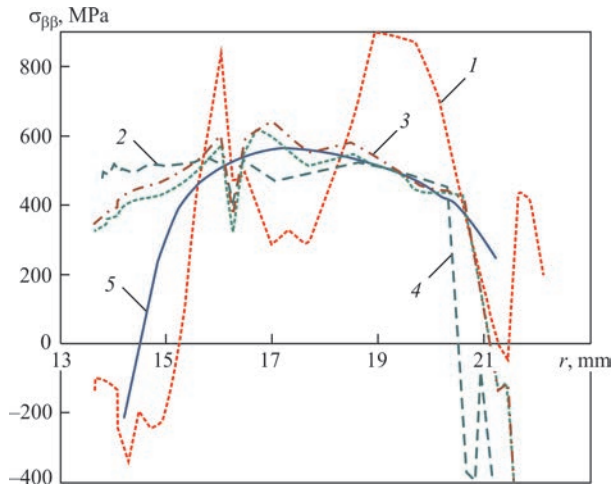

Figure 11. Residual hoop stresses across the thickness of the welded joint in the 2D model and in various cross-sections along the angular coordinate from the start–end of the welding in the 3D model (*1* — 0°; *2* — 90°; *3* — 180°; *4* — 270°)

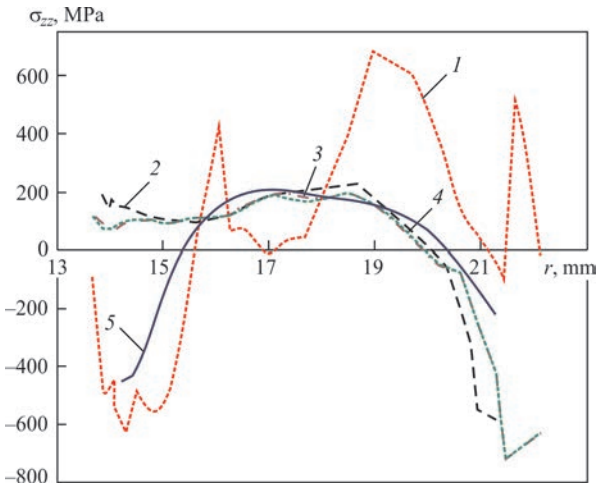

Figure 13. Residual axial stresses across the thickness of the welded joint in the 2D model and in various cross-sections along the angular coordinate from the start–end of the welding in the 3D model (*1* — 0°; *2* — 90°; *3* — 180°; *4* — 270°)

main circulation pipeline for WWER-1000 reactors. To validate the calculation results, data from experimental measurements were used; these were carried out on a mock-up specimen of the welded joint of DN850 main circulation pipeline (MCP) elements on accessible surfaces of the welded elements following heat treatment under a high-temperature tempering mode, for the purpose of comparison with the calculated data.

The calculation procedure is based on the sequential tracking of the development of temperature fields, stresses and strains during the sequential filling of the weld groove with individual beads (Figure 14). For each pass, based on experimental data regarding the parameters of the arc welding process using a nonconsumable electrode in an argon atmosphere, the sizes of the penetration zone and HAZ of the base material (10GN2MFA steel) were determined. The chemical composition of the penetration zones of each bead was determined based on the sizes of the penetration zone and the chemical composition of the filler metal (Sv-08G1NMA wire).

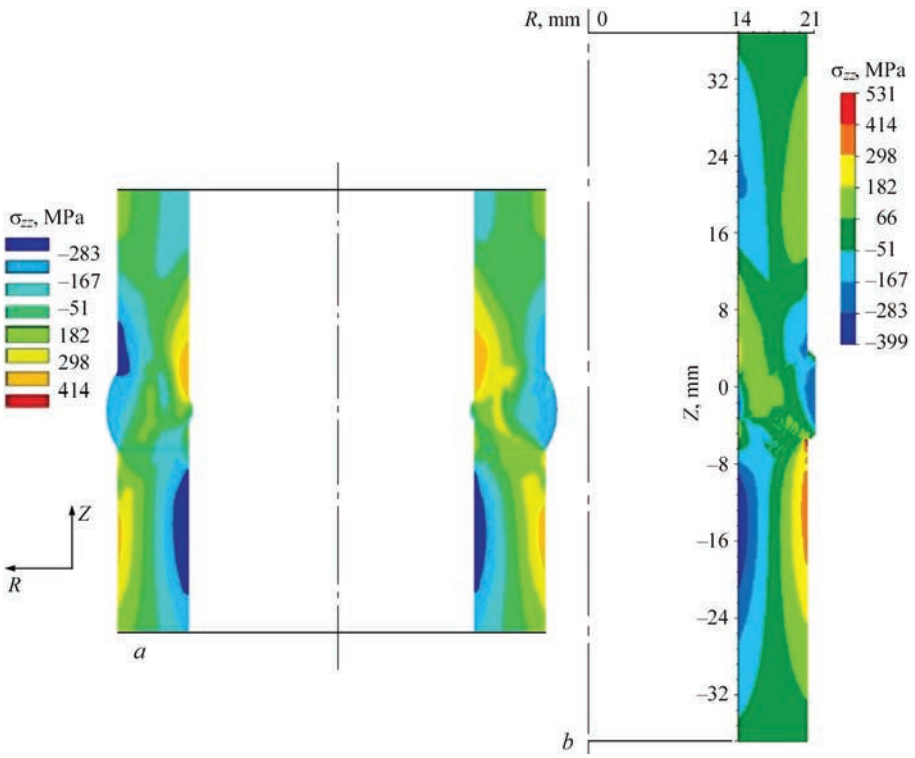

Figure 12. Comparison of numerically calculated distributions of residual welding stresses (axial component): *a* — 3D model; *b* — 2D "Girth Weld" model

Table 3. Mechanical and thermophysical properties of 10GN2MFA steel as a function of temperature [1]

T, °C	$E\cdot10^{-5}$, MPa	$\sigma_y(T)$, MPa	λ, J/(cm·s·°C)	$c\gamma$, J/(cm^3·°C)	ν	α, 1/°C
100	2.01	488	0.375	3.88	0.25	1.14
200	1.96	466	0.370	3.98	0.25	1.18
300	1.90	443	0.360	4.21	0.25	1.22
350	1.87	415	0.355	4.44	0.25	1.25
400	1.85	380	0.350	4.76	0.25	1.30
500	1.78	355	0.337	5.10	0.25	1.34
600	1.70	300	0.320	5.80	0.25	1.39
700	1.60	200	0.305	7.35	0.25	1.42
800	1.50	60	0.285	8.10	0.25	1.47
900	1.35	40	0.280	5.60	0.25	1.52
1000	1.15	20	0.275	5.00	0.25	1.65
1100	1.00	20	0.270	4.90	0.25	1.70
1200	1.00	20	0.267	4.90	0.25	1.62

To model microstructural phase transformations in the HAZ of low-alloy steels during welding or surfacing, an approach was employed based on the use of parametric (regression) equations derived at the PWI [5].

Based on the kinetics of microstructural transformations in the weld metal and HAZ, the volumetric effects were determined at specific times t at temperature T. For 10GN2MFAA steel, equation (8) was used to determine γ_j dependence.

The value of the yield strength$\sigma_T(T)$ of the finite element (volume) material at temperature T, taking into account microstructural transformations, was determined in accordance with equation (9). The creep function coefficients for the base material of the welded joint (10GN2MFA steel) were determined in [1] based on the analysis of experimental data: n = 5, $A = 8.46\cdot10^{17}$ MPa$^{-(n+1)}\cdot h^{-1}$, G = –66394 °C.

Figure 15 shows the calculated data on the distribution of residual stresses, as well as the circumferential and axial components, in the welded girth joint of the DN850 MCP after welding and heat treatment under a high-temperature tempering mode.

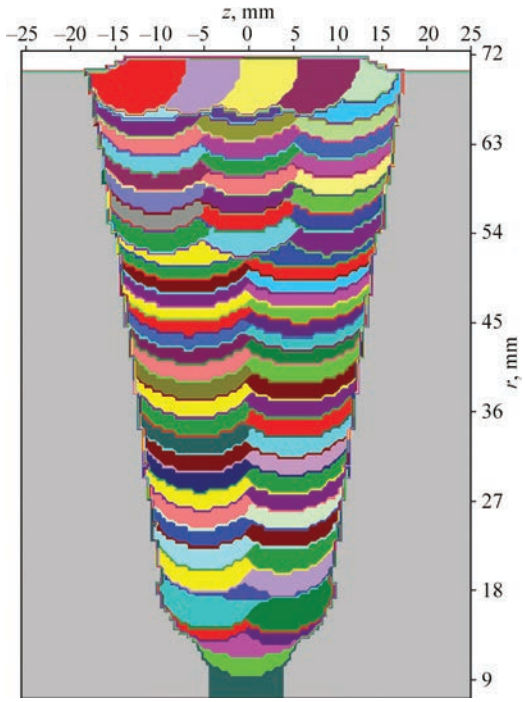

Figure 14. Results of computational modelling of filling the groove for the butt weld of DN850 MCP components

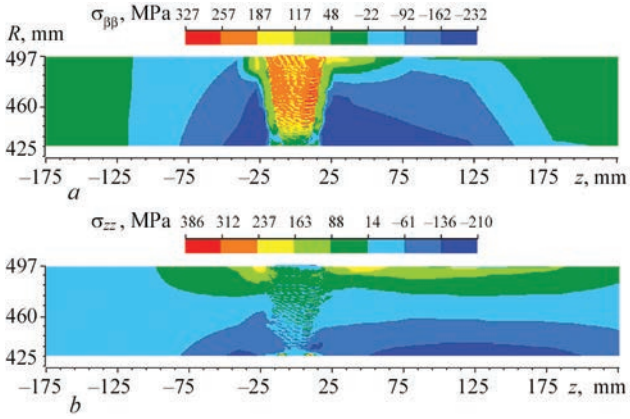

Figure 15. Calculated data on the distribution of residual stresses in the girth weld of the DN850 MCP after heat treatment under a high-temperature tempering mode: *a* — circumferential component; *b* — axial component

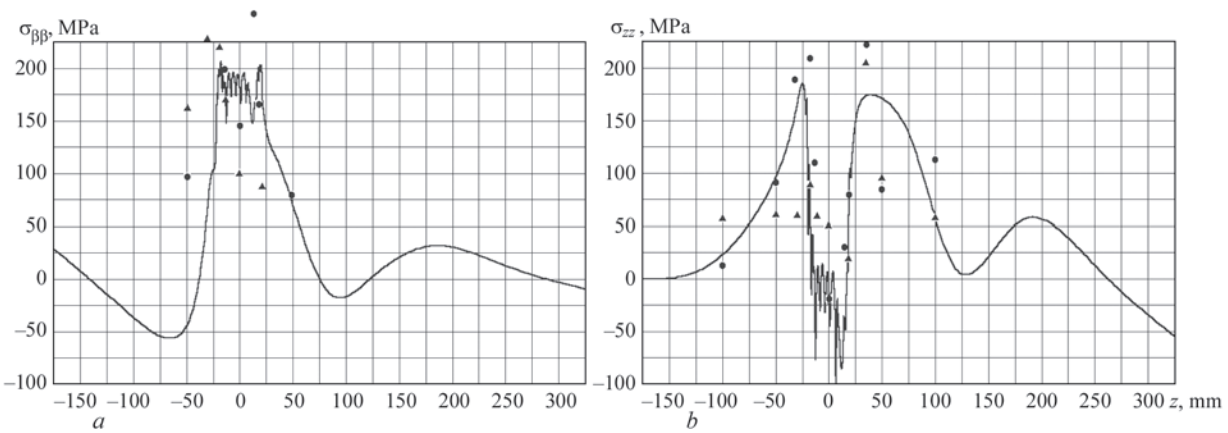

Figure 16. Comparison of calculated and experimental data on the distribution of residual stresses on the outer surface of the welded joint of the DN850 MCP [1]: *a* — circumferential component; *b* — axial component

Experimental measurements of residual stresses were carried out on a welded and heat-treated mock-up specimen of a welded joint. The measurements were taken on the surfaces, i.e. in locations accessible for the installation of strain gauges and the subsequent drilling of holes to implement the well-known Matar method. Measurements were taken at 24 locations. Figure 16 shows a comparison of calculated and experimental data regarding the distribution of residual stresses on the outer surface of the DN850 MCP, which confirmed the high accuracy of the calculation method for determining residual welding stresses.

CONCLUSIONS

The "Girth Weld" computer program is applied for typical cases of welded circumferential joints in pipelines and pressure vessels and enables the computation of the information regarding the mechanical properties of the weld metal and HAZ, residual stresses and strains, determination of the redistribution of the stress-strain state resulting from heat treatment and the effects of operational and test loads, and prediction of the serviceability and life of welded structures with discontinuities (detected by non-destructive testing or postulated).

The software is designed for engineering and scientific applications and does not require the user to have specialist training in computational methods, as it fully automates the processes of creating a mathematical model, meshing the domain, by finite elements executing a solver and visualizing the results.

The program ensures highly accurate predictive results at minimal demands on computing and time resources due to the use of modern approaches to modelling the physico-chemical processes involved in welding, as well as efficient algorithms for solving nonlinear problems and systems of high-order differential equations.

Calculations have been carried out for two test tasks of practical interest that demonstrate the main capabilities of the "Girth Weld" computer program. The verification results indicate that the physical models and processes implemented in the program are correct and correspond to accepted modern approaches to the description of physico-chemical processes during welding heating, mechanics of deformable bodies, and fracture mechanics. Based on the satisfactory agreement between the calculated results and the experimental measurement data obtained from the test specimen (a welded circumferential joint of a DN850 pipeline in the primary circuit of a WWER-1000 reactor, made of 10GN2MFA pearlitic steel), the "Girth Weld" computer program has been validated and may be used to simulate the mechanical properties and stress-strain state in the area of girth butt welds in pipelines and pressure vessels.

REFERENCES

1. Makhnenko, V.I. (2006) *Resource of safe operation of welded joints and units of modern structures*. Kyiv, Naukova Dumka [in Russian].
2. Makhnenko, V.I., Velikoivanenko, E.A., Pochinok, V.E. et al. (1999) Numerical methods for the predictions of welding stresses and distortions. *Welding and Surfacing Reviews*, 13(**1**), 1–146.
3. Yuryev, S.F. (1950) *Specific volumes of phases in the martensitic transformation of austenite*. Moscow, Metallurgizdat [in Russian].
4. (1996) Mannesmann. CCT diagram for steel X10CrMoVNb91. Data Sheet 435 R, material 1/4903.
5. Kasatkin, O.G., Zeiffarth, P. (2002) Calculation models for evaluation of mechanical properties of HAZ metal in welding of low-alloy steels. In: *Proc. of the Inter. Conf. on Mathematical Modeling and Information Technologies in Welding and Related Processes, Kyiv*, 103–106 [in Russian].
6. Belomytsev, M.Yu., Molyarov, V.G. (1994) Study of the structure and construction of the thermokinetic diagram of the decomposition of austenite in 10GN2MFA steel. *Izv. Vuzov. Chyorn. Metallurgiya*, **3**, 47–49 [in Russian].

ORCID

L.M. Lobanov: 0000-0001-9296-2335,
O.V. Makhnenko: 0000-0002-8583-0163,
O.S. Milenin: 0000-0002-9465-7710,
O.A. Velykoivanenko: 0009-0007-3704-2000,
G.P. Rozynka: 0009-0009-1750-7266,
N.R. Basystyuk: 0000-0002-9810-7273,
G.Yu. Saprykina: 0000-0003-1534-7253

CONFLICT OF INTEREST

The Authors declare no conflict of interest

CORRESPONDING AUTHOR

O.V. Makhnenko
E.O. Paton Electric Welding Institute of the NASU
11 Kazymyr Malevych Str., 03150, Kyiv, Ukraine
E-mail: makhnenko@paton.kiev.ua

SUGGESTED CITATION

L.M. Lobanov, O.V. Makhnenko, O.S. Milenin, O.A. Velykoivanenko, G.P. Rozynka, N.R. Basystyuk, G.Yu. Saprykina (2026) Computer program for modelling stress-strain state of a circumferential welded joint. *The Paton Welding J.*, **04**, 24–36.
DOI: https://doi.org/10.37434/tpwj2026.04.04

JOURNAL HOME PAGE

https://patonpublishinghouse.com/eng/journals/tpwj

Received: 24.11.2025
Received in revised form: 10.03.2026
Accepted: 30.04.2026

DOI: https://doi.org/10.37434/tpwj2026.04.05

ANALYSIS OF ACTUAL PROBLEMS OF LASER WELDING OF THIN-WALLED PRODUCTS MADE OF STAINLESS STEELS (REVIEW)

Yu.V. Yurchenko

E.O. Paton Electric Welding Institute of the NASU
11 Kazymyr Malevych Str., 03150, Kyiv, Ukraine

ABSTRACT

This paper reviews current scientific research on laser welding of thin-walled products made of high-alloy corrosion-resistant steels. Particular attention is paid to factors affecting the quality of welded joints in thin-walled structures. One such issue is the formation of craters at the end of the weld, which is often observed in the production of circumferential welds. It has been established that an effective approach to reducing this defect is the use of smooth control of laser radiation power at the beginning and end of the welding process using different types of modulation, as well as overlapping the weld and performing an additional smoothing pass. Another important aspect is ensuring stable gas shielding during welding in a narrow gap between the clamping elements. Design solutions that contribute to the formation of a laminar flow of shielding gas, in particular the use of gas distribution elements made of sintered porous materials or metal meshes, which reduce turbulence and improve the effectiveness of shielding the welding zone from atmospheric influences, were considered. The problem of deformations and residual stresses caused by localized heat input is analyzed separately. It has been established that the use of copper substrates, the optimal location of clamping elements, and the optimization of laser welding parameters can significantly reduce the level of thermal deformations and ensure high geometric accuracy of joints. Based on the results of the review, the main problems of laser welding of thin-walled products made of corrosion-resistant high-alloy steels were identified, options for their solution were considered, and prospects for further research in these areas were outlined.

KEYWORDS: laser welding, corrosion-resistant steels, thin-walled products, welding problems, craters, gas shielding, deformations

INTRODUCTION

The use of thin sheet metal makes it possible to reduce the weight and dimensions of welded structures, as well as lower their production costs. At the current stage of development of welding technologies, significant attention is being paid to the welding of metal with wall thicknesses less than 2 mm in various structures [1]. Thin sheet metal is traditionally used in aircraft, chemical, food and other industries. In the aircraft industry, this includes pipelines, turbine components, fuselages, etc. [2, 3]. As for the chemical industry, this covers pipelines, reservoirs, cisterns, and tanks [4]. The listed products typically have a significant length of welded joints and increased quality requirements. In light industry, particularly in the food industry, most metal products are thin-walled: refrigeration units, pipelines, vessels, reservoirs, and containers for sugar and dairy plants [5].

Among the materials most commonly used in these industries, austenitic stainless steels are the most widespread. They account for about two-thirds of global stainless steel production [6]. Thanks to alloying with nickel, as well as nitrogen and manganese, their structure remains austenitic across the entire temperature range — from cryogenic to melting temperatures. They have excellent formability and weldability, are non-magnetic, and retain ductility at very low temperatures [7, 8]. Among the most common are the 300 series — chromium-nickel alloys, where the austenitic structure is achieved primarily through the addition of nickel [6].

The most common austenitic steels are AISI 304, AISI 316, and AISI 321 (domestic equivalents 08Kh18N10, 03Kh17N14M3, and 12Kh18N10T, respectively). The chemical composition of these steels according to ISO 15510:2014 is shown in Table 1.

Stainless steels AISI 304, AISI 316, and AISI 321 are widely used in industry due to their corrosion resistance and high mechanical properties. AISI 304 is the most common grade used in the food industry, household appliances, architecture, and mechanical engineering. AISI 316 contains molybdenum, which increases its resistance to aggressive environments, particularly those containing chlorine, making it the preferred choice for marine, chemical, and medical applications. AISI 321 is titanium-alloyed and is distinguished by high heat resistance and resistance to intergranular corrosion, making it suitable for use in high-temperature equipment, aircraft manufacturing, and other industries where high operating temperatures are present [6–8].

Given the properties mentioned above, austenitic steels are most commonly used in the manufacture of thin-walled products. To join them, welding process-

Table 1. Chemical composition of the steels, wt.% [9]

Grade	C	Si	Mn	Ni	S	P	Cr	Cu	Ti	Mo	Fe
AISI 304	≤0.08	≤0.8	≤2	9–11	≤0.02	≤0.035	17–19	≤0.3	–	–	Bal.
AISI 316	≤0.03	≤0.4	≤1–2	13–15	≤0.02	≤0.035	16–18	–	–	2.5–3.1	
AISI 321	≤0.12	≤0.8	≤2	9–11	≤0.02	≤0.035	17–19	≤0.3	0.4–1	–	

es must be used that ensure minimal heat input and high-quality welds. The main types of welded joints for thin-walled products are butt joints for plane products and circumferential joints for cylindrical ones (Figure 1).

Currently, the methods for welding thin-walled products most commonly used worldwide are plasma, electron beam, TIG, and MIG welding [10–12].

Despite the variety of welding processes, the methods listed above have their drawbacks. Plasma welding involves high costs for welding equipment and consumables, which can can significantly increase the technology implementation costs [13].

Although electron beam welding is effective, it also has certain drawbacks. The welding equipment required for this technology is complex and expensive, which reduces its accessibility for widespread use. In addition, vacuum chambers are necessary to perform welding operations, which limits the ability to process large or heavy workpieces. Since electron beam welding is performed in sealed vacuum chambers, complex guidance systems are needed for precise positioning of the electron beam and locating the weld site. The process itself is also accompanied by X-ray radiation, which requires special protective measures for personnel [13].

TIG welding also has its disadvantages. In particular, excessive welding current can cause melting of the tungsten electrode, which affects weld quality by forming brittle tungsten in the weld pool. Furthermore, this welding process has a low speed, which limits its efficiency when welding large-scale components [14].

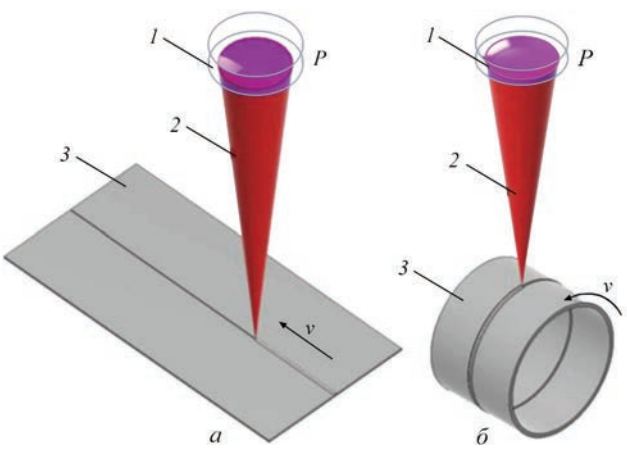

Figure 1. Schematic of laser welding: butt welds (*a*), circumferential welds (*b*): *1* — lens; *2* — laser beam; *3* — workpieces

Among the drawbacks of MIG welding is a less stable welding arc, which can lead to an uneven welding process. Another issue is the feedback from the welding wire, which can sometimes be inconsistent, complicating the control of the welding process. Welding also produces a large amount of smoke and harmful fumes, requiring the use of appropriate ventilation and personnel protection means [12].

Alongside the welding methods for thin-walled products listed above, laser welding is becoming increasingly widespread and implemented. Over the last 10 years, rapid growth in laser technologies has been occurred. Hence the cost per kilowatt of used laser power decreased by approximately 10 times, making laser welding even more competitive compared to traditional welding methods [15]. This is confirmed by data from various consulting agencies, which indicate that the global market for laser welding equipment in 2022–2023 amounted to $2.5–2.9 bln [16–18]. This market is expected to reach approximately $4 bln by 2032, with a compound annual growth rate (CAGR) of 5.5 % over the forecast period [18]. The rapid development of laser technologies is also confirmed by a significant increase in the number of scientific publications related to laser processing, particularly laser welding.

The main advantages of laser welding are: lack of requirements for complex vacuum chambers, the most localized thermal effect, a small heat-affected zone (HAZ), and minimal residual deformation.

Despite the rapid development of laser welding as a highly productive technology featuring deep penetration, minimal deformation, and high processing speeds, a number of technical challenges and issues remain relevant and have yet to be definitively resolved. These include crater formation at the beginning and end of the weld joint, ensuring reliable gas shielding, effective heat removal, control of welding stresses and deformations, as well as reliable clamping of the weld edges of thin-walled products.

THE PURPOSE

This study is aimed at analyzing scientific literature on the laser welding of thin-walled products as well as identifying common problems that arise during the welding of such components; and searching for possible solutions to these problems.

ANALYSIS OF THE PROBLEM OF CRATER FORMATION IN WELDED JOINTS

The formation of craters at the end of a welded joint during laser welding is a well-studied but still relevant issue in the fabrication of circumferential welded joints in thin-walled products. Its relevance is maintained due to changes in welding conditions, specifically the thickness and type of material, the joint design, the type and characteristics of the laser source, as well as the specific geometry of a product. Consequently, the problem is primarily of a technological nature and requires a customized approach. To effectively eliminate craters, it is necessary to seek technical solutions that take into account the specific characteristics of a product, welding parameters, and material properties.

According to the DSTU 3761.3–98 standard [19], a crater is a cavity that forms at the end of a welded joint under the influence of the pressure of the electric arc and/or the gas jet, as well as the volumetric shrinkage of the metal during its crystallization. In international terminology, this defect is referred to as a "crater" (Figure 2). The problem of crater formation at the end of a welded joint has long been known; however, with the development of welding technologies, thin-walled or closed joints — where traditional run-off tabs cannot be used — it has become increasingly relevant [20].

Despite its apparent simplicity, the crater zone is extremely complex in terms of thermodynamics, hydrodynamics, metallurgy, and the stress-strain state. Exactly here, hot cracks, pores, shrinkage cavities, and microinclusions most often occur, which degrade the mechanical properties of the joint, reduce its leak tightness, and, under unfavorable conditions, can lead to premature failure of the welded joint under load [21, 22].

Controlling the welding termination process presents a particular challenge. While most technological solutions are aimed at ensuring a stable weld pool under steady-state conditions, the termination zone is inherently unstable: after the heat source is removed, the nature of heat fluxes, temperature distribution, and crystallization rate change, leading to a local loss of balance in phase and hydrodynamic processes. As a result, the crater becomes a concentration point for residual stresses and a source of crack initiation. In addition to cold cracks, during laser welding of austenitic stainless steels remains the problem of hot crack formation [23, 24]. The main cause of their formation is the presence of residual molten films with a reduced melting point, forming as a result of microsegregation of low-melting elements such as sulfur, phosphorus, copper, and silicon, or the formation of eutectics based on Ni_3S_2, Fe_3P, etc. [23]. Under the action of shrinkage stresses arising during cooling, or due to a sudden change in heat fluxes in the weld termination region, these films lose their integrity, forming hot cracks.

Preventing crater formation at the start and end of a weld is essential for ensuring high-quality and leak-tight welds, especially during laser welding. One of the key approaches to minimizing craters in laser welding is to adjust the heat balance at the start and end of the weld.

The most common and effective strategy for preventing crater formation is to reduce the laser power at the end of the weld (ramp-down) [20]. The method of reducing the laser power at the end of the weld allows lowering the temperature in the weld pool, promoting uniform crystallization. By reducing temperature gradients and cooling rates, shrinkage stresses are reduced, susceptibility to hot cracks is decreased, and the risk of shrinkage cavities forming in the crater is minimized [20]. In [20], Kenda et al. used three variants of laser power reduction (RD) profiles (Figure 3).

Profile P_1 is a classic mode with a linear power reduction of −1.5 W/ms for the transition from deep melting to the heat conduction mode. Profile P_2 is a new approach with a zigzag-shaped decline: initially to 73 % of power, followed by 53 Hz modulation with a slope of −0.15 W/ms. Profile P_3 is similar to P_2, but with a frequency of 106 Hz and a slope of −0.25 W/ms. Figure 4 shows a top view of three typical weld joint ends made using RD profiles P_1, P_2, and P_3, shown in Figure 3 [22]. When welding with the P_1 profile, the surface of the welded joint is smooth but

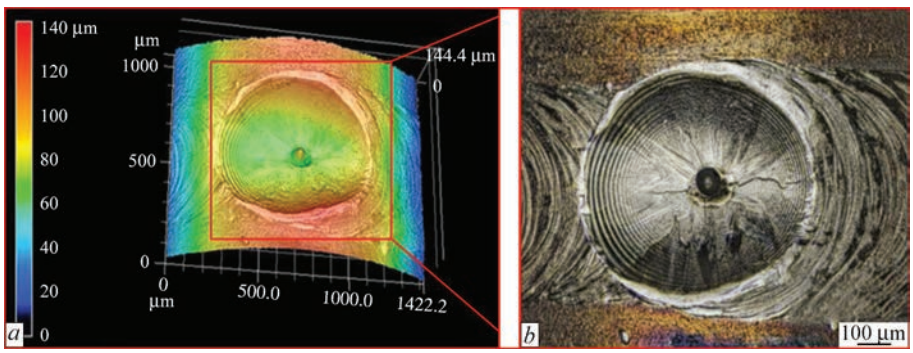

Figure 2. Crater with cracks at the end of a welded joint during laser welding: 3D scan of the crater (*a*), top view of the crater (*b*) [20]

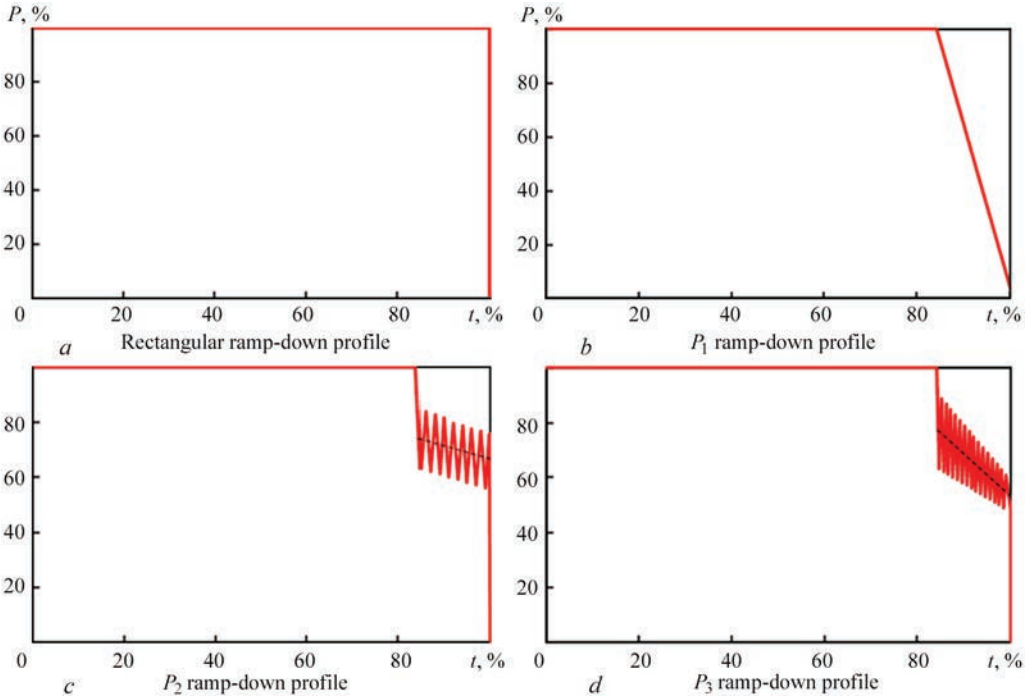

Figure 3. Laser power reduction profiles: rectangular (*a*), P_1 (*b*), P_2 (*c*), P_3 (*d*) [20]

has several long axial cracks, which typically occur under such conditions (Figure 4, *a*). These cracks initiate at the moment of power reduction, and in a certain zone of the welded joint, their parallel existence across the width is observed. The surface of the weld termination zone when using zigzag profiles P_2 and P_3 (Figure 4, *b*, *c*) has an arc-shaped structure, i.e., it contains distinct crystallization zones. The number of

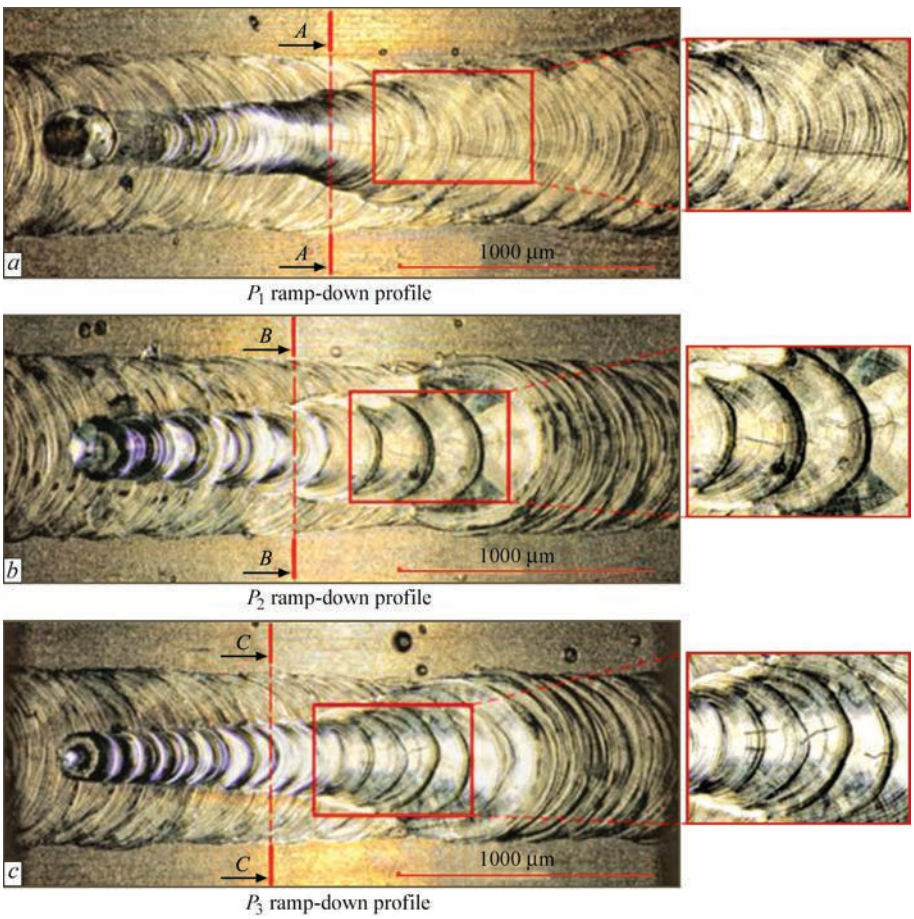

Figure 4. Comparison of crack morphology on the surface of a welded joint for different laser power reduction profiles: P_1 (*a*); P_2 (*b*); P_3 (*c*) [20]

such zones corresponds to the number of power modulation cycles incorporated into the corresponding RD profile. Figures 4, *b*, *c* also show that only short surface cracks form during usage of zigzag profiles. This is explained by the fact that powerful modulation of the laser beam creates crystallization zones that act as barriers to crack propagation [20].

There are several other methods for preventing crater formation, namely: defocusing of the laser beam, overlap welding, and the use of a "smoothing" weld [25]. A drawback of the laser beam defocusing method is the need for complex optical systems in the welding heads that ensure controlled changes in focal length. This complicates the equipment design, increases its cost, and raises maintenance requirements. The "smoothing" weld method requires an additional pass, which also increases processing time and introduces additional internal stresses due to repeated thermal exposure.

Based on a review of scientific studies dedicated to the investigation of crater formation at the end of a welded joint, the following conclusion can be drawn. Despite the existence of a certain number of scientific studies in this field, the issue of crater formation during laser welding of thin-walled welded joints made of stainless steel remains incomplete. Therefore, further research in this area remains relevant.

ANALYSIS OF THE PROBLEM OF GAS SHIELDING IN THE WELDING ZONE

The problem of gas shielding during welding with concentrated energy sources is particularly relevant due to the fact that most methods involve welding in the open air without the use of vacuum chambers. In these cases, gas shielding plays a key role. Due to high temperatures and the localized effect of the heat source, even a slight ingress of air into the welding zone can lead to the formation of oxide films, pores, cracks, and other defects. This degrades the metal's structure and reduces the strength and durability of welded joints [26–29]. One of the main factors reducing the effectiveness of gas shielding during welding is flow turbulence. During the transition from laminar to turbulent flow, the shielding gas mixes intensively with the surrounding air, causing the oxygen concentration in the weld zone to rise rapidly (Figure 5) [30, 31]. Due to momentum exchange at the transition layer with the surrounding environment or with the wall (i.e., the metal surface), the velocity profile undergoes asymmetric changes with increasing propagation length [32]. Therefore, the analysis of near-surface and free flows [33] allows for the evaluation of the efficiency of shielding gas delivery through flat or tubular nozzles.

Near-surface flows exhibit a significantly longer laminar flow region and lower turbulence at the same Reynolds number [34], indicating the advantage of flat nozzles over other shapes. The shielding gas flow rate is one of the most extensively studied parameters due to the ease of its adjustment. Blackburn et al. [35] found that reducing the flow rate improves the appearance of the weld, as excessively high flow rates cause turbulence in the gas flow. Vyskoč [36] investigated the effect of flow rate on the shape of the weld and found that its growth reduces the energy absorbed by the plasma torch while simultaneously increasing the weld width. This study analyzed the relationship between the shielding gas supply distance and the porosity of the weld. The optimal supply distance allowed for the stabilization of the vapor-gas channel and a reduction in porosity. In addition to gas flow rate, the researchers also focused on the position of the shielding gas nozzle [37]. Campana et al. [38] concluded that for effective shielding, the gas must be supplied at a right angle to the workpiece surface, and the nozzle height must be minimized to ensure reliable shielding of the vapor-gas channel and the high-temperature welding zone. Wang et al. [39] investigated the effect of the nozzle angle and found that as the angle decreases, the size of the gas shielding zone increases.

The most characteristic sign of insufficient gas shielding in the weld zone is the formation of oxide films on the metal surface, known as heat tint. On corrosion-resistant steels, such oxide films form at temperatures above 300 °C. Their thickness depends on

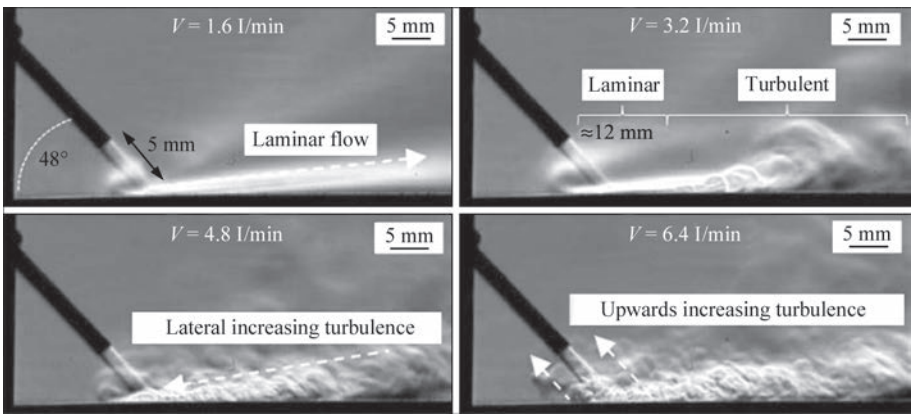

Figure 5. Helium flow pattern as a function of the gas injection rate, visualized using a Schlieren image [31]

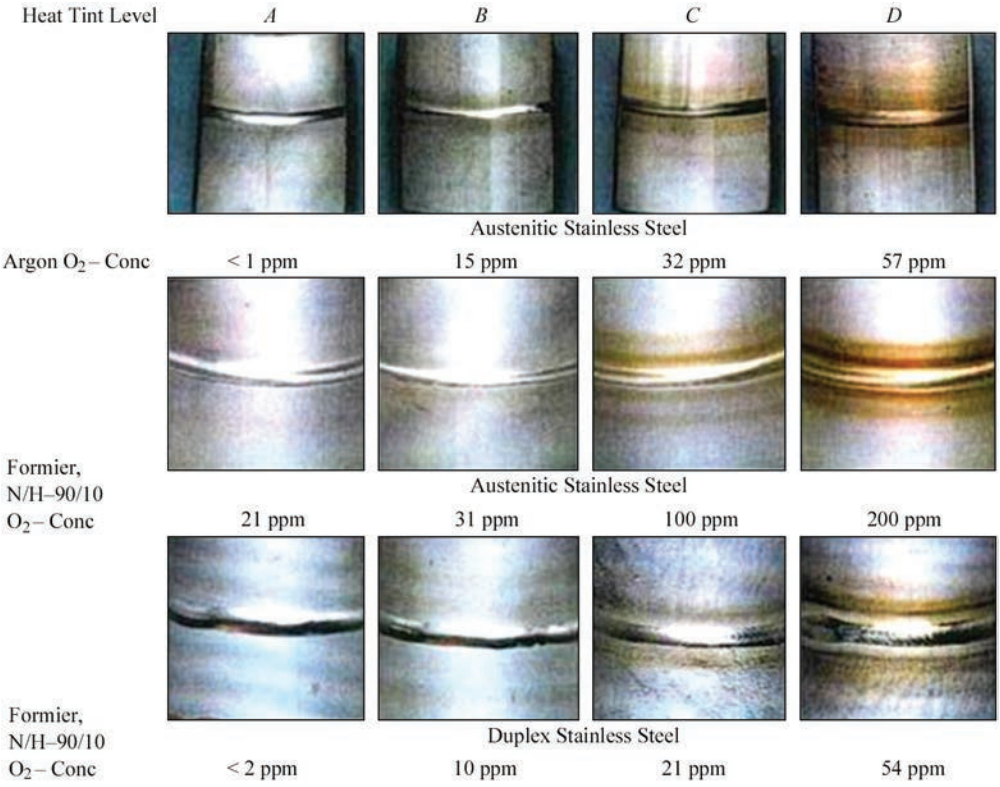

Figure 6. Colors of oxide films on the surface of stainless steel as a function of concentration in the weld zone [41]

the temperature regime, heating duration, and oxygen content in the weld zone (Figure 6). Areas with oxide films are characterized by lower corrosion resistance compared to the base metal, which can lead to the development of localized corrosion [27, 40].

The color of the oxide films formed during welding varies from light straw-colored to dark blue, depending on the temperature. This is due to the formation of oxide films composed primarily of chromium and iron. During oxidation, alloying elements, particularly chromium, can diffuse to the surface because they oxidize more readily than iron [26]. As a result, a zone with reduced chromium content forms beneath the film, which negatively affects the corrosion resistance of this area compared to the rest of the steel volume [42]. The rate of oxidation and the degree of depletion of alloying elements in the zone beneath the film are determined not by the overall chemical composition of the steel, but by the properties of the oxide film itself, particularly its diffusivity [43]. Due to its heterogeneous structure, the presence of defects, and internal stresses, such an oxide film does not provide reliable protection against corrosion. In appropriate environments, this can lead to localized corrosion in the zone with reduced chromium content located beneath the film [44].

During service, welded joints made of stainless steels may be exposed to various types of corrosion, namely: pitting, crevice, intergranular, and stress corrosion [27, 45–49]. The protective passive film on the surface of stainless steel provides high resistance to uniform corrosion in typical oxidizing environments. However, in the presence of aggressive factors, local destruction of this film is possible, leading to the development of pitting corrosion [47, 50]. The effect of elevated temperatures in the range of 500–800 °C (so-called "critical temperatures") during welding followed by slow cooling in air makes 2 mm thick AISI 304 austenitic stainless steel susceptible to intergranular corrosion [48, 51, 52]. Under these conditions, chromium carbides precipitate along the grain boundaries, reducing the chromium content in the adjacent zone.

If the chromium concentration falls below the critical level for passivation (approximately 11.5 %), this zone becomes anodic relative to the rest of the grain, leading to sensitization of the material and its susceptibility to intergranular corrosion [52]. Chromium-depleted zones can also become pathways for the preferential development of other types of localized corrosion or crack propagation under tensile stresses [53].

To prevent the formation of oxide films on the metal surface during welding and reduce the probability of corrosive damage, special gas shielding systems are used. These systems supply shielding gas to the welding zone to isolate the molten metal and surrounding areas from contact with oxygen, nitrogen, and moisture in the surrounding environment. The development of effective gas shielding devices is a relevant area of research, as the quality of a welded joint largely depends on the stability and uniformity of the gas flow. A number of scientific papers have proposed

technical solutions aimed at forming a laminar flow of shielding gas, which provides a more efficient shielding and minimizes the formation of defects in the welded joint [30, 54, 55].

One of the key techniques for ensuring reliable gas shielding involves the gradual formation of a uniform laminar flow. To initially equalize the gas velocity, diffusers made of sintered metal or metal foam are used, which significantly reduce turbulence and ensure a more uniform gas distribution [30]. Depending on the shielding quality requirements and the nozzle design, both individual elements as well as their combinations may be used. For example, a honeycomb structure may be installed downstream of the diffuser to direct the flow along the nozzle axis, effectively reducing transverse velocity fluctuations. To achieve sufficient stabilization, a length-to-diameter ratio of the holes of at least 5:1 is selected, which suppresses turbulence and promotes the formation of a laminar flow [54]. An important role is played by the design, which avoids abrupt changes in the shape and cross-section of the nozzle's internal channels. Transition areas between sections are designed with radius, which reduces the probability of flow separation and the formation of new turbulence zones. Such a smooth flow path ensures a uniform laminar flow, especially if the channel length is sufficient to form a full-fledged parabolic velocity profile [30]. Another common technique is the use of multiple shielding gas flow directions [55]. The gas is supplied both directly to the welding zone and into the surrounding area. This is achieved through separate channels: one directed straight at the welding zone, another at an angle or opposite to the beam's direction of travel to prevent air ingress, and a third through a central chamber with subsequent distribution via a honeycomb structure. In addition, the devices incorporate welding fume extraction systems that do not disrupt the main flow of shielding gas. For this purpose, extraction nozzles that extract gas only from the periphery, leaving the central zone with a clean inert atmosphere, are used [55].

A review of the scientific works on gas shielding reveals that there are currently studies devoted to the general patterns of laminar flow formation during welding with a relatively large gap between the clamping elements. However, the development of devices capable of ensuring an effective laminar gas flow in a narrow gap between closely spaced clamping elements remains outside the scope of research. This confirms the relevance of creating gas shielding devices for such welding conditions.

ANALYSIS OF THE PROBLEM OF WELDING STRESSES AND DEFORMATIONS

Welding with highly concentrated energy sources inevitably leads to the formation of residual stresses and deformations after the weld zone has cooled. Due to local thermal effects and subsequent uneven cooling, internal stresses and deformations appear, which can significantly affect the geometric accuracy and strength of structures [56]. Figure 7 shows typical forms of deformations that occur during the welding of plane parts. Transverse and longitudinal shrinkage, as well as angular deformation, are the three main types of welding deformations that typically occur together in actual welded structures [57].

During welding of thin sheet metal, where the heat input is large relatively to the material thickness, bending-type deformations may occur [57]. Such deformations are one of the main causes of dimensional

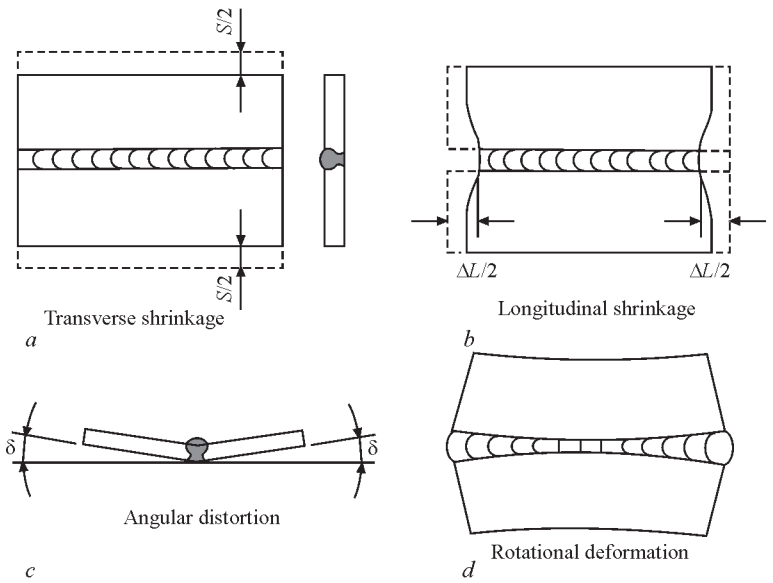

Figure 7. Typical deformations during welding: transverse shrinkage (*a*); longitudinal shrinkage (*b*); angular distortion (*c*); rotational distortion (*d*) [57]

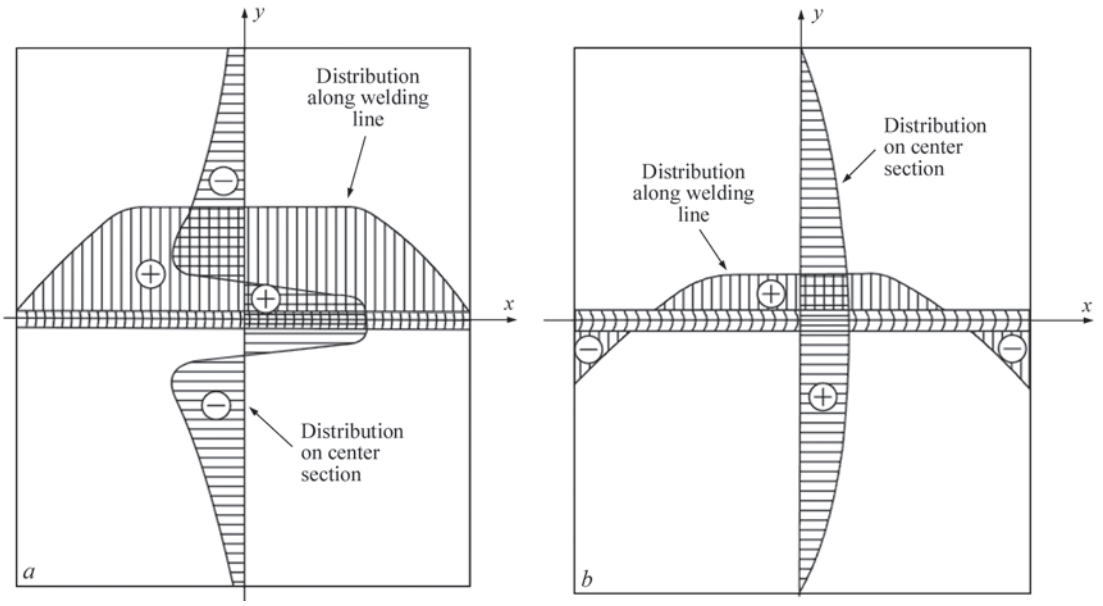

Figure 8. Schematic of residual welding stresses: stresses in the welding direction (*a*), stresses in the transverse direction (*b*) [57]

inaccuracies and lead to a reduction in the stiffness and load-bearing capacity of welded structures made of thin sheet steel. Figure 8 illustrates the distribution of residual stresses in a butt weld joint. Specifically, Figure 8, *a* shows the distribution of longitudinal residual stresses (in the direction of welding) both along the weld and in the cross-section at its center. Maximum tensile residual stresses are observed in the zone around the weld line. In areas distant from the weld zone, compressive stresses form to maintain equilibrium. Along the weld line, residual stresses at its ends decrease to zero due to free boundaries. Similarly, Figure 8, *b* shows the distribution of transverse residual stresses: they are tensile at the center and compressive at the beginning and end of the weld, while at the edges of the sheet they approach zero [57].

The level of welding distortions and residual stresses is significantly determined by the heat input. As a rule, both residual stresses and the degree of distortion grow with an increase in heat input [58]. In this regard, laser welding, which is characterized by high energy density, is advantageous because it requires less heat input compared to other welding methods [59].

The development of residual stresses during welding is related to the interaction of metallurgical changes and microstructure morphology. Tensile residual stresses negatively affect structural integrity, whereas compressive residual stresses typically have a positive effect, in particular by increasing fatigue strength [60, 61]. Stress variations caused by grain size may result from variations in the properties of the austenitic and ferritic phases, including elastic deformation, thermal, and plastic mismatch. At the same time, the crystal lattice parameter, which is a function of the interstitial atom content, is crucial for interpreting the desired residual stresses in the expanded austenite of AISI 316 steel [62]. On the other hand, it has been proven that solid-phase transformation influences the distribution of residual stresses in corrosion-resistant AISI 304 steel to a certain extent, but this influence is not significant [63].

A study [60] investigated the influence of microstructure and heat input on residual stresses following laser welding of 1-mm-thick AISI 304 stainless steel. During the experiments, laser welding was performed with a constant laser power of 750 W, while the welding speed was varied in the range of 0.6–1 m/min, and the defocusing value was varied from 0 to –1 mm. It was established that a chromium-to-nickel equivalent ratio of approximately 1.69 confirms a ferrite-austenite crystallization mode, in which the microstructure consists of a combined phase of acicular and lamellar δ-ferrite in an austenitic matrix. The maximum δ-ferrite content (12 %) is achieved at the lowest heat input of 45 J/mm, whereas when increased to 75 J/mm, its content decreases to 7–8 %. As the heat input grows, the dendrite thickness increases from 484 to 927 nm, and the interdendritic spacing doubles from 3 to 6 μm, while there is a decrease in lamellar δ-ferrite in favor of acicular δ-ferrite.

The highest quality of the welded joint is observed with minimal heat input, which is explained by the very fine dendritic structure and minimal interdendritic spacing. The higher coefficient of thermal expansion of nickel compared to chromium causes tensile stresses in the γ-austenitic phase and compressive stresses in the δ-ferritic dendritic phase. At low heat input, which increases the chromium content and decreases the nickel content, compressive stresses arise that contribute to a reduction in residual stresses. Furthermore, reducing the heat in-

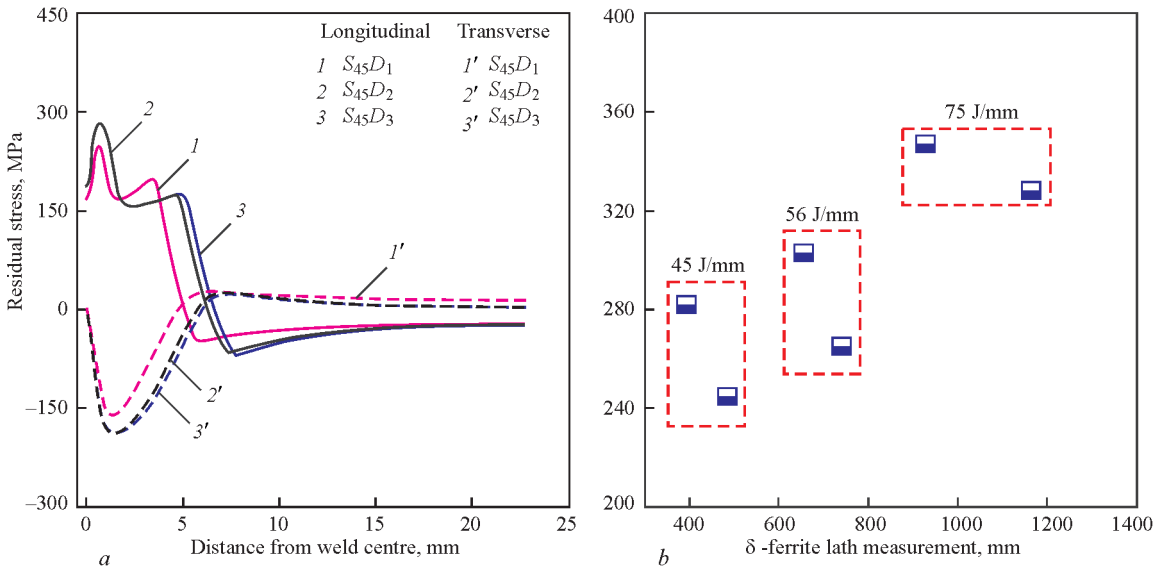

Figure 9. Distribution of residual stresses at a low heat input of 45 J/mm (*a*), variation in the size of primary δ-ferrite dendrites as a function of residual stresses (*b*) [60]

put from 75 to 45 J/mm^2 reduces the longitudinal tensile stresses to 245 MPa, which is below the yield strength, and the transverse residual stresses change from tensile to compressive (Figure 9) [60].

Several approaches can be used to reduce stress and strain levels, such as the use of closely spaced external clamping elements when welding straight-seam pipe joints. External clamping elements significantly reduce residual stresses and welding deformations by more than 30 % compared to the option that excludes usage of clamping elements [64]. The use of copper backing plates on the reverse side of the welded joint also significantly reduces residual stresses and deformations [65].

ANALYSIS OF THE RESULTS OF THE STUDIES REVIEWED

Based on the results of a literature review of recent scientific studies on the topic of laser welding of thin-walled products, the following has been established:

1. The formation of craters at the end of a welded joint during laser welding is a well-studied but still relevant issue in the fabrication of circumferential joints in thin-walled products. The relevance of this issue is predetermined by varying welding conditions, such as material thickness and type, joint design, laser source characteristics, the geometry of a workpiece, etc. The problem bears a technological nature and requires an individual approach for a specific product. Despite the availability of studies, they are mainly focused on the welding of dissimilar metals or carbon steels [20, 25]. The number of studies specifically addressing the welding of thin-walled products made of austenitic stainless steel remains limited. This creates a need for further research aimed at preventing crater formation during the welding of thin-walled products with an axis of rotation made of stainless steels. One of the most promising approaches to eliminating crater formation is the use of a smooth increase and decrease in laser power at the beginning and end of the welding process, respectively. The use of zigzag power modulation allows for reducing the length of crystallization cracks in the crater and limiting their penetration into the welded joint [20]. In addition, overlap welding and smoothing welds also help reduce the risk of crater formation and crystallization cracks [25]. Future research prospects lie in optimizing the profiles of laser power ramp-up and ramp-down during the welding process, taking into account the specific joint geometry and material properties.

2. Gas shielding during laser welding of thin-walled products in a narrow gap between clamping elements is essential for preventing the formation of oxide films and pores, as well as for maintaining the corrosion resistance of the joints. Currently, there are studies dedicated to the general patterns of laminar flow formation during welding with a relatively large gap between the clamping elements [30, 54, 55]. However, the development of devices capable of ensuring an effective laminar gas flow in the narrow gap between closely spaced clamping elements remains outside the scope of research. This confirms the relevance of creating gas shielding devices for such welding conditions. To reduce turbulence in the flow and ensure stable and continuous gas shielding in the welding area, the use of additional gas distribution elements in the design of the gas shielding device based on metal meshes or sintered porous metal is promising, as these elements allow for stabilization of the flow velocity and reduction in the intensity of mixing with atmospheric air [30, 54]. The length-to-diameter ratio of the outlet channel also plays an important role; it must be

at least 5:1 to ensure the stability of the laminar flow [54, 55]. Further research should focus on development of a gas shielding device for welding in conditions of a narrow gap between the clamping elements, which would ensure a stable laminar flow of shielding gas.

3. The problem of deformations and residual stresses in thin-walled welded structures is particularly critical due to the low stiffness of the components and their high sensitivity to thermal effects. Even when using laser welding, which involves a lower heat input compared to other welding methods, deformations caused by a concentrated heat source can lead to a loss of respective geometric accuracy and strength in the products and welded joints [56, 57]. Among known solutions, the most effective are the use of copper backing plates, which, due to their high thermal conductivity, ensure effective heat dissipation and reduce the size of the HAZ, as well as the optimization of laser welding parameters, which reduce stress and deformation levels in welded products [60, 64, 65]. An important condition for the effectiveness of these solutions is the optimal placement of the clamping elements and ensuring a full contact of the parts with the copper backing. Further research could focus on studying stresses and deformations in the welded part at different distances between the clamping elements.

CONCLUSIONS

An analysis of scientific studies on the laser welding of thin-walled products has established that:

1. An effective approach to eliminating crater defects at the end of a weld is the usage of special laser power modulation profiles at the end of the welding process. The use of zigzag modulation with a frequency of 53–106 Hz and a power reduction slope of −0.15 – −0.25 W/ms allows for a significant reduction in the length of crystallization cracks that form in the crater and lowers the risk of their penetration into the welded joint, thereby increasing the reliability and leak-tightness of the structure. In addition, welding with an overlap as well as a smoothing weld using reduced laser power also helps reduce the risk of crater formation and crystallization cracks.

2. To ensure a stable laminar flow of shielding gas, it is advisable to use devices with sintered metal diffusers and channels having a length-to-diameter ratio of at least 5:1. Such technical solutions help reduce turbulence, limit the ingress of atmospheric air into the welding zone, and prevent the formation of oxide films that reduce the corrosion resistance of the joint.

3. For 1-mm-thick AISI 304 steel, optimizing laser welding parameters specifically reducing the heat input to 45 J/mm allows for a reduction in longitudinal residual stresses to 245 MPa, which is below the yield strength, and transforms the transverse stresses from tensile to compressive. The additional use of copper backing plates and clamping elements ensures effective heat dissipation and reduces deformation by more than 30 %, which is important for ensuring the geometric accuracy and reliability of thin-walled products.

REFERENCES

1. Azanaw, G.M. (2025) Thin-walled structures in structural engineering: A comprehensive review of design innovations, stability challenges, and sustainable frontiers. *American J. of Materials Synthesis and Processing*, 10(**1**), 18–26. DOI: https://doi.org/10.11648/j.ajmsp.20251001.13
2. Trzepieciński, T., Najm, S.M., Sbayti, M. et al. (2021) New advances and future possibilities in forming technology of hybrid metal-polymer composites used in aerospace applications. *J. of Composites Sci.,* 5(**8**), 217. DOI: https://doi.org/10.3390/jcs5080217
3. Zhou, B., Liu, B., Zhang, S. (2021) The advancement of 7XXX series aluminum alloys for aircraft structures: A review. *Metals,* 11(**5**), 718. DOI: https://doi.org/10.3390/met11050718
4. Manfredi, J. (2019) Stainless steel application and fabrication in the biotech industry. In: *Filtration and Purification in the Biopharmaceutical Industry.* Third Edition, 169–190. DOI: https://doi.org/10.1201/9781315164953-8
5. Dewangan, A.K., Patel, A.D., Bhadania, A.G. (2015) Stainless steel for dairy and food industry: A review. *J. of Material Science & Engineering,* **4**, 5. DOI: https://doi.org/10.4172/2169-0022.1000191
6. Dutta, S. (2018) Different types and new applications of stainless steel. *Stainless Steel*, 62(**5**), 86–91. https://www.researchgate.net/profile/S-Dutta/publication/330383386_Different_Types_and_New_Applications_of_Stainless_Steel/links/5c3d6a31a6fdccd6b5ad9ee0/Different-Types-and-New-Applications-of-Stainless-Steel.pdf
7. Zheng, C., Yu, W. (2018) Effect of low-temperature on mechanical behavior for an AISI 304 austenitic stainless steel. *Materials Sci. and Engineering: A*, **710**, 359–365. DOI: https://doi.org/10.1016/j.msea.2017.11.003
8. Sunny, K.T., Korra, N.N. (2021) A systematic review about welding of super austenitic stainless steel. *Materials Today Proceedings,* **47**, 4378–4381. DOI: https://doi.org/10.1016/j.matpr.2021.05.185
9. (2014) ISO 15510:2014: *Stainless steels — Chemical Composition.* Ed. 2. International organization for standardization. https://www.iso.org/obp/ui/en/#iso:std:iso:15510:ed-2:v1:en
10. Boulos, M. I., Fauchais, P., Pfender, E. (2023) *Plasma torches for cutting, welding and PTA coating*. Springer eBooks*,* 1–83. DOI: https://doi.org/10.1007/978-3-319-12183-3_47-1
11. Węglowski, M., Błacha, S., Phillips, A. (2016) Electron beam welding — Techniques and trends — Review. *Vacuum*, **130**, 72–92. DOI: https://doi.org/10.1016/j.vacuum.2016.05.004
12. Ogundimu, E.O., Akinlabi, E.T., Erinosho, M.F. (2019) Comparative study between TIG and MIG welding processes. *J. of Physics Conference Series*, 1378(**2**), 022074. DOI: https://doi.org/10.1088/1742-6596/1378/2/022074
13. Khoshnaw, F., Krivtsun, I., Korzhyk, V. (2023) *Welding of metallic materias. Methods, metallurgy, and performance.* Chapter 2. Arc welding methods. Elsevier eBooks, 37–71. DOI: https://doi.org/10.1016/b978-0-323-90552-7.00004-3
14. Ahmad, A.Y., Al-Qenaei (2016) Fusion welding techniques. *Inter. J. of Eng. Research and Applications,* 6(**3**), 78–83. https://www.academia.edu/download/47559936/M6302078083.pdf
15. Yurchenko, Yu.V., Bernatskyi, A.V., Siora, O.V. et al. (2024) Analysis of actual problems of laser welding of stainless steel thin sheets and search for solutions. *Inter. J. of Sci. Eng. and Technology*, 12(**5**), 1–9. DOI: https://doi.org/10.61463/ijset.vol.12.issue5.289

16. Singh, A., Singh, S. (2024) Laser welding machine market size, forecast 2024–2032. In: *Global Market Insights Inc*. https://www.gminsights.com/industry-analysis/laser-welding-machine-market
17. (2022) *Laser Welding Market Size, Industry Share & Trends – 2032*. https://www.futuremarketinsights.com/reports/laser-beam-welding-equipment-market
18. Allied Market Research (2023) *Laser Welding System Market Size, Share, Competitive Landscape and Trend Analysis Report, by Laser type, by Power, by Application: Global Opportunity Analysis and Industry Forecast, 2023–2032*. Allied Market Research. https://www.alliedmarketresearch.com/laser-welding-system-market-A135089
19. DSTU 3761.3–98: *Welding and allied processes.* Pt 3. Welding of metals: Welded joints and welds, technology, materials and equipment. Terms and definitions.
20. Kenda, M., Klobčar, D., Nagode, A., Bračun, D. (2021) Analysis and prevention of weld crater cracking in circumferential laser microwelding of automotive pressure sensors. *Engineering Failure Analysis*, **128,** 105579. DOI: https://doi.org/10.1016/j.engfailanal.2021.105579
21. Artinov, A., Karkhin, V., Bachmann, M., Rethmeier, M. (2020) Mathematical modeling of the geometrical differences between the weld end crater and the steady-state weld pool. *J. of Laser Applications*, **32**, 022024. DOI: https://doi.org/10.2351/7.0000068
22. Lai, W.J., Ganguly, S., Suder, W. (2020) Study on effect of laser keyhole weld termination regimes and material composition on weld overlap start-stop defects. *J. of Manufacturing Processes*, **58**, 416–428. DOI: https://doi.org/10.1016/j.jmapro.2020.08.012
23. Norouzian, M., Elahi, M.A., Plapper, P. (2023) A review: Suppression of the solidification cracks in the laser welding process by controlling the grain structure and chemical compositions. *J. of Advanced Joining Processes*, **7**, 100139. DOI: https://doi.org/10.1016/j.jajp.2023.100139
24. Wang, D., Zhang, F., Warinsiriruk, E. et al. (2024) A novel method for evaluating solidification cracking susceptibility of austenitic stainless steel using trapezoidal hot cracking test during laser welding. *Optics & Laser Technology*, **175**, 110789. DOI: https://doi.org/10.1016/j.optlastec.2024.110789
25. Gook, S., Üstündag, Ö., Gumenyuk, A., Rethmeier, M. (2019) Avoidance of end crater imperfections at high-power laser beam welding of closed circumferential welds. *Welding in the World*, **64**, 407–417. DOI: https://doi.org/10.1007/s40194-019-00841-x
26. Łabanowski, J., Głowacka, M. (2011) Heat tint colours on stainless steel and welded joints. *Welding Inter.*, 25(**7)**, 509–512. DOI: https://doi.org/10.1080/09507116.2010.540837
27. Bobić, B., Jegdić, B., Gligorijević, B. (2014) Analysis of corrosion damage in a boiler made of AISI 304L stainless steel. *Zastita Materijala*, 55(**1**), 33–37. DOI: https://doi.org/10.5937/zasmat1401033b
28. McNicol, J., Narayanan, B., Sridhar, N., Fink, C. (2022) Corrosion resistance of austenitic stainless steel welds with no-backing gas. *Welding in the World*, **67**, 819–830. DOI: https://doi.org/10.1007/s40194-022-01442-x
29. Wickström, L., Hinds, G., Turnbull, A. (2015) Influence of weld preparation procedure and heat tinting on sulfide stress corrosion cracking of duplex stainless steel. *Corrosion*, 71(**8**), 1036–1047. DOI: https://doi.org/10.5006/1645
30. Schricker, K., Baumann, A., Bergmann, J.P. (2021) Local shielding gas supply in remote laser beam welding. *J. of Manufacturing and Materials Processing*, 5(4), 139. DOI: https://doi.org/10.3390/jmmp5040139
31. Schmidt, L., Hickethier, S., Schricker, K., Bergmann, J.P. (2019) Low-spatter high speed welding by use of local shielding gas flows. *High-Power Laser Materials Processing: Applications, Diagnostics, and Systems VIII*, **10911**, 185–197. DOI: https://doi.org/10.1117/12.2507024
32. Gersten, K. (1998) Turbulent boundary layers. In:*Recent Advances in Boundary Layer Theory. CISM International Centre for Mechanical Sciences*, Vol. **390**. Ed. by A. Kluwick. Springer, Vienna. DOI: https://doi.org/10.1007/978-3-7091-2518-2_5
33. Gersten, K., Herwig, H. (1992) *Strömungsmechanik. Grundlagen der Impuls-, Wärme- und Stoffübertragung aus asymptotischer Sicht:* Textbook. DOI: https://doi.org/10.1007/978-3-322-93970-8
34. Gogineni, S., Shih, C. (1997) Experimental investigation of the unsteady structure of a transitional plane wall jet. *Experiments in Fluids*, **23**, 121–129. DOI: https://doi.org/10.1007/s003480050093
35. Blackburn, J., Allen, C., Hilton, P., Li, L. (2010) Nd:YAG laser welding of titanium alloys using a directed gas jet. *J. of Laser Applications*, **22**, 71–78. DOI: https://doi.org/10.2351/1.3455825
36. Vyskoč, M., Sahul, M., Dománková, M. et al. (2020) The effect of process parameters on the microstructure and mechanical properties of AW5083 aluminum laser weld joints. *Metals*, 10(**11**), 1443. DOI: https://doi.org/10.3390/met10111443
37. Deepan Bharathi Kannan, T., Sathiya, P., Ramesh, T. (2017) Experimental investigation and characterization of laser welded NiTinol shape memory alloys. *J. of Manufacturing Processes*, **25**, 253–261. DOI: https://doi.org/10.1016/j.jmapro.2016.12.006
38. Campana, G., Ascari, A., Fortunato, A., Tani, G. (2008) Hybrid laser-MIG welding of aluminum alloys: The influence of shielding gases. *Applied Surface Science*, 255(**10**), 5588–5590. DOI: https://doi.org/10.1016/j.apsusc.2008.07.169
39. Wang, H., Shi, Y., Gong, S., Duan, A. (2007) Effect of assist gas flow on the gas shielding during laser deep penetration welding. *J. of Materials Processing Technology*, 184(**1–3**), 379–385. DOI: https://doi.org/10.1016/j.jmatprotec.2006.12.014
40. Jegdić, B.V., Bobić, B.M., Prokolab, M.M. (2013) Influence of heat tint on corrosion resistance of stainless steels. *Zavarivanje i Zavarene Konstrukcije*, 58(**3**), 121–126. https://scindeks.ceon.rs/article.aspx?artid=0354-79651303121J
41. Frantsen, J.E., Mathiesen, T., Hattesen, K.U. et al. (2008) Common corrosion problems in the brewery sector. *Force Technology*, NACE-08176. https://onepetro.org/NACE-CORR/proceedings-abstract/CORR08/All-CORR08/118824
42. Mahajanam, S., Heidersbach, K. (2021). Corrosion studies of heat-tinted austenitic stainless steel. *Material Performance*. https://nace.mydigitalpublication.com/publication/?i=704427&article_id=4006538&view=articleBrowser&ver=html5
43. Yu, Y., Shironita, S., Souma, K., Umeda, M. (2018) Effect of chromium content on the corrosion resistance of ferritic stainless steels in sulfuric acid solution. *Heliyon*, 4(**11**), e00958. DOI: https://doi.org/10.1016/j.heliyon.2018.e00958
44. Sun, M., Du, C., Liu, Z. et al. (2021) Fundamental understanding on the effect of Cr on corrosion resistance of weathering steel in simulated tropical marine atmosphere. *Corrosion Science*, **186**, 109427. DOI: https://doi.org/10.1016/j.corsci.2021.109427
45. Zatkalíková, V., Uhríčik, M., Markovičová, L., Kuchariková, L. (2022) Corrosion behavior of sensitized AISI 304 stainless steel in acid chloride solution. *Materials,* 15(**23**), 8543. DOI: https://doi.org/10.3390/ma15238543
46. Wu, X., Liu, Y., Sun, Y. et al. (2020) A discussion on evaluation criteria for crevice corrosion of various stainless steels. *J. of Material Science and Technology*, **64**, 29–37. DOI: https://doi.org/10.1016/j.jmst.2020.04.017
47. Parangusan, H., Bhadra, J., Al-Thani, N. (2021) A review of passivity breakdown on metal surfaces: influence of chloride- and sulfide-ion concentrations, temperature, and pH. *Emergent Materials*, **4**, 1187–1203. DOI: https://doi.org/10.1007/s42247-021-00194-6

48. Bansod, A.V., Patil, A.P., Moon, A.P., Khobragade, N.N. (2016) Intergranular corrosion behavior of low-nickel and 304 austenitic stainless steels. *J. of Materials Engineering and Performance*, **25**, 3615–3626. DOI: https://doi.org/10.1007/s11665-016-2221-2
49. Toppo, A., Pujar, M., Sreevidya, N., Philip, J. (2018) Pitting and stress corrosion cracking studies on AISI type 316N stainless steel weldments. *Defence Technology*, 14(**3**), 226–237. DOI: https://doi.org/10.1016/j.dt.2018.03.004
50. Yoon, H., Ha, H., Lee, T. et al. (2019) Pitting corrosion resistance and repassivation behavior of C-bearing duplex stainless steel. *Metals*, 9(**9**), 930. DOI: https://doi.org/10.3390/met9090930
51. Zhou, W., Ma, W., Li, Y., Sun, Y. (2021) Effect of sensitizing treatment on the microstructure and susceptibility to intergranular corrosion of high-nitrogen austenitic stainless steel. *Metallography Microstructure and Analysis*, **10**, 25–35. DOI: https://doi.org/10.1007/s13632-020-00708-4
52. Fujii, T., Suzuki, M., Shimamura, Y. (2022) Susceptibility to intergranular corrosion in sensitized austenitic stainless steel characterized via crystallographic characteristics of grain boundaries. *Corrosion Science*, **195**, 109946. DOI: https://doi.org/10.1016/j.corsci.2021.109946
53. Cárcel-Carrasco, F., Pascual-Guillamón, M., García, L.S. et al. (2019) Pitting corrosion in AISI 304 rolled stainless steel welding at different deformation levels. *Applied Sciences*, 9(**16**), 3265. DOI: https://doi.org/10.3390/app9163265
54. Ding, J., Colegrove, P., Martina, F. et al. (2015) Development of a laminar flow local shielding device for wire + arc additive manufacture. *J. of Materials Processing Technology*, **226**, 99–105. DOI: https://doi.org/10.1016/j.jmatprotec.2015.07.005
55. Vykhtar, B., Lingner, M., Richter, A.M., Hoops, F. (2022) Monitoring and local gas shielding at laser-based welding of titanium alloys. *Procedia CIRP*, **111**, 532c535. DOI: https://doi.org/10.1016/j.procir.2022.08.085
56. He, Y., Yang, Z., Yang, D. et al. (2025) Numerical simulation of local cooling on residual stress and deformation of welded joints of unequal thickness plates. *J. of Materials Research and Technology,* **36**, 8410–8420. DOi: https://doi.org/10.1016/j.jmrt.2025.05.057
57. Murakawa, H. (2013) *Residual stress and distortion in laser welding*: Handbook of laser welding technologies. Woodhead Publishing Series in Electronic and Optical Materials. Elsevier eBooks, 374–398. DOI: https://doi.org/10.1533/9780857098771.2.374
58. Unnikrishnan, R., Idury, K.S., Ismail, T. et al. (2014) Effect of heat input on the microstructure, residual stresses and corrosion resistance of 304L austenitic stainless steel weldments. *Materials Characterization*, **93**, 10–23. DOI: https://doi.org/10.1016/j.matchar.2014.03.013
59. Deepak, J., RP, A., Sundar, S.S. (2023) *Applications of lasers in industries and laser welding: A review*. In: *Proceedings,* 28 February 2023. DOI: https://doi.org/10.1016/j.matpr.2023.02.102
60. Kumar, B., Bag, S., Mahadevan, S. et al. (2021) On the interaction of microstructural morphology with residual stress in fiber laser welding of austenitic stainless steel. *CIRP J. of Manufacturing Science and Technology*, **33**, 158–175. DOI: https://doi.org/10.1016/j.cirpj.2021.03.009
61. Korinko, P.S., Malene, S.H. (2001) Considerations for the weldability of types 304L and 316L stainless steel. *Practical Failure Analysis*, **1**, 61–68. DOI: https://doi.org/10.1007/bf02715336
62. Hummelshøj, T.S., Christiansen, T.L., Somers, M.A. (2010). Lattice expansion of carbon-stabilized expanded austenite. *Scripta Materialia*, 63(**7**), 761–763. DOI: https://doi.org/10.1016/j.scriptamat.2010.05.031
63. Lin, Y., Chou, C. (1995) A new technique for reducing the residual stress induced by welding in type 304 stainless steel. *J. of Materials Processing Technology*, 48(**1–4**), 693–698. DOI: https://doi.org/10.1016/0924-0136(94)01710-i
64. Liu, Y., Wang, P., Fang, H., Ma, N. (2021) Mitigation of residual stress and deformation induced by TIG welding in thin-walled pipes through external constraint. *J. of Materials Research and Technology*, **15**, 4636–4651. DOi: https://doi.org/10.1016/j.jmrt.2021.10.035
65. Mohammed, M.S., Hamdey, M.D., Kareem, A.H., Majdi, H.S. (2024) Investigation of copper backing plate effects in stainless steel welding distortion, heat distribution, and residual stress. *Inter. J. of Heat and Technology*, 42(**4**), 1434–1446. DOI: https://doi.org/10.18280/ijht.420433

ORCID

Yu.V. Yurchenko: 0000-0001-9253-009X

CORRESPONDING AUTHOR

Yu.V. Yurchenko
E.O. Paton Electric Welding Institute of the NASU
11 Kazymyr Malevych Str., 03150, Kyiv, Ukraine.
E-mail: yurchenko@paton.kiev.ua

SUGGESTED CITATION

Yu.V. Yurchenko (2026) Analysis of actual problems of laser welding of thin-walled products made of stainless steels (Review). *The Paton Welding J.*, **04**, 37–48.
DOI: https://doi.org/10.37434/tpwj2026.04.05

JOURNAL HOME PAGE

https://patonpublishinghouse.com/eng/journals/tpwj

Received: 25.06.2025
Received in revised form: 08.10.2025
Accepted: 10.04.2026